STUDY OF PHOTOCHROMIC AND HYDROGEL MATERIALS FOR SMART WEARABLE APPLICATIONS

ZHANG JUNZE

PhD

The Hong Kong Polytechnic University

2026

The Hong Kong Polytechnic University

School of Fashion and Textiles

Study of Photochromic and Hydrogel Materials for Smart Wearable Applications

Zhang Junze

A thesis submitted in partial fulfilment of the requirements for the degree of Doctor of Philosophy

August 2025

CERTIFICATE OF ORIGINALITY

I hereby declare that this thesis is my own work and that, to the best of my knowledge and belief, it reproduces no material previously published or written, nor material that has been accepted for the award of any other degree or diploma, except where due acknowledgement has been made in the text.

_____ (Signed)

_____Zhang Junze _____ (Name of student)

Abstract

With the rapid development of wearable technology, smart materials that combine sustainability, multifunctional integration, and biocompatibility have become a research hotspot. Photochromic materials have significant potential in information security encryption and photopatterned displays, while hydrogels are indispensable in bioelectronic interfaces and implantable medical devices. However, traditional materials face challenges such as poor colorfastness, insufficient environmental stability, and difficulty balancing mechanical properties and biocompatibility, which seriously restrict their practical applications. Developing new materials with desirable properties of preparation scalability, performance stability, and environmental/ biological compatibility is crucial for promoting sustainable electronic textiles and smart healthcare devices. In this research, we have designed sustainable and smart wearables with excellent photochromic properties for photo-patterning and information security encryption applications, and developed highly stretchable and biocompatible wearable devices with excellent physical and electric properties for bioelectronic and healthcare applications.

Firstly, a new kind of fiber-based photochromic wearables is designed and developed by combining cotton fabric with a MoO_3-based self-adhesive polymer network and long chain silyl group. The prepared photochromic textile wearable has exhibited excellent fatigue resistance and favorable reversibility (> 40 cycles), rapid light response (reach color saturation with a UV dose of 60 kJ m^{-2}), outstanding color retention capability (> 90 days), and desirable biocompatibility (cell viability > 100%). In addition, the prepared photochromic textiles could maintain a fast light response and

excellent color retention even after experiencing repeated washing (20 cycles). Moreover, the photo-patterning photochromic wearables are verified by resisting the deterioration of acid solution, alkali solution, and sweat (pH 2.0–9.0) as well as keeping clear patterns under sunlight irradiation. As a demonstration of the applications, fiber-based photochromic textile wearables are made and employed for the sustainable applications of rewritable photo-patterning and information security encryption.

Then, a fiber-based photochromic wearable is designed and developed by covalently bonding MoO_3 microcapsule (MM) nanoparticles with a sheath-core structure into pristine cotton fabrics and integrating MM nanoparticles with sodium alginate (SA) through electrostatic forces and peptide linkages. The resulted photochromic wearable exhibits reversible color transformation and exceptional photochromic characteristics, including remarkable fatigue resistance (> 40 cycles), rapid light response, and outstanding color retention (> 60 days). Moreover, the photochromic wearable exhibits exceptional stability in diverse harsh environments, including different acid-base solutions (pH 2.0-9.0), various temperature (-30–60°C), indoor light and sunshine exposure, and repeated laundering (> 15 cycles). This photochromic fabric exhibits exceptional wearability, boasting remarkable flexibility (17 mm), and biocompatibility (cell viability > 95%). Notably, rewritable T-shirt and QR code information security encryption systems are demonstrated, highlighting their potential in customizable designs, flexible rewritable textiles, and information security encryption.

Furthermore, a multifunctional gelatin-based biogel (G-ZCX) is designed by integrating Zinc pyrrolidone carboxylate (PCA-Zn), cellulose nanofibers (CNF), and xanthan gum (XG) through synergistic ionic crosslinking and hydrogen bonding. This biogel combines low modulus (0.1-0.5 MPa), high stretchability (286.7%), and fatigue

resistance (>10,000 cycles), closely matching the mechanical properties of biological tissues. The biogel exhibits high ionic conductivity and negligible inflammatory responses both in vitro and in vivo. As a wearable sensor, it enables full-range motion detection and high-accuracy gesture recognition (99.8% via 1D-CNN). As demonstration of applications, it stably acquires multi-modal electrophysiological signals (electromyography (EMG)/ electrocardiography (ECG)/ electrooculography (EOG)/ electroencephalography (EEG)) with an excellent signal-to-noise ratio (SNR: 26.3 dB) and minimal attenuation over 24 h. For implantable applications, cytotoxicity tests and rat subcutaneous implantation experiments confirmed its excellent biocompatibility, and the inflammatory response was essentially eliminated after 14 days. This work provides a general strategy and a versatile platform for highly stretchable and biocompatible hydrogel materials with promising functions for various applications such as bioelectronics, personalized rehabilitation, and implantable medical devices.

This comprehensive study demonstrates the remarkable versatility of wearable devices with color-changing and biocompatible sensing capabilities and their associated functionalized systems. The innovative approaches and advanced designs outlined in these studies demonstrate significant improvements in photochromic performance, biocompatible performance, and application potential. Consequently, these findings pave the way for the development of sustainable and biocompatible wearable functionalities that are more intelligent, practical, human-centric, and sustainable.

Publications

Published Journal Paper:

1. **Zhang, J.,** Chen, T., Zhu, M., Lu, J., Liu, X., Sun, W., ... & Xu, B. (2025). Scalable, Fast light-responsive, and excellent color-retention fiber-based photochromic wearables for sustainable photo-patterning and information security encryption. Advanced Functional Materials, 35(8), 2415622.
2. **Zhang, J.,** Liu, X., Chen, T., Han, J., Ahmed, T., Wang, X., ... & Xu, B. (2025). Sustainable Photochromic Wearables with Excellent Retention and Superior Stability for Customizable Patterns and Information Security Encryption. SusMat, e70023.
3. **Zhang, J.,** Xu, B., Chen, K., Li, Y., Li, G., & Liu, Z. (2024). Revolutionizing digital healthcare networks with wearable strain sensors using sustainable fibers. SusMat, 4(4), e207.
4. Fang, C., Liu, X., Wang, S., **Zhang, J.,** Zhao, J., Fan, X., & Xu, B. (2025). Dual mediation of MnSe as superior cathodes for Durable Zn-ion energy storage. Chemical Engineering Journal, 508, 160999.
5. Wang, Q., Liu, X., Han, J., Xiao, Y., Tan, D., Yang, Y., **Zhang, J.,** & Xu, B. (2025). High-performance naturally crosslinked silk-based triboelectric nanogenerators for multimodal sensing and energy harvesting. Nano Energy, 135, 110620.
6. Ahmed, T., Gao, Y., So, M. Y., Tan, D., Lu, J., **Zhang, J.,** & Xu, B. (2024). Diamond-Structured Fabric-Based Triboelectric Nanogenerators for Energy Harvesting and Healthcare Application. Advanced Functional Materials, 34(48), 2408680.
7. Zhu, M., Xu, B., Chen, T., **Zhang, J.,** & Sun, W. (2024). Advanced Functional

Photochromic Wearables with Superior Durability and Stability for Sustainable Applications. Advanced Functional Materials, 34(42), 2406840.

8. Han, J., Li, Z., Fang, C., Liu, X., Yang, Y., Wang, Q., **Zhang, J.,** & Xu, B. (2024). Hierarchically porous architectured stretchable fibrous materials in energy harvesting and self-powered sensing. Nano Energy, 129, 110080.
9. Chen, T., Xu, B., Zhu, M., **Zhang, J.,** Sun, W., & Han, J. (2024). Advanced functional photochromic wearables with fast photo-responsivity, long color-retention, and multi-environmental stability. Chemical Engineering Journal, 490, 151804.
10. Chen, T., Xu, B., Han, J., Zhu, M., **Zhang, J.,** & Li, Z. (2024). Chelating coordination regulated photochromic electrospun nanofibers for waterproof and long-color-retention rewritable wearables. ACS Applied Materials & Interfaces, 16(10), 13305-13315.

Published Patent:

1. Bingang Xu, Meng Zhu, Tiandi Chen, **Junze Zhang**. Washable photochromic fabric, method for controlling color-change performance, and method for fading color, Application No. 2024101874919, 2024.02.20.
2. Bingang Xu, Tiandi Chen, **Junze Zhang**, Meng Zhu. Preparation method of functional photochromic fabric, functional photochromic fabric and application, Application No. 2024101874995, 2024.02.20.

Journal Paper under Preparation:

1. **Zhang, J.,** Liu, X., Chen, T., Sun, W., Ahmed, T., Yang, Y., Lu, J., Wang, S., Xu, B. Highly Stretchable and Biocompatible Gelatin Biogels for Multifunctional

Electronic Applications. (Under preparation)

Acknowledgements

First and foremost, I would like to express my sincerest gratitude to my chief supervisor, Prof. XU Bingang, Professor in the School of Fashion and Textiles at the Hong Kong Polytechnic University, for providing me such a precious opportunity to pursue my PhD study, as well as for his continuous support, expert guidance and inspiring encouragement. His contagious enthusiasm and meticulous attitude to scientific research inspire me a lot and set me a perfect example for my whole academic life.

I would also like to express my special thanks to my research colleagues and teammates, especially Dr. Chen Tiandi, Dr. Zhu Meng, Dr. Lu Jian, Dr. Yang Yujue, Mr. Liu Xinlong, Ms. Han Jing, Mr. Ren Xingchao, Ms. Wang Qian, Ms. GAO Yuanyuan, and Mr. Ahmed Taosif, for their invaluable assistance and professional suggestions in my research.

My sincere appreciation also goes to the technicians in my department for their valuable advice and support throughout this research. Their expert knowledge and patient instruction have been instrumental in the successful completion of my experiments.

Finally, I would like to express my heartfelt gratitude to my family for their unwavering support, understanding, and encouragement throughout my PhD journey. Their love and care have been my greatest source of strength and motivation, enabling me to overcome challenges and pursue my academic goals with confidence.

Table of Contents

List of Figures

List of Tables

List of Abbreviations

spiropyrans	SPs
diarylethenes	DAEs
ultraviolet	UV
polycaprolactone	PCL
polyethylene terephthalate	PET
polymethyl methacrylate	PMMA
phosphomolybdic acid	PMoA
polyacrylamide	PAM
wearable hydrogels	WHs
polyacrylic acid	PAA
liquid metal	LM
polyoxyethylene octyl phenol ether-10	OP-10
ethylenediamine tetraacetic acid	EDTA
ammonium persulfate	APS
hydrochloric acid	HCl
sodium hydroxide	NaOH
sodium bicarbonate	$NaHCO_3$
transmission electron microscope	TEM
X-ray diffraction	XRD
Fourier transform infrared spectroscopy	FT-IR
Energy Disperse Spectroscopy	EDS
Thermal gravimetric analysis	TGA
Sodium molybdate	Na_2MoO_4
scanning electron microscopy	SEM
polytetrafluoroethylene	PTFE
Zinc pyrrolidone carboxylate	PCA-Zn

electromyography	EMG
electrocardiography	ECG
electrooculography	EOG
electroencephalography	EEG
hematoxylin and eosin	H&E
Molybdenum trioxide	MoO_3
MoO_3 self-synthesized polymer network-based photochromic textiles	MSPPT
MoO_3-based self-synthesized polymer network	MSPN
N-butyl acrylate	BA
styrene	St
vinyltrimethoxysilane	VTMS
hexadecyltrimethoxysilane	HDTMS
ammonium molybdate	$(NH_4)_2MoO_4$
ammonium heptamolybdate	$(NH_4)_6Mo_7O_{24}$
the hexagonal phase of MoO_3	h-MoO_3
the orthorhombic phase of MoO_3	α-MoO_3
MoO_3 microcapsule	MM
sodium alginate	SA
SA/MM/Epoxy pristine cotton fabrics	SAME-PCFs
Glycidoxypropyltrimethoxysilane	KH560
Epoxy PCFs	E-PCFs
MM/Epoxy PCFs	ME-PCFs
potassium persulfate	$K_2S_2O_8$
glutaraldehyde	GA
x-ray photoelectron spectroscopy	XPS
cellulose nanofibers	CNF
xanthan gum	XG
natural moisturizing factor	NMF
gelatin-based biogel integrating PCA-Zn, CNFs, and XG	G-ZCX biogel

deep learning	DL
one-dimensional convolutional neural networks	1D-CNNs
extracellular matrix	ECM
sprague-dawley	SD

Chapter 1. Introduction

1.1 Research Background

With the improvement of living standards and the advancement of technologies, consumer demand for wearable devices with both sustainable color-changing and biocompatible sensing capabilities has surged[1, 2]. Sustainable color-changing wearables, with their dynamic aesthetics, have captured the attention of both the fashion and technology markets, infusing practical devices with vitality and uniqueness. Meanwhile, biocompatible wearable sensors offer real-time and continuous monitoring of physiological and environmental conditions through accurate health assessments—including physical activity and biochemical indicators—providing transformative solutions for early disease detection, medical rehabilitation, chronic disease management, personalized health interventions, and telemedicine. Photochromic elements (such as MoO_3 nanoparticles) impart dynamic, UV-responsive visualization capabilities to textile fabrics, while embedded biocompatible sensing elements (such as biocompatible hydrogel electrodes) enable real-time monitoring of physiological signals and movement. The synergistic integration of these two technologies not only expands the application scenarios of wearable devices—from health management to information security and encryption—but also reduces environmental impact through material reuse, promoting the evolution towards sustainable intelligence.

Photochromic materials, as a class of important functional materials, have attracted increasing attention owing to their remarkable capability to reversibly exchange light under different conditions or isomerize into forms with dramatically

diverse properties. Their practical applications[3] span optical data storage[4, 5], photonic memory[6], sensors[7, 8], smart inks[9, 10], fluorescence imaging systems, and artificial neuron models. As representatives of the new generation of optical wearable devices, photochromic fabrics are gradually breaking through the static aesthetic boundaries of traditional clothing, moving toward a new era of dynamic, programmable, and multi-scenario applications. The fabrication of photochromic textiles involves embedding light-sensitive compounds into the fibers of the fabric[1, 11]. When exposed to UV radiation, they can change color, and upon removal of the light source or application of heat, they revert to their original state, resulting in a reversible color change. While early color-changing textiles were primarily used in specialized fields such as military camouflage, advances in materials science and manufacturing technology have enabled photochromic fabrics to be widely applied in health monitoring, environmental sensing, personalized display, and intelligent interaction. These fabrics can not only change their appearance in real time according to external lighting conditions, but also serve as information display interfaces or environmental sensors, greatly enriching the functionality and user experience of wearable devices. Looking ahead, photochromic fabrics are expected to become a foundational technology in smart clothing, medical assistance, and information security, driving wearable devices toward greater intelligence and personalization. Despite significant progress in developing photochromic textiles with multiple color-switching functions, challenges remain in achieving fast color switching, long-term color retention, and washing durability.

Wearable electronic devices, by integrating biocompatible sensors, can sense and collect a variety of physiological and motion signals from the human body—such as heart rate, body temperature, gait, and muscle activity—in real time. These devices

efficiently convert physical signals, such as mechanical motion, into electrical signals, and possess a high degree of flexibility and stretchability, allowing them to adapt to the complex curves of different body parts for comfortable, long-term wear. Compared with traditional rigid metal or semiconductor-based sensors, flexible wearable devices offer significant advantages in sensing range, flexibility, and wearability, greatly expanding the application scenarios and population coverage of health monitoring. The widespread adoption of wearable biocompatible devices and ongoing technological advancements have driven the development of digital health platforms and transformed medical service models. Through wireless communication and data integration, these devices enable continuous collection and remote transmission of personal health data, providing a robust foundation for personalized health management, disease early warning, remote diagnosis and treatment, and medical rehabilitation. In areas such as chronic disease management, elderly care, and sports health, wearable biocompatible devices enable all-weather, non-invasive, and low-power health monitoring, significantly improving the efficiency and accessibility of medical services. Furthermore, wearable biocompatible sensors offer advantages such as environmental friendliness, portability, low energy consumption, and minimal manufacturing waste, helping to reduce the environmental impact of medical consumables, lower healthcare costs, and promote sustainable development in the healthcare industry. With further integration of artificial intelligence, big data, and the Internet of Things, the biocompatible devices are poised to enable more intelligent, personalized, and inclusive health management, becoming a key driver of smart healthcare and the development of a healthy society.

This research aims to develop photochromic textile wearables with outstanding photochromic performance through advanced material design and optimization, and to

design wearable biocompatible materials and devices for multifunctional bioelectronic and healthcare applications.

1.2 Research Objectives

This research aims to design and develop photochromic and hydrogel wearables with advanced sensing capabilities and versatile functional systems. These wearable devices exhibit significant improvements in photochromic performance, biocompatibility, and application potential, paving the way for the development of more intelligent, practical, sustainable, and biocompatible wearable devices. The specific research objectives are as follows:

1. To synthesize photochromic materials (MoO_3) with outstanding photochromic properties for use as functional components in color-switching wearables, achieving long retention time, color-switching ability, enhanced durability, and superior stability.
2. To design photochromic wearables by integrating MoO_3 into fabrics, enabling scalable manufacturing processes, rapid light responsiveness, excellent washing fastness, and long color retention.
3. To develop photochromic wearables by combing MoO_3 microcapsules with fabrics, achieving great flexibility, long retention time and superior stability.
4. To fabricate gelatin-based biogels, enabling high stretchability, fatigue resistance, and excellent biocompatibility for comprehensive motion detection, high-accuracy gesture recognition, and reliable acquisition of electrophysiological signals.

1.3 Research Significance

With rising living standards and technological advancements, there is a growing

demand for wearable devices featuring sustainability, dynamic aesthetics, and health monitoring capabilities. While traditional materials have been widely used to develop sustainable and functional wearables for photochromic applications and medical monitoring, they still face numerous challenges such as poor photochromic properties, insufficient environmental stability and durability, and bad biocompatibility. These limitations not only limit the practical application of photochromic wearables but also hinder the widespread adoption of wearable sensors for long-term health monitoring and implantable medical applications. Herein, this research study achieved key breakthroughs in material design and structural optimization by designing and developing MoO_3-based photochromic fiber-based wearables and highly stretchable and biocompatible hydrogels. The performance of photochromic textiles is significantly improved, including light responsiveness speed, cycling stability, and environmental durability, enabling them to meet diverse application such as rewritable patterns, information encryption, and anti-counterfeiting identification. Furthermore, the biogels exhibit low modulus, high stretchability, excellent durability, and great biocompatibility, enabling highly sensitive capture of motion and physiological signals and accurate gesture recognition while demonstrating excellent biocompatibility in implantable experiments.

1.4 Outline

This thesis is divided into seven chapters, and the structure is organized as follows:

Chapter 1 briefly provides a general overview of this research study, including the research background, objectives, significance and the overall structure of the thesis. It highlights the importance of developing sustainable and functional wearable devices.

Chapter 2 presents a comprehensive review of the development of sustainable and

functional wearables. The fundamental principles, classifications, functionalization strategies, and application scenarios of photochromic textiles and wearable hydrogels are discussed, summarizing the current achievements and challenges in the field.

Chapter 3 introduces the materials, fabrication techniques, and characterization methods adopted in the study. It elaborates on the design strategies for preparing photochromic textiles and biocompatible hydrogels, along with the evaluation systems employed for analyzing their structural, optical, mechanical, and biocompatible performance.

Chapter 4 explores the fabrication of fiber-based photochromic wearables with scalability, fast light-responsiveness, and excellent color-retention time. It shows their application potential in sustainable photo-patterning and information security encryption.

Chapter 5 presents an optimized design of photochromic fabrics with superior stability and durability under diverse environmental conditions. Demonstrations include rewritable textiles, customizable patterns, and secure information encryption systems.

Chapter 6 details the development of multifunctional gelatin-based biogels with superior stretchability, fatigue resistance, and excellent biocompatibility. Their applications in motion detection, gesture recognition, electrophysiological monitoring, and implantable devices are systematically discussed.

Chapter 7 summarizes the findings of this research study and suggestions for future directions.

Chapter 2. Literature Review

2.1 Development of Fascinating Optical and Sensing-ability Wearables

Driven by an increasing consumer demand for daily captivating optical and sensing-enabled wearables for personal fitness monitoring, functional and sustainable wearables are rapidly emerging as a multibillion-dollar industry, transforming the wearable market through sustainable consumer products, optoelectronic devices, eco-friendly photo-patterning information displays, and medical equipment[12-14].

Wearables with color-changing and sensing capabilities facilitate significant advancements in functional wearable technology. Color-changeable wearables captivate the fashion and technology markets with their dynamic aesthetics, infusing vitality and distinction into utilitarian equipment[15]. Wearable sensors enable real-time, unobtrusive, continuous, and multi-parameter monitoring of physiological and environmental conditions through precise health assessment (including physical activity and biochemical markers), offering transformative solutions for early disease detection, medical rehabilitation, chronic disease management, personalized health interventions, and telemedicine[16, 17]. The visual feedback of color-changing wearables enhances the direct visualization of health status indicators, such as stress and exhaustion, hence augmenting users' health awareness. Wearable sensing devices can impart sensing capabilities to devices while integrating with color-changeable functionalities, so greatly augmenting the interaction intelligence and application scope of devices in health, safety, environmental, and other domains. Moreover, in contrast to conventional apparel, appealing optical wearables significantly diminish environmental pollution and printing expenses in the manufacturing process of traditional garments. Wearable sensors offer significant advantages such as exceptional

durability, skin adherence, and remarkable adaptability, which substantially diminish electronic waste, manufacturing costs, and resource usage. In summary, fascinating optical and sensing wearables advance this field towards a more intelligent, practical, human-centered, and sustainable trajectory, challenging conventional morphological and functional limits.

2.2 Fascinating Optical Wearables

Color enhances our world with brightness and brilliance, improving human experience through both natural events and synthetic materials. This essential aesthetic and functional attribute is exemplified in stimuli-responsive or chromic materials. These systems exhibit reversible, discernible color alterations upon exposure to external stimuli, a characteristic referred to as chromism. This dynamic flexibility offers significant potential for advanced applications, such as adaptive textiles, next-generation displays, intelligent windows, sophisticated security features, and biological sensors. Chromism appears in several forms influenced by the stimulus: thermochromism, mechanochromism, electrochromism, and photochromism. Photochromic technologies are especially intriguing for applications requiring easy, accurate, and cost-effective control. Their sensitivity to light—a plentiful, easily directed, and non-contact stimulus—provides unparalleled benefits for incorporation into functional devices. This intrinsic compatibility establishes photochromics as a fundamental technology for the emerging domain of intriguing optical wearables. These wearables seek to integrate dynamic visual attributes with fabrics and personal accessories, advancing beyond static aesthetics to interactive, responsive, and functional interfaces worn on the body. The advancement of photochromic garments signifies a pivotal frontier. The history of chromic wearables can be traced back to camouflage battle fatigues made with special materials and color patterns, enabling

soldiers to blend seamlessly into diverse environments and evade detection, marking one of the early applications of chromic textiles (Figure 2.1)[15]. By changing color when exposed to light, these systems enable clothes or accessories to change how they look in real-time based on things like sunlight, let users customize their appearance, show health information, or act as interactive screens—all while being easy to control from a distance, using little energy, and able to work with flexible materials. Thus, the development of photochromic materials and their incorporation into wearable devices is not solely an aesthetic endeavor but a crucial advancement toward smart, interactive, and adaptive personal technologies.

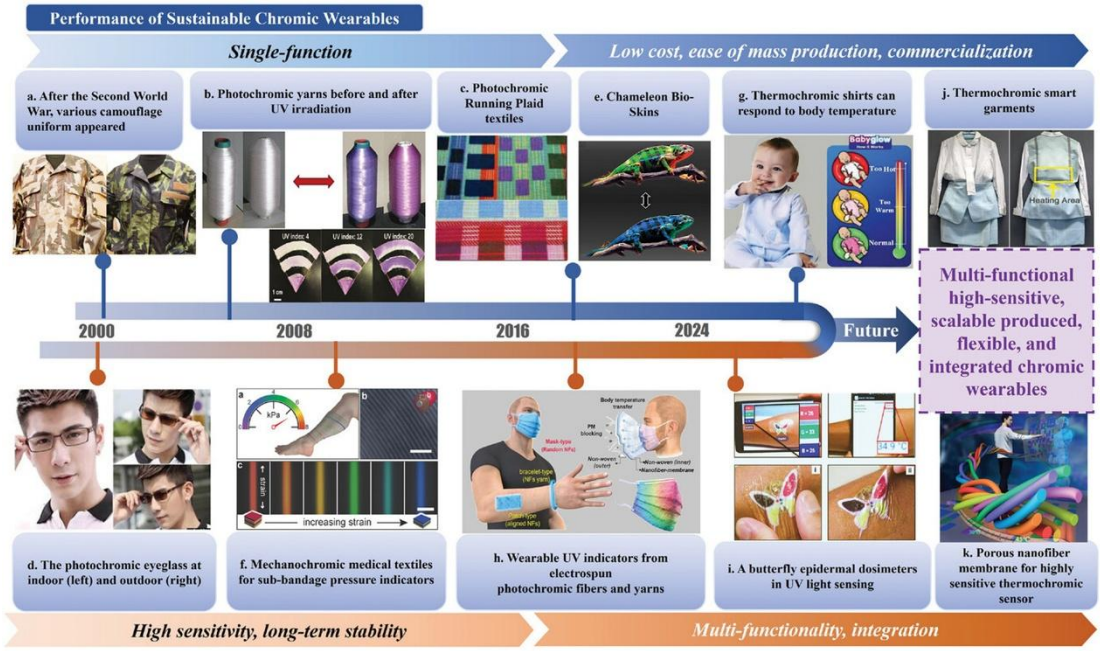

Figure 2.1 Development history of fascinating optical wearables[15].

2.2.1 Photochromic materials

Photochromism is when a chemical changes between two different forms (called A and B) that absorb light differently, and this change is caused by light (Figure 2.2) [18, 19]. This light-induced interconversion, generally happening upon absorption

within certain wavelength ranges (specifically 100–400 nm, including UVC: 100–280 nm, UVB: 280–315 nm, and UVA: 315–400 nm), modifies molecule structure and electronic energy levels, resulting in a novel spectroscopic state. The thermodynamically stable form (A) undergoes photoisomerization to a metastable form (B); reversion to A happens by thermal or photochemical processes[20]. This back-and-forth change in the molecule comes with significant differences in physical properties, such as how light bends (refractive index), how well it conducts electricity (dielectric constant), thickness (viscosity), how well it dissolves (solubility), and how it interacts with surfaces (surface wettability). In the predominant manifestation (positive photochromism), a colorless or pale-yellow state (A) transforms into a colored form (B) upon exposure to irradiation. Negative (inverse) photochromism, which occurs when a colorful A state bleaches to a colorless B after irradiation, along with reversible color-to-color transitions, is less prevalent. The phenomenon occurs in biological systems (e.g., retinal photochemistry in vision[21]), inorganic chemicals, and other organic materials. The intrinsic optical modification ability of photochromic materials under UV light facilitates prospective applications. These encompass dynamic fabrics, multipurpose wearables, adaptive camouflage, wearable UV radiation sensors, and optical image storage systems. The easy, non-invasive regulation provided by light stimulation renders photochromic especially appropriate for incorporating responsive optical characteristics into wearable devices.

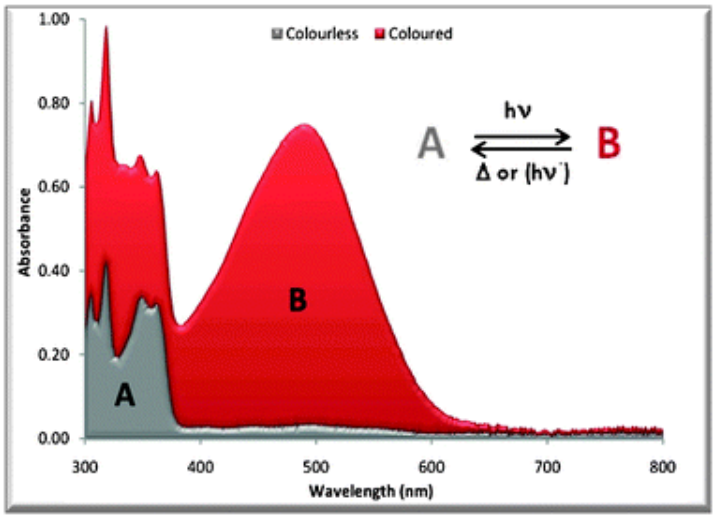

Figure 2.2 The change of absorption spectra between two states[20].

2.2.2 Classification of photochromic materials

Photochromic materials are principally classified into organic and inorganic categories according to their composition. Over one hundred different organic photochromic compounds have been created, including well-known types like spiropyrans (SPs), spirooxazines, fulgides, diarylethenes (DAEs), azobenzenes, and naphthopyrans[20]. A primary attribute of the majority of organic photochromics is the temperature instability of their photogenerated isomers. Consequently, these isomers spontaneously return to their original state, even in the absence of light, via reversible photochromic processes. Inorganic photochromic compounds mainly consist of certain transition metal oxides (like WO_3, MoO_3, ZnO, TiO_2, VO_2), metal halides, and some rare earth complexes[22]. Although these transition metal oxides typically provide benefits such as enhanced stability and reduced production costs as photochromic materials, their photochromic effectiveness is generally worse.

2.2.2.1 Organic photochromic materials

Organic photochromic materials have attracted significant research interest due to

their capacity to exhibit fast photochromic responses across broad segments of the visible spectrum. Numerous organic compounds demonstrate this property, including SP, spirooxazines, fulgides, DAEs, azobenzenes, and naphthopyrans. Key mechanisms underpinning the photochromism in these compounds encompass pericyclic reactions, cis-trans isomerizations, intramolecular hydrogen transfer, intramolecular group transfers, dissociation processes, and electron transfers (oxidation-reduction).

SPs and spirooxazines undergo reversible ring-opening via UV-induced C–O bond heterolysis, generating colored, planar merocyanine chromophores visible to the eye (Figure 2.3a)[23-25]. Discovered in the 1950s, SPs exhibit pronounced color changes and low background fluorescence, enabling applications in data storage, optical switches, and displays[26]. Spirooxazines offer superior photochemical stability and fatigue resistance, suiting them for anti-counterfeiting applications, though their thermal stability remains inferior to SPs (Figure 2.3b)[27]. Both systems revert thermally or under visible light[28, 29]. Fulgides and DAEs feature distinct stability profiles[30]. Fulgides undergo thermally irreversible photochromism via π-π* transitions and intramolecular bridged-ring formation, making them suitable for optical memory despite slow fading kinetics limiting textile use[31]. DAEs exhibit substituent-dependent behavior[32]: furan/thiophene-based derivatives display thermally irreversible photochromism akin to fulgides, while phenyl/indole-based variants show reversible, rapid light-driven transitions between open-ring (colorless) and closed-ring (colored) states (Figures 2.3c, d) [33]. Both face application barriers—fulgides in sensitivity and DAEs in complex synthesis and cost. Azobenzene derivatives reversibly isomerize between stable trans (E) and metastable cis (Z) configurations under light/heat, with significant geometric changes enabling shape-morphing molecular devices[34]. Naphthopyrans[35], known since the 1960s, undergo UV-induced C(sp^3)–

O cleavage to form colored TC (trans-cis) and TT (trans-trans) ring-open isomers with extended conjugation (Figure 2.3e, f). Reversion occurs directly for TC isomers under visible light/heat, whereas TT reverts indirectly via TC, resulting in slower kinetics[36]. These isomerization-driven systems underpin advanced photoresponsive technologies[37].

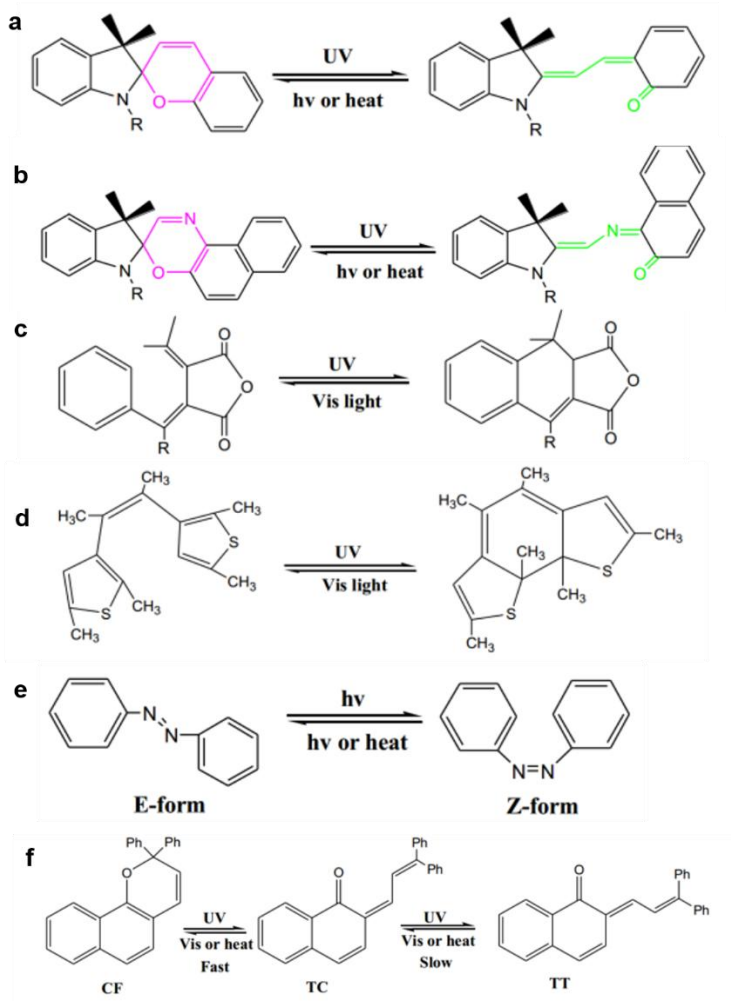

Figure 2.3 The photochromic mechanism of a) SPs, b) spiroxazine, c) fulgides, d) DAEs, e) azobenene, f) naphthopyran.

The photochromic mechanisms of the abovementioned organic photochromic materials can be divided into three types: SP, spirooxazine, and naphtholpyran

attributed to the heterocleavage of C (sp^3)-O bonds in the molecular structure; The photochromism of fulgides and diarylethylene is attributed to molecular pericyclic reactions. It is worth noting that these two materials also exhibit thermal irreversibility (i.e., they cannot autonomously return to their original state under dark conditions), making them potentially useful in specific fields such as optical memory and optical switching devices; The photochromism of azobenzene is attributed to cis trans isomerism. However, it is undeniable that the molecular structure of organic photochromic compounds contains a large number of unsaturated bonds, which are highly susceptible to changes in pH in the external environment[38], solvents, and oxidation, leading to irreversible color changing reactions and even permanent loss of color changing ability, resulting in decreased photochemical fatigue and durability[39-41].

2.2.2.2 Inorganic photochromic materials

Transition metal oxide photochromics are defined as inorganic systems exhibiting reversible optical changes under light exposure, such as WO_3, ZnO, TiO_2, V_2O_5, and MoO_3. Their inherent advantages—including extended retention times[42], exceptional chemical durability[43], mechanical robustness, and facile fabrication into diverse architectures—position them as promising alternatives to organic counterparts[44]. Historically constrained by weak coloration, slow kinetics, and limited reversibility, recent breakthroughs in nanoscale engineering have unlocked their latent potential. These advanced systems now demonstrate tunable wavelength selectivity, rapid responsivity, and multi-chromic capabilities. Such engineered properties enable transformative applications in dynamic optical filters, high-stability anti-counterfeiting labels, and reconfigurable photonic devices, marking a paradigm shift in stimulus-responsive material design.

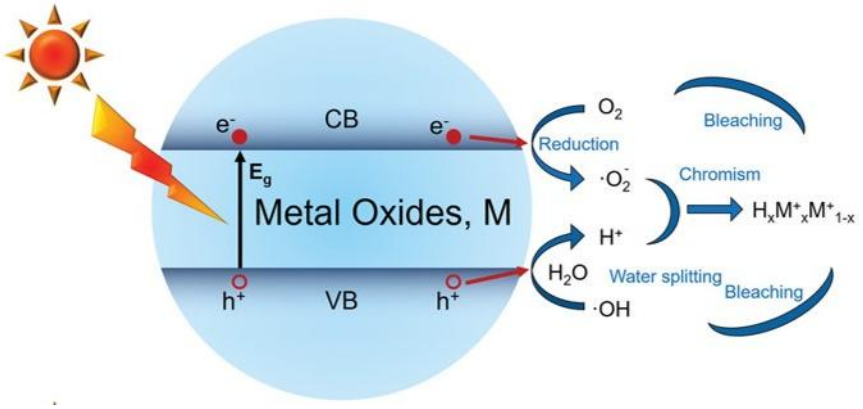

Figure 2.4 Illustration of the photochromic mechanisms of metal oxides[22].

In transition metal oxides, intramolecular hydrogen transfer occurs when UV irradiation detaches hydrogen atoms from surface-adsorbed organic molecules. These hydrogen atoms donate electrons to the oxide lattice, reducing metal cations to lower valence states, while the resulting protons localize near oxygen anions[45, 46]. This hydrogen photochromism mechanism involves UV-induced abstraction reactions that facilitate proton accommodation and migration. Concurrently, electron transfer proceeds through redox processes where electrons relocate between species, altering oxidation states[47, 48]. Such electron transfers—characteristic of ionic bonding—mirror biological processes including oxygen binding, photosynthesis, and detoxification. In photochromic transition metal oxides, these energy transfer processes fundamentally involve electron exchanges (Figure 2.4)[49].

WO_3 exhibits reversible photochromism across multiple structural forms—including bulk crystals, thin films, and quantum dots—enabling reversible optical switching between transparent and blue states under light, heat, or electrical stimuli. This behavior originates from reduction-oxidation reactions involving tungsten valence transitions ($W^{6+} \rightarrow W^{5+}/W^{4+}$), where both W^{5+} and W^{4+} contribute to coloration, with W^{4+} driving deep blue transformations[50, 51]. The mechanism involves two concurrent processes: UV-induced valence reduction ($W^{6+} \rightarrow W^{5+}$) and structural

reorganization into hydrogen tungsten bronze (H_xWO_3), causing visible coloration. With a bandgap of 2.6–3.0 eV[52], UV irradiation generates holes that decompose adsorbed water to release protons[53]. These protons and photogenerated electrons drive water splitting, forming blue H_xWO_3. Concurrently, oxygen radicals either occupy lattice vacancies or desorb, facilitating the bleaching process[54].

ZnO finds extensive application in personal care products, including sunscreens, cosmetics, and lotions[55]. Its photochromic and photocatalytic behaviors arise, respectively, from nanostructural morphology variations and synergistic combinations with organic photochromic molecules[56]. Although ZnO's bandgap (3.20–3.37 eV) suggests optimal absorption at 350-400 nm, it exhibits broad visible-light absorption beyond 400 nm[57]. This necessitates hybrid organic-inorganic systems to achieve energy-level modifications for enhanced UV selectivity and targeted photochromic responses[58]. Surface functionalization with DAEs [59], azobenzenes[60], or SPs[61] enables precise tuning of ZnO's wavelength-specific sensitivity. Upon light exposure exceeding ZnO's bandgap in hybrid systems, photoexcitation promotes electrons to the conduction band. These react with O_2 forming superoxide radicals (O_2^-), while valence band holes generate hydroxyl radicals (OH^-) through hydroxide oxidation. The resulting radicals induce photochromic transformations via oxidative degradation of the organic components[62].

TiO_2 demonstrates both photochromic and photocatalytic behavior under ultraviolet (UV) illumination, a property originating from its distinctive electronic structure[63]. UV irradiation with energy matching or exceeding the bandgap promotes electrons from the valence band to the conduction band, generating electron-hole pairs. The photoexcited electrons reduce Ti^{4+} species to Ti^{3+} states. Anatase and rutile polymorphs exhibit optical absorption gaps of 3.2 eV and 3.0 eV[64], corresponding to

wavelengths of ~413 nm and ~387 nm, respectively. Consequently, TiO_2 achieves photochromic responses under UV and near-visible wavelengths.

The photochromic behavior of vanadium oxide compounds arises from photoinduced charge transfer, leading to valence state alterations in vanadium ions[65]. Among these, the mechanism of V_2O_5 involves photoexcitation initiating electron transfer, reducing V^{5+} to V^{4+} species, which alters optical absorption. V_2O_5 possesses an optical bandgap of approximately 2.52 eV[66], corresponding to visible light absorption near 490 nm. However, bandgap engineering through doping, composite formation, or metal intercalation enables tuning of its absorption profile towards the UV spectral range.

MoO_3, a wide band gap n-type semiconductor, is renowned for its applications in photochromic and electrochromic systems, catalysis, sensors, and organic solar cells[67, 68]. Its photochromic behavior is characterized by reversible color change upon UV exposure and subsequent bleaching in oxidizing environments (e.g., H_2O_2). MoO_3 nanosheets have stronger color-changing abilities due to better movement of charge carriers, more flexible structure, and effects from being very small. MoO_3 possesses a bandgap (2.75–3.25 eV) slightly broader than that of WO_3[69, 70]. When UV photons ($h\nu > Eg$) excite electrons from the valence band to the conduction band, generating electron-hole pairs. Surface-adsorbed water interacts with photogenerated holes, releasing protons (H^+). These protons intercalate into the lattice, forming hydrogen molybdenum bronze (H_xMoO_3). Concurrently, Mo^{6+} ions capture electrons, reducing to Mo^{5+}. The ensuing intervalence charge transfer ($Mo^{5+} \rightarrow Mo^{6+}$) induces a characteristic blue coloration. Exposure to an oxidizing agent (e.g., O_2 or H_2O_2 solution) re-oxidizes Mo^{5+} to Mo^{6+}, restoring the original bleached state[71].

2.2.3 Applications of photochromic materials

Photochromic materials can be used in many fields because of the reversible change of color during light irradiation, including life decorations, information storage, anti-counterfeiting materials, and camouflage materials.

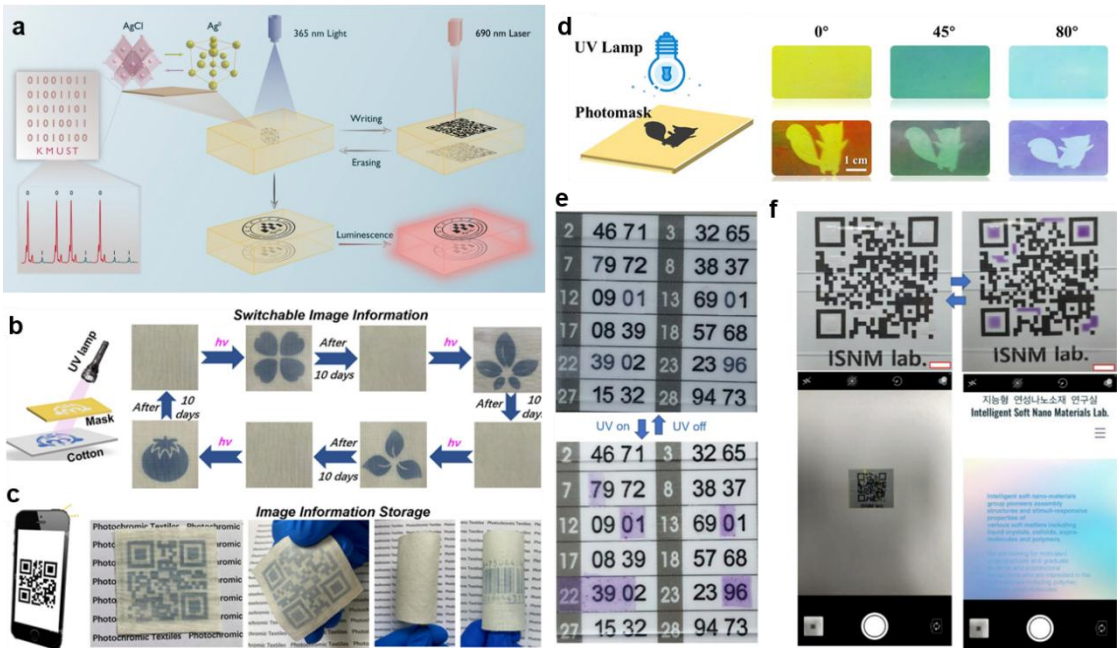

Figure 2.5 a) Schematic illustration of capability of Eu-Ag germanium borate glass for writing, reading, and erasing application[72]. b) Patterns can be written and erased by a photomask and UV light. c) Application of photochromic cotton fabric for image information storage[73]. d) Illustration of the photochromic film showing different color and patterns[74]. e) Encryption application of photochromic film. f) Image information storage showing QR code[75].

2.2.3.1 Life decorations

Photochromic materials have been widely used in daily life for decorative or protective purposes. For example, by adding photochromic materials to clothing or building coatings, endowing them with photochromic function. Clothing and building walls can convert their colors under light irradiation, which not only enhances

aesthetics but also brings more choices to people's lives. Adding a light-colored material to glasses can intelligently control the color of the glasses due to the sensitivity of photochromic materials to light (Figure 2.5a)[72]. When the 365 nm UV light is irradiated into the glass, a dark area is formed as the photochromic region, and the optical information is written. Excitation light from a xenon lamp is used to excite the glass to realize an optical information readout. The modulated transmittance or luminescence in the glass could be erased by using 690 nm laser irradiation. Under strong light exposure, glasses will change color from light to dark to avoid direct eye injury. In addition, smart windows and photochromic glass can quickly adjust the color based on the intensity of incident light, thereby adjusting the light transmittance and carrying heat, which is used to regulate indoor light and save energy.

2.2.3.2 Information storage

Photochromic materials can be used in information storage as a means of creating rewritable and erasable data storage devices. These materials have the ability to change color or optical properties when exposed to light, and this property can be harnessed for information storage applications. One potential application is in the development of photochromic optical data storage devices. By using photochromic materials as the storage medium, data can be written, read, and erased using light (Figures 2.5b, c)[73]. This could enable the creation of rewritable optical storage media that can be used for archival purposes, data backup, or other storage needs. Another potential application is in the development of photochromic-based memory devices. By utilizing the reversible color-changing properties of photochromic materials, it may be possible to create non-volatile memory cells that can store information in a stable manner without the need for a constant power supply. This could lead to the development of new types of memory technologies with potential applications in data storage, computing, and other

fields. Overall, the application of photochromic materials in information storage has the potential to enable the development of new types of rewritable and erasable data storage devices, as well as innovative memory technologies that could offer advantages in terms of stability, energy efficiency, and data retention.

2.2.3.3 Anti-counterfeiting materials

Photochromic materials can be used in anti-counterfeiting materials to create security features that change color or appearance when exposed to light. This makes it difficult for counterfeiters to replicate or reproduce the security features, as the color-changing properties of the photochromic materials are difficult to mimic. For example, photochromic inks can be used in printing security labels, documents, or packaging. When exposed to UV light, the photochromic ink changes color, revealing hidden patterns, text, or images that are only visible under specific lighting conditions (Figure 2.5d)[74]. This makes it easy for authentication and verification of the original product or document. Additionally, photochromic materials can be incorporated into security threads, holograms, or other security elements to provide an extra layer of protection against counterfeiting. The color-changing properties of the photochromic materials make it easier for consumers, retailers, and authorities to identify genuine products and distinguish them from counterfeit ones. Overall, the application of photochromic materials in anti-counterfeiting materials enhances security and helps protect brands, products, and documents from unauthorized replication and fraud.

2.2.3.4 Camouflage materials

Photochromic materials can be used in camouflage to create adaptive and responsive camouflage systems that can change color or appearance in response to different lighting conditions. This technology can be particularly useful for military applications, where the ability to blend into different environments and adapt to

changing lighting conditions is crucial for concealment and protection. By incorporating photochromic materials into camouflage fabrics, paints, or coatings, it is possible to create camouflage patterns that can adjust their color or pattern in response to varying levels of light (Figures 2.5e, f)[75]. This allows the camouflage to better match the surrounding environment, whether it's in bright sunlight, low light, or shadowed areas. Additionally, photochromic materials can be used to create dynamic camouflage systems that respond to different wavelengths of light, such as UV or infrared. This can help military personnel or equipment to remain concealed from detection systems that operate in these spectrums. Overall, the application of photochromic materials in camouflage can enhance the effectiveness of concealment and protection in military and tactical environments, providing adaptive and responsive camouflage solutions that can better match the surrounding environment and improve the overall effectiveness of camouflage systems.

2.3 Development of Photochromic Wearables

2.3.1 Functionalization strategies for photochromic wearables

The rapid development of photochromic materials has made the preparation of photochromic textiles a key challenge. The traditional textile production process usually includes spinning into fibers, twisting into yarns, weaving into fabrics (knitting, weaving, embroidery or bonding), and finishing. The current strategies for preparing photochromic textiles mainly include combining photochromic materials and polymers through spinning technology to prepare functional fibers or coating photochromic materials on the fiber surface through coating or deposition processes.

2.3.1.1 Spinning techniques

Fibers, as the basic units of textiles, can be more easily prepared and introduced with various functions. By introducing functional materials into fiber during the manufacturing process, they can be endowed with abilities such as beauty, protection, and conductivity[76]. Based on this, a large number of functional fibers for assembling wearable electronic products have been developed[77-79]. Spinning technology can extrude a spinnable liquid into a jet by mixing functional materials and polymers and solidify it into fibers. Commonly used techniques include melt spinning, wet spinning, microfluidic spinning, thermal stretching, spinning, and solution extrusion (Figure 10) [80-82]. Many techniques have been used to incorporate functional nanomaterials into spinning solutions to prepare photochromic wearables.

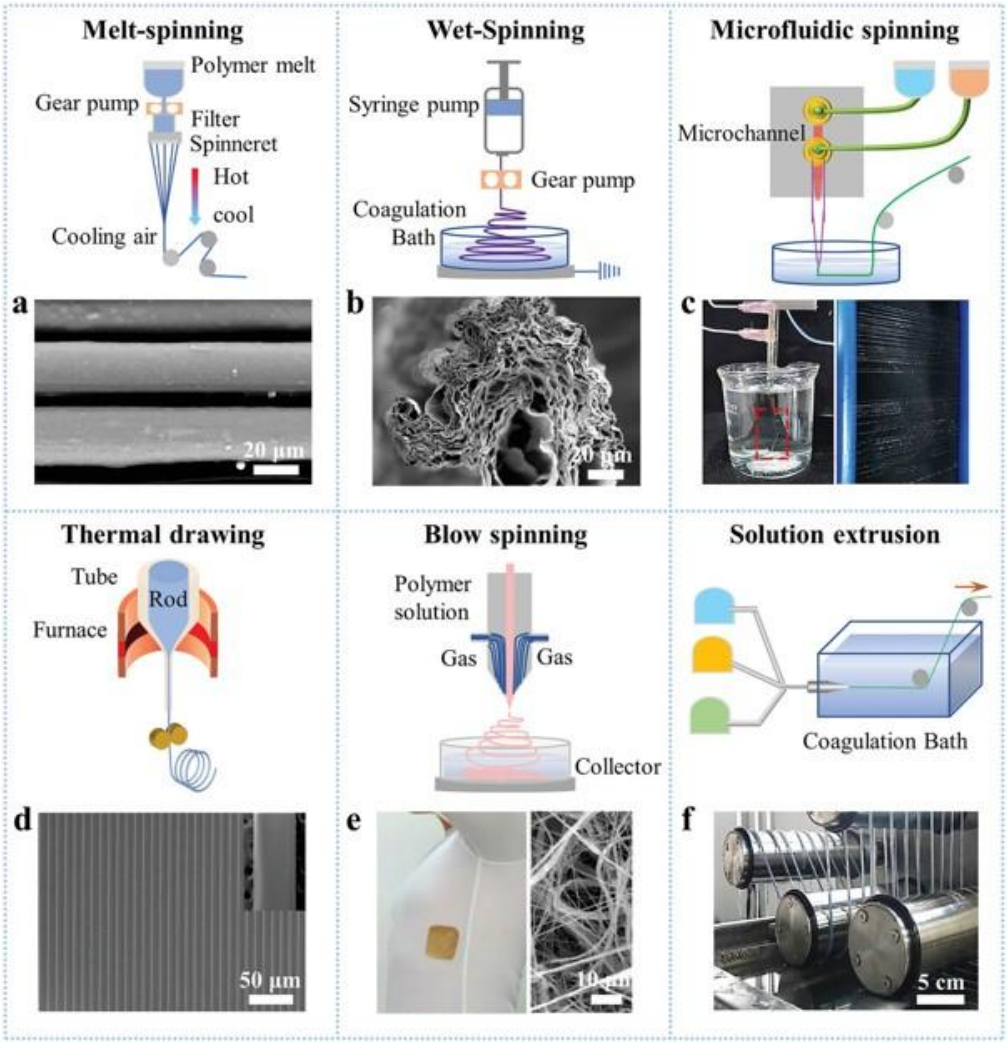

Figure 2.6 Schematic illustration of spinning techniques for Fabricating photochromic wearables. a) Melt-spinning technology[83]. b) Wet-spinning technology[84]. c) Microfluidic spinning technology[85]. d) Thermal drawing technology[86]. e) Blow-spinning technology[87]. f) Solution-extrusion method[88].

For example, a previous work employed electrospinning technology to introduce photochromic dyes into polycaprolactone (PCL) and successfully prepared photochromic fibers for UV sensing[89]. They used the fibers to construct different morphologies (such as artificial tattoos, leaves, and Wi-Fi icons), demonstrating their high UV sensitivity and ability to distinguish irradiation intensities (Figures 2.7a, b).

Furthermore, they developed a core-sheath structured yarn mixed with UV- and pH-responsive materials. Then yarns were embroidered into grape patterns on fabrics, and the patterns were made to appear purple (grapes) and green (leaves) under stimulation, demonstrating the potential for multi-responsive recognition. Another work reported using electrospinning method to prepare nanofibrous membranes made of amorphous WO_3 and polyvinylpyrrolidone (Figures 2.7 c, d)[90]. The membrane can be colored under UV light irradiation, and its coloration rate can be adjusted in a different oxidizing environment. The pattern can be repeatedly printed on the membrane using UV light, and the pattern can be maintained for several days and self-erased at room temperature. The resolution remains clear after repeated printing-erasing cycles for 40 times. This membrane with excellent photochromic properties and flexibility can be used as a rewritable medium to replace traditional fabric printing, contributing to environmental protection and sustainable development.

In addition, researchers used electrospinning technology to develop a nanofiber membrane for anti-counterfeiting using rare earth aluminate nanoparticles and polyethylene terephthalate (PET) (Figures 2.7e, f)[91]. The fluorescence activity of this flexible and elastic film remains stable under stretching. NREA@PET film can be used to produce anti-counterfeiting patterns that only appear under UV light, and has broad prospects in the fields of intellectual property protection, security printing, and military camouflage. Another research designed a sheath-core structure fiber based on electrospinning technology, modified polymethyl methacrylate (PMMA) nanofibers (Figure 2.7g)[92]. This fiber can quickly change color after UV irradiation in 1 min, and the color can be maintained for more than 4 h.

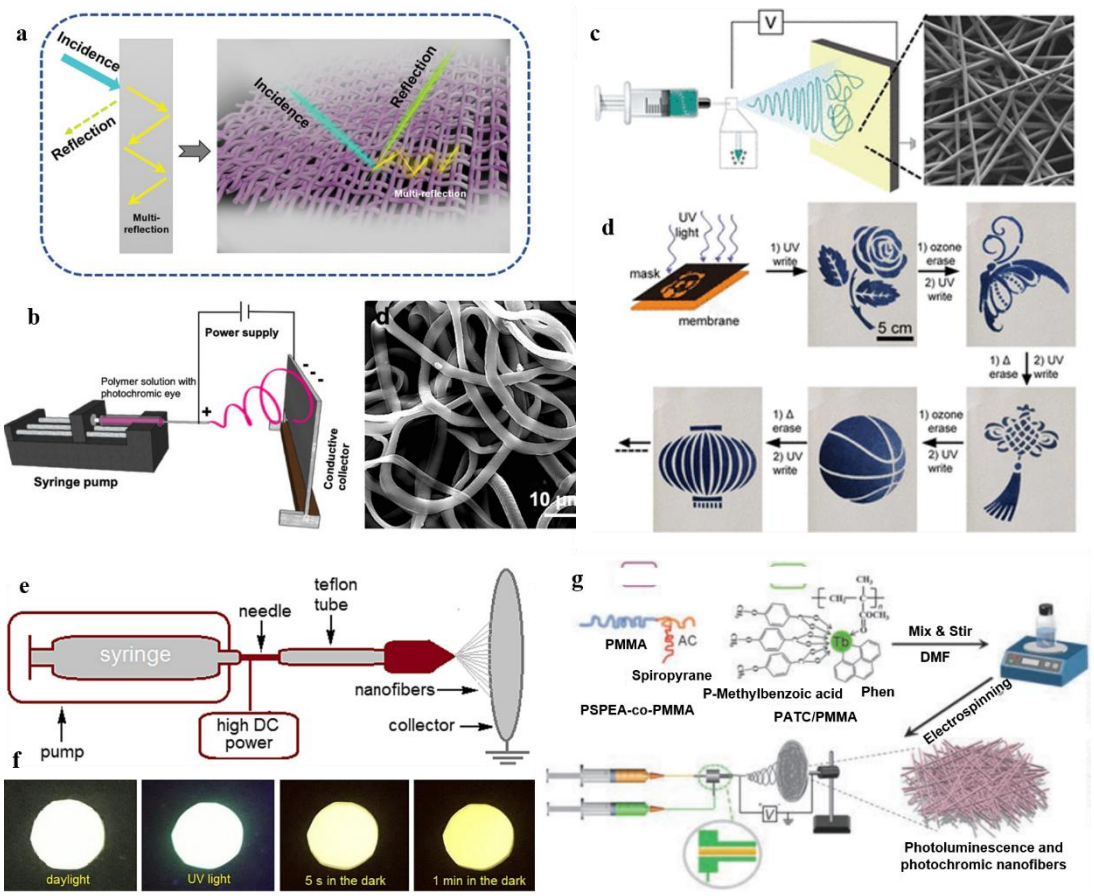

Figure 2.7 a) Illustration of fabric showing great color contrast. b) Schematic for fabricating PCL fiber through electrospinning[89]. c) Fabrication process of hybrid nanofibrous membranes using electrospinning technology. d) Various patterns were written and erased on the fabric[90]. e) Electrospinning method for preparing photochromic nanofibers. f) Color changes of rare earth aluminate nanoparticles@PET films under different light condition [91]. g) Diagram of preparation process of photochromic fabrics with sheath-core structure by electrospinning method[92].

2.3.1.2 Surface modification of textiles

A series of surface modification strategies for directly functionalizing textiles with photochromic properties have been developed, mainly including coating technology, deposition methods, and etching treatments. Dip coating (Figure 2.8) is widely used to

coat photochromic materials onto textiles to achieve the photochromic wearables[93-95].

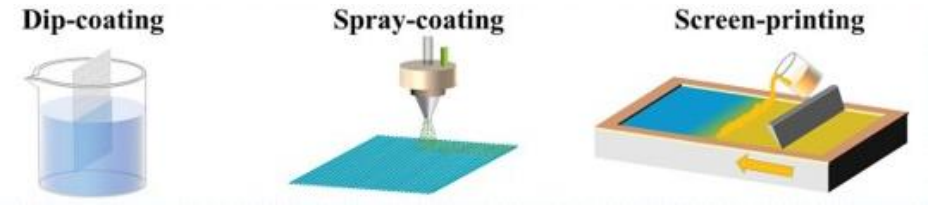

Figure 2.8 Various surface modification methods for photochromic textiles[22].

For instance, Gao et al. developed a photochromic cotton fabric by covalently fixing SP molecules with a carboxy linking group (Figure 2.9a)[96]. These fabrics exhibited excellent photochromic properties including color change (from pale yellow to purple) and great durability (> 10 cycles). The strong covalent bond between photochromic materials and fabrics endows the fabrics with excellent washing fastness (> 5 washing times). Similarly, Fan et al. prepared cotton photochromic fabrics through a click chemistry method (Figure 2.9b), showing excellent photochromic properties, durability (> 20 cycles), and tri-stimulus response color changing[97]. The process involves the synthesis of photochromic compounds containing alkenyl end groups, followed by the introduction of thiol groups into cotton fabrics modified with 3-mercaptopropyltriethoxysilane, and finally the grafting based on the thiol-ene click reaction. The resulting photochromic cotton fabric has a fast color change response of picoseconds and can quickly recover to its original state under three different stimuli: heating, dark environment or green light irradiation. After 20 reversible cycles, its absorbance still remains at a high level (about from 0.8 to 0.6).

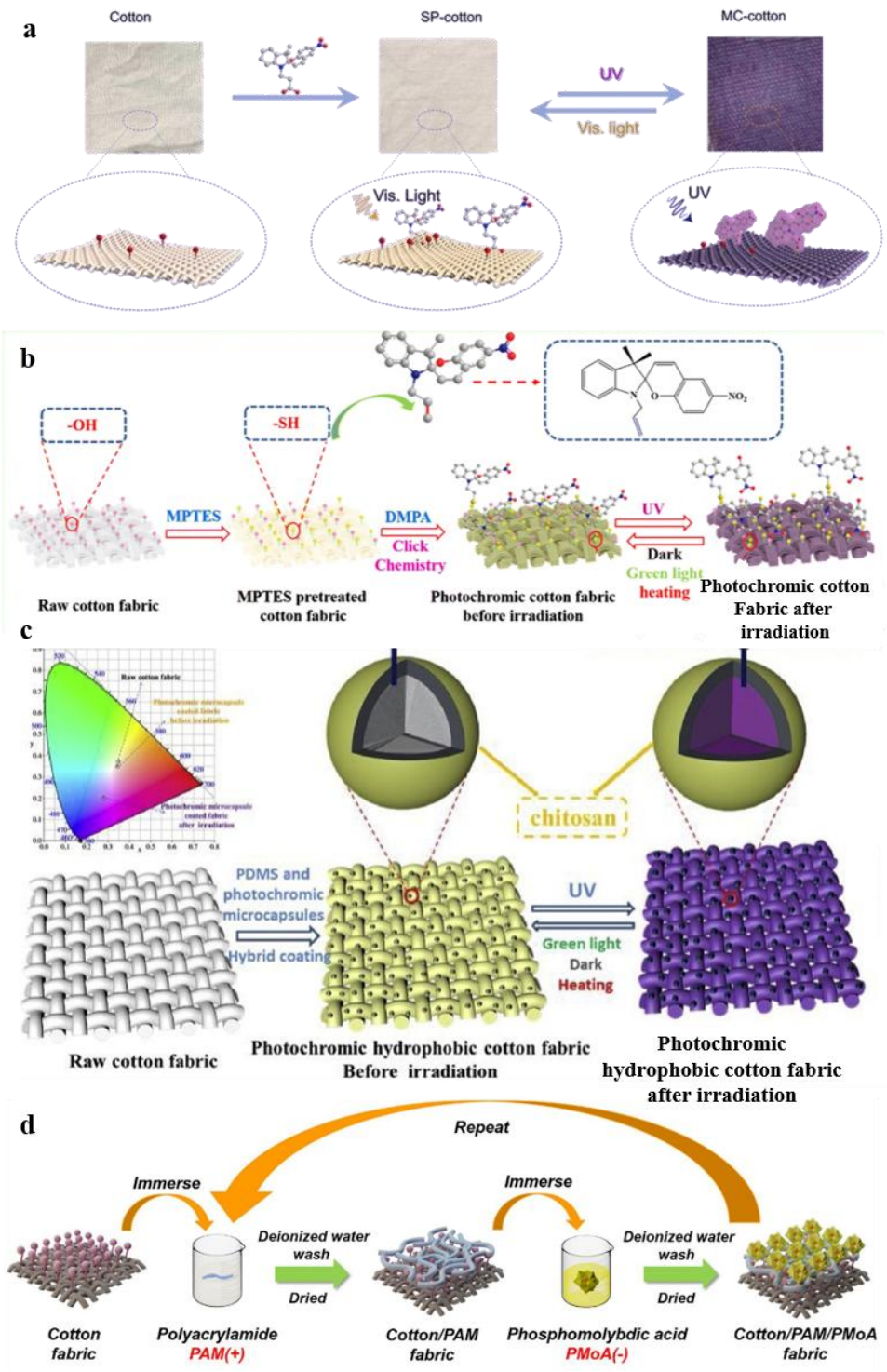

Figure 2.9 a) The fabrication procedure of SP-cotton fabric[96]. b) Schematic diagram showing the preparation process of photochromic cotton fabric[97]. c) The preparation procedure of microcapsule based photochromic cotton fabric[98]. d) Illustration of

photochromic cotton fabric prepared by self-assembly technology[73].

Another work reported cotton fabrics were modified by coating with photochromic microcapsules containing polydimethylsiloxane (PDMS) (Figure 2.9c) [98]. The fabric exhibits great photochromic properties such as fast color change (from light yellow to dark purple within 10 s) and color-fading rate (under 532 nm green light in 20 s). Meanwhile, the fabric exhibited good fatigue resistance (after 20 washing cycles) and long color retention time, indicating that it has excellent hydrophobic and antifouling effects. Another study prepared a new composite photochromic fabric (Figure 2.9d) by layer-by-layer self-assembly technology of phosphomolybdic acid (PMoA) and polyacrylamide (PAM)[73]. The fabric can quickly change from colorless to blue within 5 min under UV light and maintain excellent durability (>20 cycles). These photochromic textiles prepared based on surface modification strategies have broad prospects in practical applications due to their flexibility, wearability and potential stretchability, especially in the fields of optical information storage, chemical sensors, molecular switches, information security encryption and smart textiles.

2.3.2 Application of photochromic textiles

Photochromic textiles have great application potential in military uniforms, sensors, decorations, UV protection, information encryption, image storage and alarm protection owing to their ability to reversibly color change under UV light.

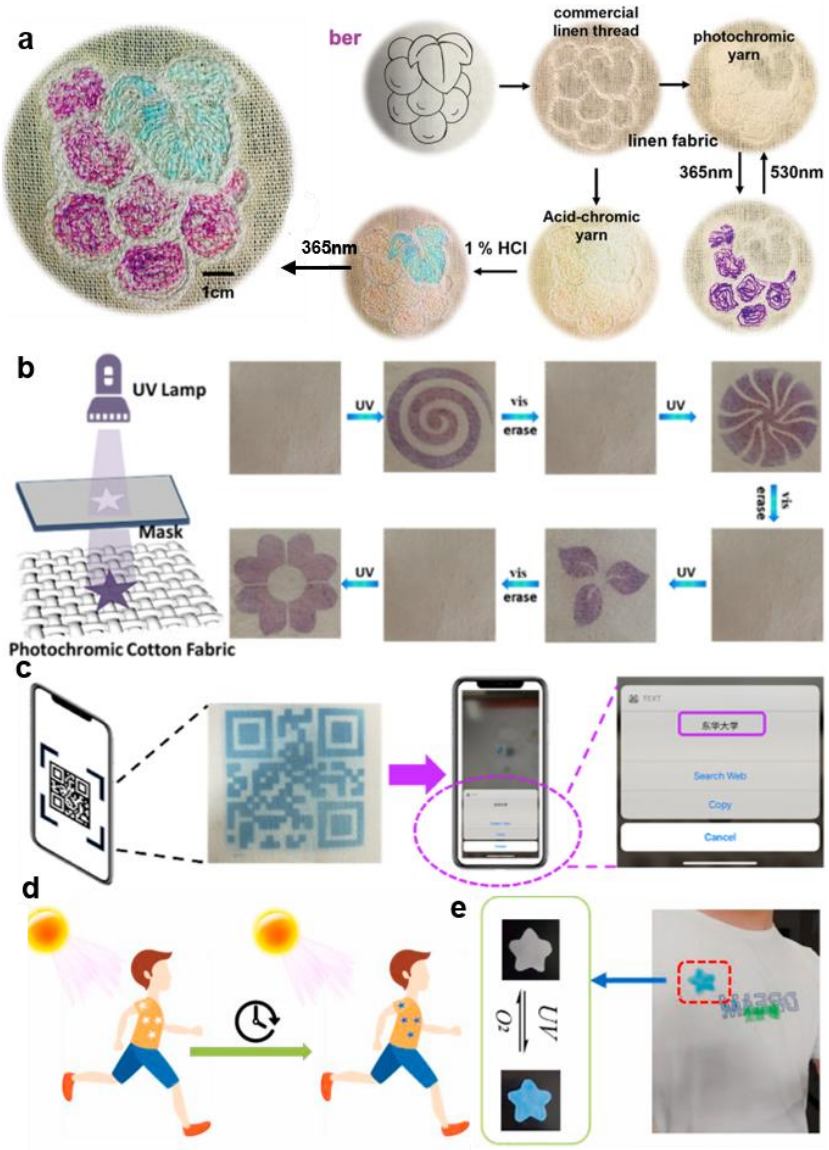

Figure 2.10 a) UV- and pH-responsive embroidered grape pattern on linen[89]. b) Reversible image storage via UV coloration and visible-light erasure[99]. c) QR code encryption on photochromic cotton for information storage[100]. d) The self-adhesive label was attached to clothing for UV detecting. e) The label on the volunteer's clothing changed from white to blue under UV irradiation[101].

Figure 2.10a shows a sensor was prepared by templating electrospun PCL fibers doped with photochromic materials or embroidering yarns containing photochromic

cores and sheaths on commercial linen fabrics[89]. When exposed to UV light (365 nm), a purple grape pattern appears on the linen substrate, and its gray-brown background indicates the strong UV intensity of the environment. Although multi-parameter sensing in the environment has greater application potential, it is still challenging to achieve such sensors with high selectivity. In terms of information storage, Figure 2.10b designed photochromic cotton fabrics by combining photochromic microcapsules with sodium alginate (SA) through electrostatic layer-by-layer self-assembly technology[99]. This material can repeatedly record and erase various patterns under alternating irradiation of UV and visible light, showing the application prospects of erasable optical data storage. In addition, Qi et al. developed a photochromic fabric by modifying cotton fibers with 3-mercaptopropyltrimethoxysilane and covalently bonding them with spirooxazine[100]. As shown in Figure 2.10c, a QR code containing confidential information is printed on this fabric, which can be scanned and decrypted by a mobile device, providing a new idea for military camouflage (such as wearer authentication). This method significantly improves the security of information transmission and expands its application in information storage and encryption. In addition, a study used the hydrogen bond self-assembly of polyacrylic acid (PAA) and sodium decatungstate to prepare a flexible and lightweight solar UV detector that is compatible with cotton fabrics[101]. The self-adhesive label based on this composite fabric was attached to clothing (Figure 2.10d) to detect the intensity of solar UV rays. As shown in Figure 2.10e, the label on the volunteer's clothing changed from white to blue under UV irradiation, which helps people intuitively identify UV threats.

2.4 Biocompatible Wearable Electronics

With the rapid development of digital health, flexible electronic devices, particularly wearable and biocompatible sensors, have become a key technology driving transformation in the medical industry[102, 103]. These devices can continuously monitor multiple physiological parameters, such as heart rate, blood pressure, and electrophysiological signals, enabling early disease detection and long-term patient health management[104-108]. This improves diagnostic and treatment efficiency and reduces medical costs, making healthcare more convenient and affordable[109-111]. Compared to traditional rigid devices, flexible sensors, owing to their superior mechanical properties, can closely conform to the surface of human body or soft tissue[112-115]. This significantly improves measurement accuracy and comfort while reducing complications such as skin irritation and inflammatory response. The design of wearable electronic devices directly links biocompatibility to device applicability, safety, and user compliance. Currently, flexible, stretchable, and biocompatible materials such as medical-grade silicone, polylactic acid (PLA), and PCL are widely used. They facilitate stable operation of devices in dynamic environments and establish the material foundation for long-term health monitoring.

Furthermore, the advent of biodegradable materials has transformed wearable, biocompatible, and implantable electronic devices[116, 117]. This type of sensor can naturally degrade through metabolism in the body after completing its monitoring task, avoiding the need for secondary surgery for removal and reducing the risk of infection and long-term foreign body reactions[118]. It is particularly suitable for postoperative monitoring and interventional applications on sensitive tissues such as the nervous system. Advancements in materials science and micro-nanofabrication technology have enabled the new generation of biocompatible devices to integrate intelligent

sensing, wireless communication, and big data analysis, facilitating multi-parameter, non-invasive, continuous health monitoring and real-time feedback[119, 120]. In the future, as the demand for personalized medicine and remote health management continues to increase, biodegradable and biocompatible wearable electronic devices will further develop in the direction of intelligence, integration, and sustainability, not only strengthening their core position in the digital health platform but also providing key technical support for building a safe, efficient, and environmentally friendly health system.

2.5 Wearable Hydrogels (WHs)

Contemporary wearable sensors are architecturally categorized into fibrous networks, thin-film epidermal patches, and microfluidic systems, each conferring distinct advantages for digital health monitoring. Fibrous sensors, typically integrated into textiles, provide exceptional omnidirectional strain tolerance and breathable large-area coverage, yet exhibit signal drift during sustained biomechanical activity. Thin-film epidermal devices achieve ultra-conformable skin interfaces enabling clinical-grade electrophysiological sensing (e.g., ECG, EEG), though their utility is constrained by limited multi-analyte detection capabilities and adhesion failure under hydrous conditions. Microfluidic platforms facilitate continuous biomarker analysis in biofluids (sweat, interstitial fluid) but necessitate complex fluidic control and external analytical components. Functionally, these systems diverge into physical sensors (strain, pressure, temperature) with millisecond-level responsiveness for motion tracking, chemical sensors for real-time metabolite profiling, and multimodal architectures that integrate cross-domain sensing at the cost of increased power complexity. Collectively, these platforms advance decentralized health monitoring, yet inherent compromises in

interfacial stability, biocompatibility during prolonged wear, and functional integration persist as fundamental limitations.

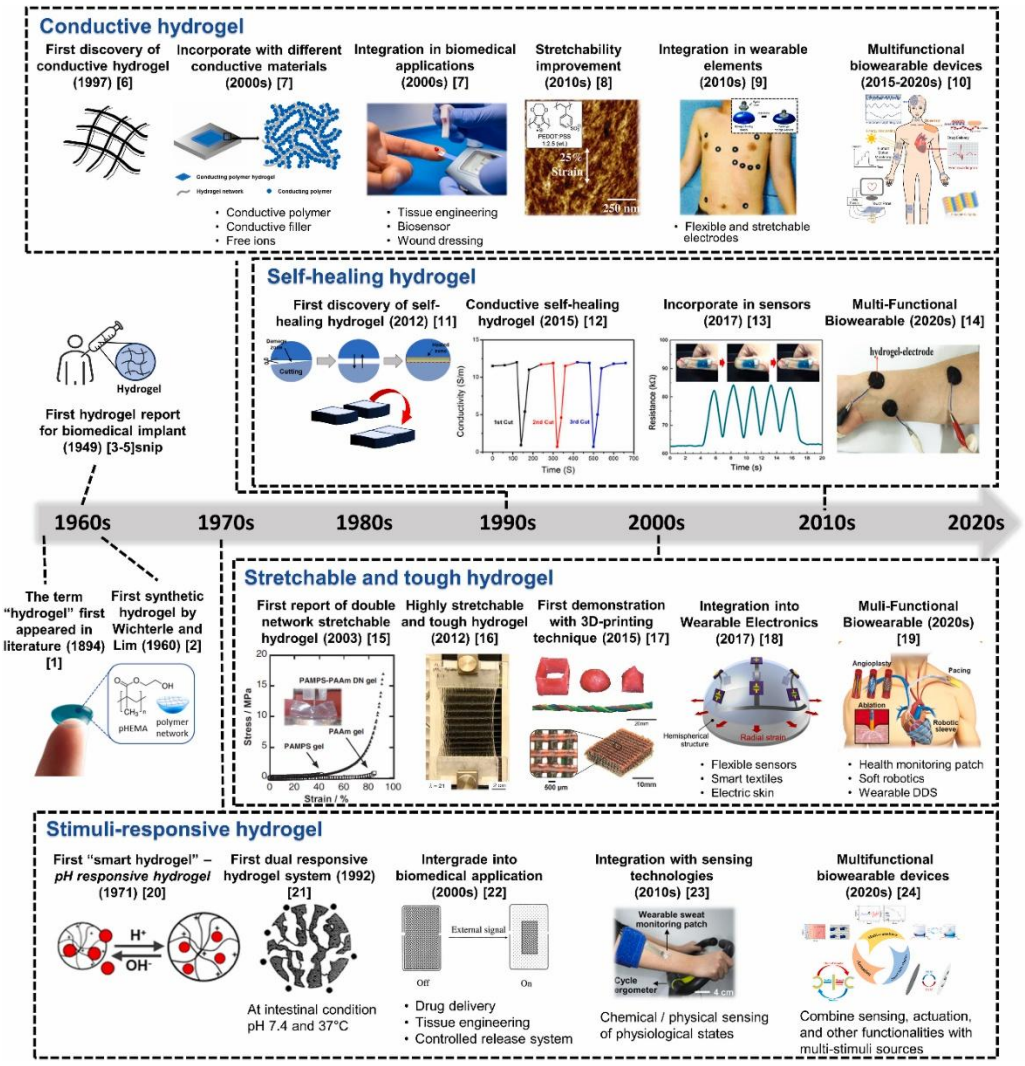

Figure 2.11 A chronological introduction to the development of functional hydrogels and their applications in wearable bioelectronics[121].

Hydrogel-based wearables exemplify a revolutionary wearable model, utilizing inherently porous, water-dense (>90%) structures derived from cross-linked hydrophilic polymers to address the essential constraints of traditional systems[122-124]. Their elastic properties, similar to human tissue (0.1–10 kPa), and ability to stretch a lot help reduce stress concentrations and motion artifacts when moving, which

are common problems in traditional thin-film sensors. Figure 2.11 sequentially delineates significant developing milestones: initiatives prior to 2000 concentrated on hydrogel innovation and fundamental biomedical applications, whilst advancements after 2000 facilitated intricate bioelectronic integration for wearable technologies[121]. Synthetic polymers such as PAA and PAM are popular in the market because they have great stretchability (about 1000% strain), while natural options like gelatin (about 200% strain) are much better for the environment since they can be renewed, are compatible with living tissues, and break down easily, meeting ecological needs. These materials harness attributes such as abundance, renewability, inherent biocompatibility, low cytotoxicity, degradability, and cost-effectiveness, aligning with growing environmental concerns and advancing sustainable soft matter design[125, 126].

The water-rich, biotransparent interface of hydrogel facilitates bidirectional metabolite and oxygen diffusion, ensure skin-attachability and good adhesion without causing inflammation or needing to be surgically removed later, reducing medical waste[127]. In addition, the nontoxic and biocompatible hydrogel sensors allow sensing equipment can even be safely implanted in the body for long periods. Implantable hydrogel-based strain sensors with complete degradability also can decompose naturally over time, thereby reducing superfluous medical consumption and multiple surgical operations, holding significance for facilitating early rehabilitation and repair. Their ion-conducting structures allow for multiple types of sensing (like detecting strain and biochemical changes), making them better than traditional sensors. Supramolecular cross-linking also allows the material to heal itself on its own (more than 95% effective), withstand different temperatures (from -20°C to 50°C), and stick to tissues, which helps prevent layers from separating in stiff devices[126, 128]. Future directions encompass closed-loop theragnostic, self-powering triboelectric, and low-

impedance brain interfaces for symbiotic human-device integration. Despite issues with ambient stability (<20 days) and scalable production, hydrogel technologies—especially gelatin-based systems—are poised to redefine wearables as adaptive, intelligent biomimetic interfaces rather than passive monitoring tools.

2.5.1 Classification of WHs

WHs can be developed by combining conductive materials with hydrogel or by combining the free ions and elastic polymer network. While the hydrogels could be classified into ionic hydrogels and electronic hydrogels according to the conductive substances (Figure 2.12).

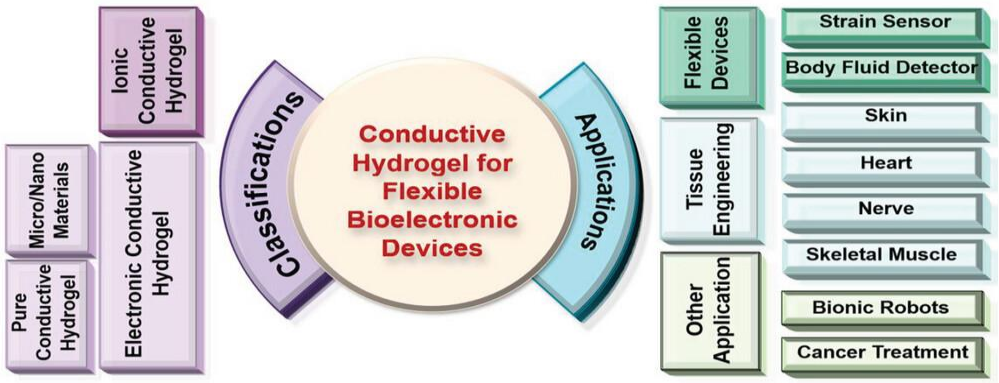

Figure 2.12 The classifications and applications of conductive hydrogels[126].

2.5.2 Ionic hydrogels

Ionic hydrogels represent an important advancement in connecting electronics with biological tissues, created to solve the differences in how traditional electronics and biological tissues work and feel[129, 130]. These materials incorporated mobile ions within an elastic, hydrated polymer network, achieving tissue-like softness, stretchability, and optical clarity. Their nanostructured matrix enables tunable ion diffusion, with pore architecture governing ionic mobility. This design, combined with customized chemical capabilities, facilitates selective ion interactions vital for biotic-

abiotic communication. Conductivity results from dissociated metal ions (e.g., Na^+, K^+) in the hydrogel's aqueous channels, which migrate directionally under applied electric fields[131]. The deformation of the hydrogel network dynamically alters ionic channels, resulting in variations in resistance. Simultaneously, electrostatic interactions between ions and charges in the polymer matrix significantly affect ion transport kinetics, which are essential for the sensing processes crucial for next-generation bio-integrated devices.

The previous study introduced an ionic and metal-ligand bonds hydrogel by combining the polyampholyte with multivalent metal-ion solutions (Figure 2.13a)[132]. This hydrogel has 200% strain, stable ionic conductivity (0.018 S/m at equilibrium), good self-recovery, and anti-fatigue behavior. The stable conductivity and mechanical robustness enable their use as highly stretchable strain sensors (gauge factor up to 2.43), effectively monitoring human motions like finger bending and wrist movement. Another research reported an ionic hydrogel was fabricated by using UV irradiation to polymerize N,N-dimethylacrylamide within ionic liquid-swollen polyelectrolyte microspheres (Figure 2.13b)[133]. This architecture conferred exceptional crack propagation insensitivity, a high fatigue threshold, and excellent stretchability (3000% strain). Reversible hydrogen/ionic bonds enabled rapid self-healing, full recyclability, wide-temperature stability, and ionic conductivity. This sensor can detect accurate physiological monitoring, facilitated by robust mechanical stability and adhesion. As shown in Figure 2.13c, Matsuda et al. developed resilient ionic double-network hydrogels, inspired by muscle training, which autonomously expand and fortify under continuous mechanical stress[134]. The technique utilizes mechanoradical generation via covalent bond cleavage in a brittle polyelectrolyte network (e.g., PNaAMPS) within a dual network architecture. Provided monomers participate in mechanoradical

polymerization at fracture locations, thereby repairing and fortifying the network without catastrophic failure. This procedure, conducted with a continuous monomer supply in an open system, facilitates substantial cyclic strengthening and size augmentation. Applications include creating specially designed features using mechanical stamping (like heat-sensitive patterns) and making flexible materials for soft robotics. Figure 2.13d displays a 3D-printable ionic double-network hydrogel scaffold containing alginate and PAM for single-stage craniectomy-cranioplasty in traumatic brain injury[135]. In vivo, Ca^{2+}-enriched scaffolds promoted accelerated cranial bone regeneration (140% higher osteopontin expression vs. controls) and degraded safely within 8 weeks. This bioactive design overcomes limitations of rigid implants by combining intracranial pressure compliance with osteoconductive functionality, enabling integrated brain protection and skull reconstruction.

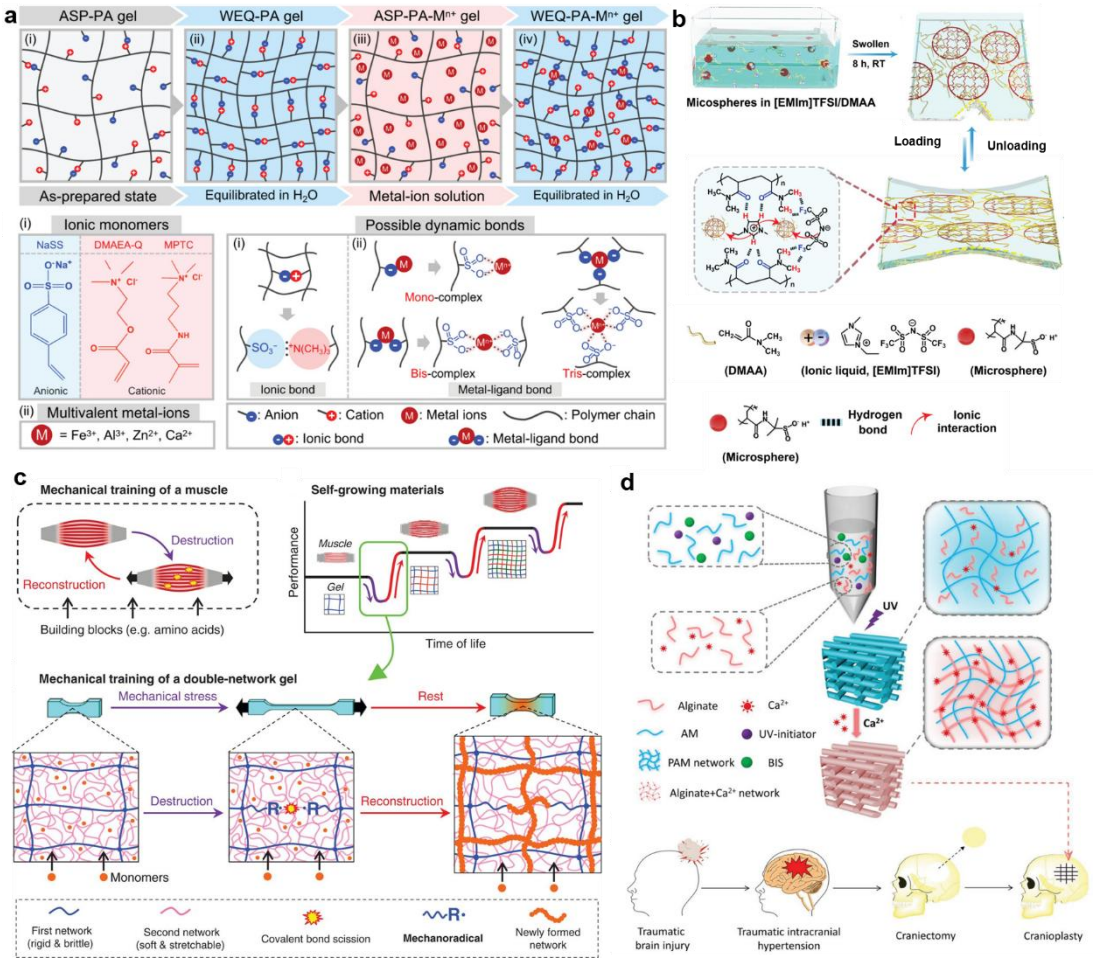

Figure 2.13 a) An ionic and metal-ligand bonds hydrogel was developed by combining the polyampholyte with multivalent metal-ion solutions[132]. b) The tensile deformation diagram of covalently cross-linked hydrogel with entanglement instead of the host material[133]. c) Schematic diagram of breaking and regenerating of the ionic double-network hydrogels, inspired by muscle training [134]. d) A 3D-printable ionic double-network hydrogel scaffold containing alginate and PAM [135].

2.5.3 Electronic hydrogels

Electronic hydrogels achieve conductivity through intrinsically conductive polymers (e.g., PEDOT: PSS) with conjugated chains, or via conductive fillers

(graphene, CNTs, metals) forming percolation networks. These systems enhance conductivity by orders of magnitude while preserving essential hydrogel properties: hydration, biocompatibility, and tissue-like mechanics. Electrical characteristics are tunable through filler selection and dispersion. The integration of electronic pathways within ion-permeable matrices enables direct bioelectronic interfacing for enhanced sensing, stimulation, and recording applications.

Hu et al. designed an electronic hydrogel by encapsulating EGaIn liquid metal (LM) with graphene oxide nanosheets to form core–shell nanofillers (Figure 2.14a)[136]. Ultrasonication enabled GO coordination with Ga^{3+}, creating a stable shell that prevented LM leakage while facilitating hydrogen bonding with PAM/SA networks. The composite achieved 303 kPa tensile strength at 1240% elongation, 0.036 S m^{-1} conductivity, and notch insensitivity. The shear-thinning hydrogel exhibited rapid self-healing (6 s) and strain-dependent piezo resistivity (GF = 4.56 beyond 900% strain), enabling 3D-printed tactile sensors for motion detection and spatial pressure mapping. Also, Lin et al. developed ionic-electronic hybrid $Ti_3C_2T_x$ MXene hydrogels for high-voltage supercapacitors by vacuum filtration and ionic liquid immersion (Figure 2.14b)[137]. The ion accessibility in the disordered MXene structure enable the hydrogel with 70 F g^{-1} capacitance at 3 V-10× higher than dried films—with rectangular CVs maintained up to 500 mV s^{-1}. This hydrogel architecture facilitated rapid $EMI^+/TFSI^-$ transport, achieving 80% capacitance retention after 1,000 cycles. This strategy unlocks MXene for high-energy-density storage in nonaqueous electrolytes. Lu et al. prepared pure PEDOT:PSS hydrogels via an additive-assisted method involving dimethyl sulfoxide addition, controlled dry-annealing, and rehydration (Figure 2.14c)[138]. The resultant hydrogels exhibit high electrical conductivity, high stretchability, and excellent long-term stability in physiological environments. These

properties make them highly promising for bioelectronic interfaces like neural implants and biosensors.

Ohm et al. developed a silver-PAM-alginate hydrogel by embedding the silver flakes in the hydrogel matrix, showing high electrical conductivity (>350 S cm^{-1}), low Young's modulus <10 kPa, high stretchability (>250% strain) (Figure 2.14d)[139]. This sensor can be applied to a high-current soft robotic stingray swimmer and neuromuscular stimulation electrodes, leveraging the composite's ability to deliver direct current and conform to biological tissues. The material bridges the gap between metallic conductivity and hydrogel softness for bioelectronics and wearable devices.

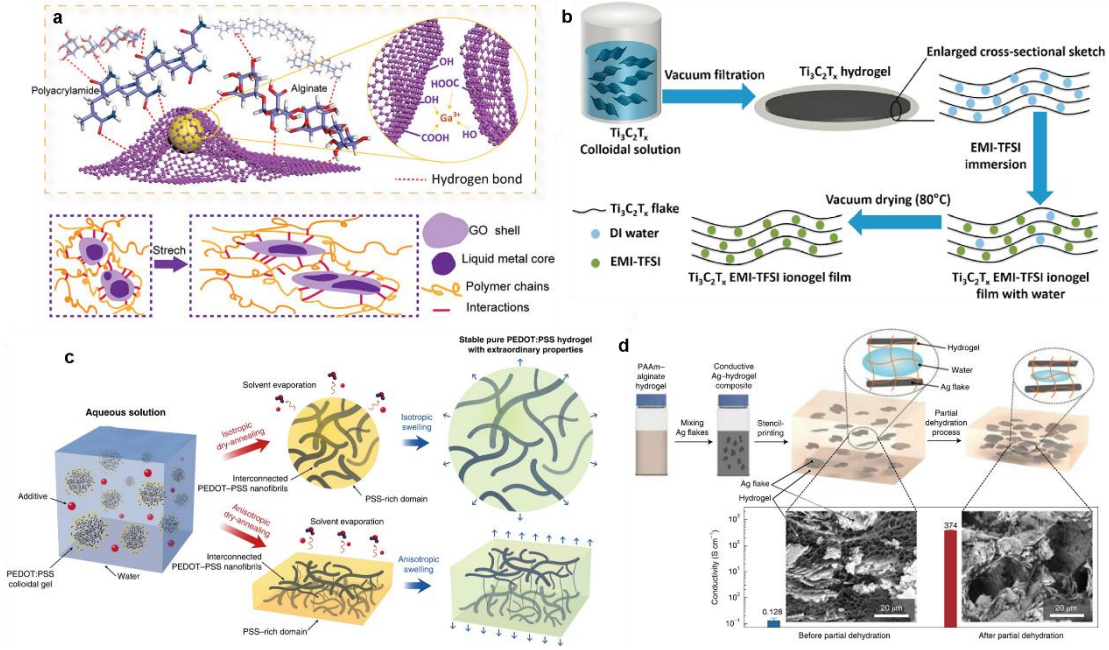

Figure 2.14 a) Illustration of LM and GO nanomaterials forming a P-LMGO hydrogel[136]. b) Schematic of fabrication procedure of ionic-electronic hybrid $Ti_3C_2T_x$ MXene hydrogels[137]. c) The preparation process of pure PEDOT:PSS hydrogels[138]. d) Schematic diagram of the synthesis of a silver-PAM-alginate hydrogel[139].

2.5.4 Application of wearable hydrogel

In bioelectronics, the movement state, biochemical information (pH, glucose, hypoxia, and other biomolecules), and electrophysiological signals (ECG, EEG, and EMG) of human bodies and organs can be monitored and collected, which would provide great information feedback and auxiliary medical treatment. Due to the excellent biocompatibility, tissue adhesion (on-demand adhesion) and coordinated mechanical flexibility, the conductive hydrogel has been widely studied and shows great potential in flexible devices, tissue engineering, implanted devices in vivo, human–computer interaction, soft robots, and so on.

The integration of skin-attached, WH sensors upon various body locations enables real-time monitoring of physical dynamics, encompassing a series of deformations from the small to the pronounced. A previous research has unveiled microgels was attached to limbs to sense the muscle movements[140]. As the finger bent through a range of angles (0°, 30°, 60°, and 90°) and wrist bent in different speed (Figure 2.15a), the sensor showed gradual and ladder-shaped changes in relative resistance. Also, with repetitive leg actions (Figure 2.15b), the resistance change reveals a reduplicative pattern, accurately discriminating the movements based on the response frequency and intensity of the sensor. The sensor can identify finger, wrist, and leg bending, showing great potential in health management for athletes. WHs have been applied to perceive and understand their surrounding environments, allowing for more accurate object grasping. Shen et al. developed an ultra-capacitive ion gel touch skin by laminating PAM-NaCl hydrogels with conductive fabrics, encapsulated in elastomers (Figure 2.15c)[141]. The skin enabled physiological monitoring of carotid pulses and respiration when worn on human subjects. Integrated into a soft bionic hand, it provided real-time tactile feedback for handling delicate objects and enabled dynamic interaction

recognition. In addition, hydrogels can be used in wireless soft microrobots to achieve controlled drug release and lesion detection in vivo. Lee et al. developed an octopus-inspired hydrogel adhesion robot utilizing two-photon 3D microprinting (Figure 2.15d)[142]. The design attains robust wet tissue adhesion (⩽16 mN) via a suction mechanism, while the LCST characteristics of pNIPAM facilitate on-demand separation through magnetic heating (32% volume reduction at 45°C). The magnetically driven robot demonstrates precise adherence to pig tissues in vitro and accomplishes reversible attachment-detachment cycles, advantageous for minimally invasive biomedical applications like localized medication delivery. And the WH system can be used to evaluate the electrical impulse propagation across the scarred tissue and its efficacy in reducing cardiac arrhythmia and preserving ventricular function. An injectable self-doped conductive hydrogel, produced through the grafting of poly-3-amino-4-methoxybenzoic acid onto gelatin and cross-linked with carbodiimide (Figure 2.15e), is capable of restoring electrical impulse propagation in myocardial infarction (MI) scars[143]. Upon injection into rat myocardial infarction scars, the hydrogel connected isolated cardiomyocytes, facilitated synchronous contraction, diminished arrhythmia occurrence, and preserved ventricular function. This method demonstrates therapeutic potential for preventing arrhythmias and cardiac remodeling post-myocardial infarction by electrically linking scar tissue. Additionally, a self-driven cancer treatment system that integrates iron porphyrin covalent organic framework-coated carbon nanotubes through injectable PEDOT:PSS conductive hydrogels was developed (Figure 2.15f)[144]. The hydrogel enhanced tumor aggregation and reduced electrical impedance, while the electric pulses (30 V, 3.5 Hz) generated by the TENG polarized the nanozymes, increasing the peroxidase-like activity of hydroxyl radical production by four times. In mice with 4T1 tumors, the

system was able to reduce tumor size by 83.6% after just one treatment, and it completely eliminated the tumor in 33% of the cases. This approach achieves efficient, autonomously administered catalytic therapy through electron polarization driven by human motion (Figure 2.15g).

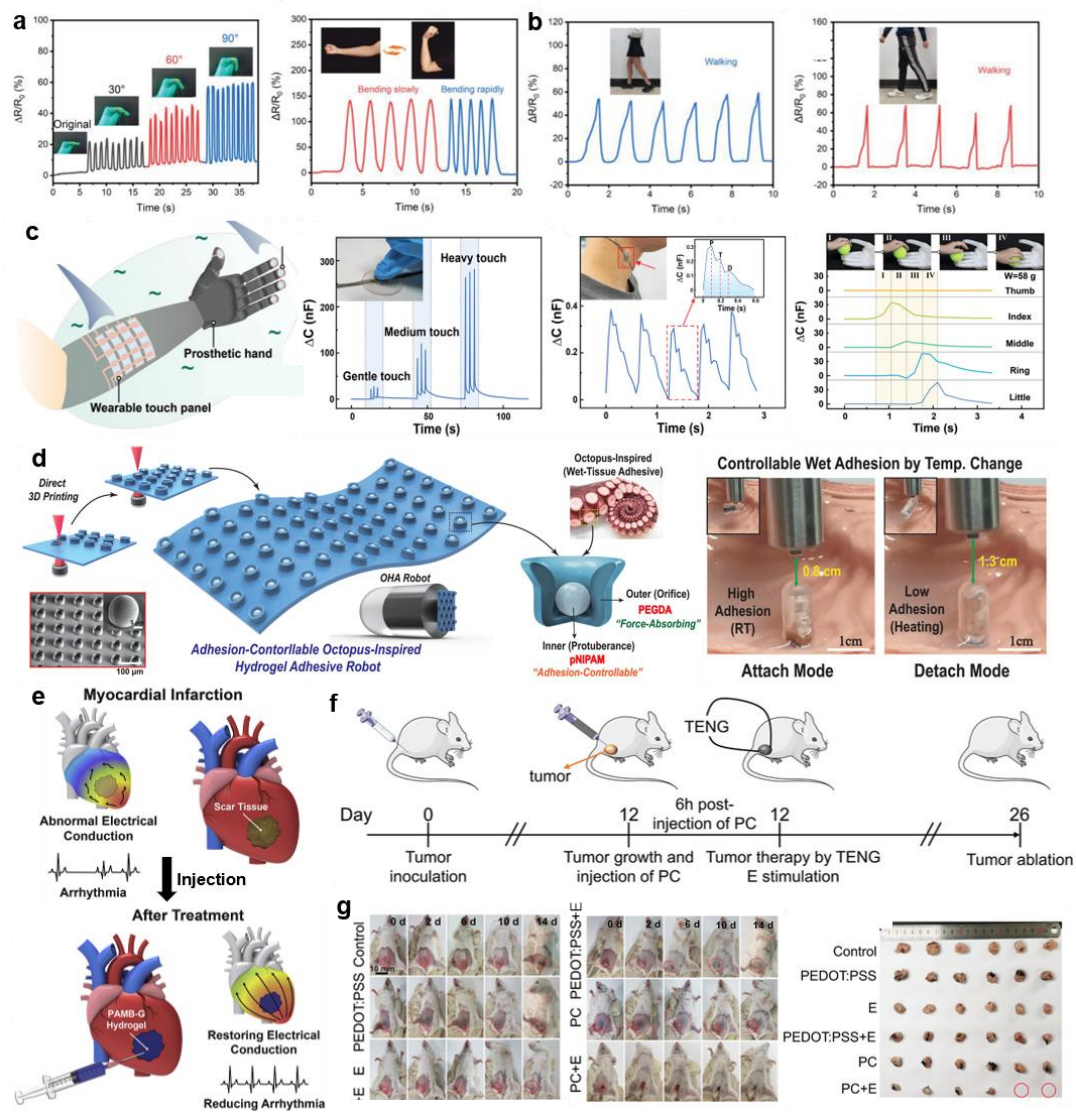

Figure 2.15 a) Detection of finger and wrist motions via microgels. b) Detections of walking and running via microgels attached on the knee surface[140]. c) Schematic of the PAM-NaCl hydrogels integrated into a soft bionic hand for monitoring of carotid pulses and respiration, real-time tactile feedback[141]. d) An octopus-inspired hydrogel

can be precisely adherent to pig tissues[142]. e) A self-doped conductive hydrogel was injected into rat myocardial infarction scars[143]. f) Treatment of cancer in tumor mice[144].

Chapter 3. Research of Methodology

3.1 Scalable, Fast Light-responsive, and Excellent Color-retention Fiber-based Photochromic Wearables for Sustainable Photo-patterning and Information Security Encryption

3.1.1 Materials

Cotton fabric was purchased from Suqian Fina Trading Co., Ltd., China. Ammonium molybdate ($(NH_4)_2MoO_4$), Ammonium heptamolybdate ($(NH_4)_6Mo_7O_{24}$), Sodium molybdate (Na_2MoO_4), and polyoxyethylene octyl phenol ether-10 (OP-10) were provided by Shanghai Macklin Biochemical Technology Co., Ltd. Ethylenediamine tetraacetic acid (EDTA), N-butyl acrylate (BA), ammonium persulfate (APS), and styrene (St) were obtained from Shanghai Aladdin Biochemical Technology Co., Ltd., China. Hydrochloric acid (HCl, 38%), ethanol alcohol, sodium hydroxide (NaOH), sodium bicarbonate ($NaHCO_3$), and hexadecyltrimethoxysilane (HDTMS) were purchased from DIECKMANN. Vinyltrimethoxysilane (VTMS) and SDS were supplied by TCl (Shanghai) Development Co., Ltd., China. Artificial sweat was bought from Shenzhen Zhongwei Instrument Equipment Co., Ltd., China.

3.1.2 Preparation of MoO_3 nanoparticle

Three different molybdenum sources, namely $(NH_4)_2MoO_4$, $(NH_4)_6Mo_7O_{24}$ and Na_2MoO_4, were used to synthesize MoO_3. To prepare MoO_3 nanoparticles, a predetermined quantity of the molybdenum source was dissolved in 50 mL of deionized water, resulting in a solution with a concentration of 0.1 mol L^{-1}. Afterwards, an EDTA saturated solution (2 mL) was added to the mixture while stirring constantly at room temperature. The pH of the solution was subsequently modified to 1.5 using HCl

solution, while the combination was stirred in darkness for a duration of 4 h. Subsequently, the solution was transferred to a 100 mL autoclave and subjected to hydrothermal treatment at a temperature of 120°C for 2 days. After the treatment, the light blue precipitates were gathered and washed with distilled water and ethanol to eliminate contaminants. Ultimately, the solid particles were dehydrated using a vacuum at a temperature of 50°C, resulting in the production of MoO_3 nanoparticles.

3.1.3 Preparation of MoO_3-based self-synthesized polymer network (MSPN) solution

The synthesized MoO_3 was dispersed in a mixture of the St (7.5 g), BA (7.5 g), and VTMS (0.6 g). Next, the necessary quantities of OP-10 (0.15 g), SDS (0.3 g), and $NaHCO_3$ (0.15 g) were dissolved into 45 mL of deionized water. This mixture was subjected to ultrasonic stirring to form a pre-emulsion. Subsequently, the pre-emulsion and aqueous solution (5 mL) containing APS (0.15 g) were continuously dropped into a round-bottom flask with N_2 and a mechanical stirrer and stirred at 80°C. The reaction was allowed to proceed for 3 h before cooling to room temperature, resulting in the formation of the MSPN solution.

3.1.4 Preparation of MoO_3 self-synthesized polymer network-based photochromic textiles (MSPPTs)

Initially, the knitted cotton fabrics were treated with a 20 g L^{-1} NaOH solution to remove impurities and introduce more functional groups on the fiber surface. Then, cotton fabrics were modified using MSPN solutions containing varying concentrations of MoO_3 nanoparticles (ranging from 1.5-10 mg mL^{-1}) through the pad-dyeing method. Next, place the treated fabrics in an oven for 6 hours at 60°C, and this process needs to

be repeated 1-4 times. After that, HDTMS (1%) was used to treat MSPN-coated fabrics, and MSPPTs were obtained.

3.1.5 Characterization and measurements

The morphologies of the cotton fabrics before and after treatment were examined using Field Emission Scanning Electron Microscopy (SEM, Tescan MIRA). The transmission electron microscope (TEM) was employed to investigate the morphologies of MoO_3 nanoparticles. The crystal structure and phase composition of the prepared MoO_3 nanoparticles were analyzed by X-ray diffraction (XRD) pattern (Rigaku SmartLab). Fourier transform infrared spectroscopy (FT-IR) was utilized to characterize the structure of the pristine cotton fabrics, MSPN-coated fabrics, and MSPPTs. Mechanical properties of samples were assessed using a universal material testing machine (3365, Instron, USA). The surface hydrophilicity of the fabrics was measured with an optical contact angle measuring device (SDC-350). Elemental content and distribution of samples were analyzed using Energy Disperse Spectroscopy (EDS). Thermal gravimetric analysis (TGA) was conducted to determine the content of the pristine cotton fabrics, MSPN-coated fabrics, and MSPPTs. The air permeability ($mm\ s^{-1}$) of fabrics before and after functionalization was measured using a MO21S air permeability tester (KES, Kato Tech Co., Ltd.) following the ASTM D737-08 standard. The washing fastness of photochromic textiles was evaluated following the AATCC TM 135-2004 standard. The abrasion resistance test based on ASTM D4966 standard was performed to investigate the durability of MSPPTs during long-term wear, and the samples were abraded for 10,000 cycles with pressure of 9 ± 0.2 kPa. The skin allergic reaction test was evaluated by attaching photochromic fabrics to the forearm of a volunteer (one author of this paper) and informed written consent was also obtained from the volunteer. The absorption spectra of samples were recorded by a UV−vis

spectrophotometer (Agilent Cary 300 Conc). Color difference (ΔE) and CIE coordinate diagrams of MSPPTs were evaluated by Macbeth Color-Eye 7000A (Dearly Enterprise Limited, China) under CIE standard illuminant D65 and 10° standard chromaticity. The cytotoxicity of photochromic fabrics was conducted by using L-929 cells (ATCC, US) based on CCK-8 assay.

3.2 Sustainable Photochromic Wearables with Excellent Retention and Superior Stability for Customizable Patterns and Information Security Encryption

3.2.1 Materials

Cotton fabric was purchased from Suqian Fina Trading Co., Ltd., China. Na_2MoO_4 was provided by Shanghai Macklin Biochemical Technology Co., Ltd. EDTA and Glycidoxypropyltrimethoxysilane (KH560) were obtained from Shanghai Aladdin Biochemical Technology Co., Ltd., China. Chitosan, Tween 80, glutaraldehyde (GA) solution 25%, acetic acid, petroleum ether, SA, ethanol alcohol, NaOH, HCl (38%), $NaHCO_3$, sodium chloroacetate, acetone, and potassium persulfate ($K_2S_2O_8$) were purchased from DIECKMANN. Artificial sweat was bought from Shenzhen Zhongwei Instrument Equipment Co., Ltd., China.

3.2.2 Preparation of MoO_3 nanoparticle

To prepare MoO_3 nanoparticles, a predetermined quantity of Na_2MoO_4 was dissolved in 50 mL of deionized water to form a solution with a concentration of 0.1 mol/L. Afterwards, a saturated solution of EDTA (2 mL) was introduced into this mixture while stirring constantly at room temperature. The pH of the solution was subsequently modified to 1.5 using HCl, while the combination was stirred in the

absence of light for a duration of 4 h. Subsequently, the solution was put into a 100-mL autoclave and exposed to hydrothermal treatment at a temperature of 120°C for 48 h. Following the treatment, the light blue MoO_3 nanoparticles were gathered and underwent multiple washes using distilled water and ethanol alcohol to eliminate any contaminants. After that, the MoO_3 nanoparticles (1 g) were evenly distributed in a 200-mL solution of 0.3% acetic acid, which was mixed with 1.2 g of chitosan and 4 g of tween 80. Next, the mixture was subjected to ultrasonic treatment for 3 h, and then the cell grinder was used to grind the mixture for 30 min. Afterwards, a 4 mL solution of GA was dropped and constantly stirred for 4 h to chemically bond the chitosan and solidify the microcapsule. The MoO_3 microcapsule (MM) nanoparticles were ultimately centrifuged and washed with petroleum ether with a volume percentage of 30%.

3.2.3 Preparation of SAME-PCF

Initially, the knitted cotton fabrics were treated with a 20 g/L NaOH solution to remove oil and impurities, and enhance the presence of additional functional groups on the fiber surface. Next, cotton fabrics were immersed in a solution of KH-560 with a concentration of 1.5% at a temperature of 60°C for 12 h. The fabrics were then cleaned using acetone and distilled water, resulting in the production of the Epoxy PCFs (E-PCFs). After the treatment, place the treated fabrics at a 60°C to dry for 4 h. Afterwards, separately prepare a solution of MM nanoparticles (with concentrations ranging from 5-20 mg/mL) and a solution of SA (5 mg/mL). The PH values of both solutions were adjusted to 5. Subsequently, the E-PCFs were immersed into a solution of MM nanoparticles for 4 h. They were then dried at a temperature of 60°C for 4 h, resulting in the formation of the MM/Epoxy PCFs (ME-PCFs). Afterwards, the ME-PCFs were submerged in a solution of the SA for 30 min and subsequently subjected to a drying

process at a temperature of 60°C for 4 h. Ultimately, this procedure needs to be replicated 1-4 times in order to prepare the SAME-PCF.

3.2.4 Characterization and measurements

The surface morphology of these fabrics, MoO_3 nanoparticles, and MM nanoparticles were investigated by SEM. The morphology of MoO_3 nanoparticles was examined using a TEM. XRD technique was used to study the crystal structure and phase composition of the MoO_3 nanoparticles and functionalized fabrics. X-ray photoelectron spectroscopy (XPS, Kratos Axis 165) was used to examine the valence changes of Mo atoms. The structure of the PCF, E-PCF, ME-PCF, and SAME-PCF was analyzed using FT-IR. The mechanical properties of the samples were evaluated using a universal material testing machine (3365, Instron, USA). The contact angle measurement equipment (SDC-350) was used to quantify the hydrophilicity of the textiles. The elemental composition and distribution of the samples were examined by using EDS mapping. The content of the PCF, E-PCF, ME-PCF, and SAME-PCF was measured by TGA. A MO21S air permeability tester (KES, Kato Tech Co., Ltd.) was used to measure the air permeability (mm s^{-1}) of fabrics depending on the ASTM D737-08 standard. The washing ability of photochromic fabrics was assessed in accordance with the AATCC TM 135-2004 standard. The UV-vis absorption spectra of the samples were measured using a UV-vis spectrophotometer (Agilent Cary 300 Conc). The color difference (ΔE) and CIE coordinate diagrams of photochromic fabrics were assessed using the Macbeth Color-Eye 7000A (Dearly Enterprise Limited, China) under the CIE standard illuminant D65 and 10° standard chromaticity. The cytotoxicity of photochromic fabrics was assessed using L-929 cells (ATCC, US) by the CCK-8 assay.

3.3 Highly Stretchable and Biocompatible Gelatin Biogels for Multifunctional Electronic Applications

3.3.1 Materials

Gelatin powder was purchased from Shanghai Aladdin Biochemical Technology Co., Ltd., China. Zinc pyrrolidone carboxylate (PCA-Zn) was provided by Shenzhen Xingkaiyue Biotechnology Co., Ltd. Xanthan gum (XG) was obtained from Shanghai Huhui Biotechnology Co., Ltd. Cellulose nanofiber was bought from Tianjin Woodelf Biotechnology Co., Ltd.

3.3.2 Preparation of biogel

Gelatin powder (1 g) was dissolved in deionized water (2 mL) and allowed to soak for 30 mins. Subsequently, PCA-Zn (0.2-0.7 g) was added to the solution under continuous stirring at 50°C for 30 mins. Nano-crystalline cellulose (0.1-0.7 g) was then incorporated, and the mixture was stirred for an additional 1 h. XG (0.08-0.36 g) was subsequently introduced, followed by further stirring for 1 h to ensure homogeneity. The resulting precursor solution was cast into a polytetrafluoroethylene (PTFE) mold of the desired geometry and cooled to room temperature (25°C) to form the biogel. For a 2 mL aliquot of the precursor solution, gelation occurred within approximately 1 min.

3.3.3 Characterization

The micromorphology and interface structure of the hydrogel were investigated by SEM (Tescan VEGA3). To prepare the samples, the hydrogels were freeze-dried for 48 h and then sliced in liquid nitrogen. XRD technique was used to study the crystal structure and phase composition of the hydrogels before and after functionalization. XPS (Kratos Axis 165) was used to examine the valence changes of Zn atoms. The

chemical structure of the hydrogels was analyzed using a Fourier transform infrared spectrometer (FTIR, Nicolet 6700, Thermo Fisher Scientific, USA) and a Raman spectroscopy (Jobin Yvon LabRam HR800) with a 632.8 nm laser wavelength. The content of the hydrogels was measured by TGA. Mechanical testing on hydrogels was performed using the Instron 5542 mechanical tester. 2 mL of the fluidic Hydrogels were created in the PTFE mold measuring 25 mm in length, 4 mm in width, and 2 mm in height. The electrical signals of hydrogels were measured by an electrometer (Keithley 6514 system). The skin allergic reaction test was evaluated by attaching hydrogels to the forearm of a volunteer (one author of this paper) and informed written consent was also obtained from the volunteer. The cytotoxicity of hydrogels was evaluated by using L929 cells (ATCC, US) by the CCK-8 assay.

3.3.4 Electrophysiological recordings

Electromyography (EMG), electrocardiography (ECG), electrooculography (EOG), and electroencephalography (EEG) signals were acquired using both biogel electrodes and commercial Ag/AgCl gel electrodes (3M) to enable comparative performance assessment. For each modality, three-channel recordings (positive, negative, and reference electrodes) were simultaneously obtained using both electrode types, as electrode positioning was found to have negligible influence on EEG signal quality. For EMG and ECG recordings, the biogel electrode was placed on the dorsum of the hand as the working electrode, with two additional biogel electrodes positioned on the forearm serving as reference electrodes. EOG signals were recorded by placing two biogel electrodes on the temples bilaterally as working electrodes and a third electrode below the ear as the reference. For EEG acquisition, two biogel electrodes were affixed to the forehead bilaterally as working electrodes, with a reference

electrode placed below the ear. All electrodes were interfaced with a device for signal acquisition and processing (Brain Products actiCHamp Plus amplifier).

3.3.5 In vivo biocompatibility studies

Animal experiments were approved by the Animal Care and Use Committee of Suzhou Huaxiao Biotechnology Co., Ltd. (IACUC-HX0201401). Eight Sprague-Dawley (SD) rats (8-week-old Sprague-Dawley rats, weighing 200 g) were used. The rats were divided into a control group and a material group. Prior to surgery, all animals underwent skin preparation, and three implantable sites were made in each animal, with a distance of more than 2 cm between adjacent sites. A longitudinal incision was performed at each site. The material was placed subcutaneously on the rat's back and sutured to the wound. In the control group, the epidermis was incised, but no materials were placed. Rats were sedated via a subcutaneous injection of 5 mg/kg Analgesia for three consecutive days after surgery. Wound recovery was assessed on days 3 and 14 after surgery, and the data were quantitatively analyzed using Image J software. Rats were sacrificed using exsanguinations with anesthesia on the 3rd and 14th days after surgery. Skin samples were collected postoperatively, embedded in paraffin, and sections were stained with hematoxylin and eosin (H&E) and Masson's trichrome.

3.4 Study Milestones

<table>
<tr><th colspan="2">First Academic Year</th><th colspan="2">Second Academic Year</th><th colspan="2">Third Academic Year</th></tr>
<tr><td>2022.09-2023.01</td><td>2023.01-2023.06</td><td>2023.06-2023.12</td><td>2023.12-2024.06</td><td>2024.06-2024.12</td><td>2024.12-2025.07</td></tr>
<tr><td>Literature review (Finished)</td><td colspan="4">Reading latest papers on sustainable and functional wearables for smart applications</td><td rowspan="4">Thesis writing & defense</td></tr>
<tr><td colspan="3">Scalable, Fast Light-responsive, and Excellent Color-retention Fiber-based Photochromic Wearables for Sustainable Photo-patterning and Information Security Encryption</td><td></td><td></td></tr>
<tr><td></td><td colspan="3">Sustainable Photochromic Wearables with Excellent Retention and Superior Stability for Customizable Patterns and Information Security Encryption</td><td></td></tr>
<tr><td></td><td></td><td colspan="3">Highly Stretchable and Biocompatible Gelatin Biogels for Multifunctional Electronic Applications</td></tr>
</table>

Figure 3.1 Study milestones.

Chapter 4. Scalable, Fast Light-responsive, and Excellent Color-retention Fiber-based Photochromic Wearables for Sustainable Photo-patterning and Information Security Encryption

4.1 Introduction

As the standard of living rises, individuals are becoming increasingly dependent on and demanding higher levels of customization and functionality in their apparel. The advancement of functional and intelligent wearable fiber-based devices in stimuli-switching devices, thermal-regulated textiles, wearable sensors, and antibacterial textiles has been greatly stimulated[12, 145-150]. People occasionally discard traditional garments after a short period of use due to their inflexible style and non-adjustable designs. This results in the squandering of significant expenses and substantial environmental contamination from garments undergoing intricate manufacturing procedures. Light-responsive textiles made with photochromic material have become ideal for reducing printing costs and addressing environmental problems. These textiles have attracted a growing attention worldwide owing to their attractive potential in the fields of optical data storage, switchable image information, photonic memory, information security encryption, sustainable photo-patterning information displays, and optoelectronic devices[151-153].

Photochromism is the reversible transformation of a chemical material between two forms that have different absorption spectra, leading to the transformation between different colors on fabrics[18, 154]. Various techniques have been proposed to develop fiber-based photochromic wearables with the merits of adaptability to the human body,

wearing capability, and reversible photo-patterning[155-158]. Nevertheless, the sustainable application of fiber-based photochromic wearables still faces a considerable challenge because of their limited scalability, color retention, stability, and response speed, resulting from complicated fabrication procedures, unavoidable environment changes, and deterioration of material properties. Attractive applications such as sustainable photo-patterning information storage and information security encryption not only require photochromic fabrics to acquire clear patterns in a short time and remain the patterns for a long term but also realize a rapid writing-erasing cycle as information needs to be converted. Long-term color retention is important in ensuring that the photochromic fabric remains vital and functional after repeated utilization and exposure to light. In addition, the quick reversible capabilities can ensure a stable and smooth transition between the writing and erasing state as well as providing a dynamic and sensitive wearing experience. Although there are some existing photochromic fabrics with good color retention, they rely on long-time and high-intensity UV irradiation to write patterns and the patterns are difficult to erase, hindering the utilization and development of photochromic wearables in the realm of daily wearing, reversible image storage, and information security encryption. Furthermore, converting the color of photochromic fabrics typically necessitates the utilization of complex equipment (e.g., a laboratory oven and green light) or hazardous oxidants (e.g., potassium persulfate solution and O_3) that are not easily accessible for home use. Therefore, it is highly desirable to develop an environmentally friendly and scalable photochromic wearable with exceptional color retention and rapid color-reversible capabilities for sustainable photo-patterning and information security encryption applications, which can further promote the commercialization and popularization of photochromic fabrics.

Photochromic materials, encompassing organic molecules like SPs, spirooxazines, DAEs and azobenzenes[154, 159], transition metal oxides like tungsten trioxide, Molybdenum trioxide (MoO_3), zinc oxide[160-162], and polyoxometalates like phosphomolybdic acid[73], have been extensively integrated with flexible substrates for fabrication of advanced photochromic devices. Compared with tungsten trioxide and zinc oxide, MoO_3 is an n-type semiconductor characterized by a wider band gap and deeper charge carrier traps. These properties result in more pronounced color changes and longer colored states, making MoO_3 renowned for its applications in photochromic and electrochromic systems, catalysis, sensors, and organic solar cells[163-165]. MoO_3 exhibits exceptional photochromic performances, including significant coloration efficiency, rapid and reversible color changes, long color retention, and excellent fatigue resistance[166-168], rendering it an ideal candidate for photochromic applications. Extensive research on MoO_3 mainly focuses on its structure optimization[169], catalysis[170], composite reinforcing materials[171], and electronics[172]. However, the application of MoO_3 in photochromic wearables has not been reported until now and remains a considerable challenge. During long-term wearing and usage, frequent writing-erasing cycles and washing can constantly degrade the photochromic properties of these fabrics. Strong adhesion between the fabric and photochromic materials is indispensable to withstand damage from harsh environments and multiple writing-erasing cycles. Besides, MoO_3, an acidic molybdenum oxide, undergoes a neutralization reaction under alkaline conditions, generating molybdate and water, which results in the loss of its photochromic properties. Detergents like alkaline solutions (pH > 8) can completely eliminate the photochromic capabilities of MoO_3. Under the action of a crosslinking agent, polymer monomers can form a crosslinking network, which limits MoO_3 nanoparticles in the narrow space of the

polymer and effectively provides tight polymer encapsulation to avoid external damage. Additionally, by increasing spatial hindrance, hydrophobic agents can further encapsulate and protect MoO_3 nanoparticles against the chemical destruction from alkaline solutions. Therefore, it is urgent to develop a kind of photochromic fabric based on MoO_3 that can maintain a stable light stimulus response and great photochromic performance after experiencing frequent color-switching, washing, and complicated environmental changes.

In this chapter, MSPPTs are designed and prepared by integrating MSPN and long chain silyl group to cotton fabrics. This photochromic fabric shows great reversible color change (from pale yellow to blue), rapid light response (reaching color saturation with a UV dose of 60 kJ m^{-2}), outstanding color retention capability (> 90 days), and excellent fatigue resistance (> 40 cycles). Additionally, the MSPPT can maintain good photochromic properties after experiencing deterioration from alkaline solution, acidic solution, and sweat (pH 2.0 ~ 9.0), benefiting from the tight coating of long-chain silane groups and the strong encapsulation for MoO_3 by self-synthesized polymer network. Besides, this photochromic fabric can keep a clear pattern under sunlight irradiation and has great biocompatibility (cell viability > 100%), showing its potential in daily wear. As an application, writing-erasing of the clearly identifiable patterns and information display and storage *via* QR code are demonstrated to verify the feasibility of the practical applications in photo-patterning and information security encryption. This research provides insight into the design and fabrication of scalable, fast light-responsive, and excellent color retention photochromic wearables, aiming at realizing tremendous advancement in sustainable and smart textiles.

4.2 Results and Discussion

Figure 4.1a shows the fabrication procedure for functionalized cotton fabrics using pad-dyeing technology. Initially, the cotton fabrics were treated with an alkali solution to eliminate oil and impurities as well as expose more functional groups to the cotton fiber surface. Subsequently, a radical polymerization process was conducted to form a self-synthesized polymer network composed of BA, St, and VTMS. In this process, the MoO_3 nanoparticles were immobilized in the self-synthesized polymer network space, and then the self-synthesized polymer network was covalently incorporated into cotton fabric. After being photochromic functionalized, the cotton fabric was padded by a rolling mill to get rid of any extra MSPN solution on the fiber surface, thus obtaining MSPN-coated fabric. Finally, MSPPTs were achieved through the modification of MSPN-coated textiles using HDTMS. The materials and fabrication procedures are detailed in the experimental section. The images of the MSPPTs in different deformations (i.e., initial, folding, bending, and rolling) are displayed in Figure 1(b_1-b_4), revealing the MSPPTs possess good flexibility and can be easily integrated into wearables for practical application. Figure 4.1(c_1-c_4) displays the surface morphology of the pristine cotton fabric and MSPPTs. The pristine cotton fabric exhibits a smooth and curly surface (Figure 4.1c_1-c_2). In contrast, the photochromic cotton fabric displays a coarse and relatively uneven surface similar to polymer wrinkle (Figure 4.1c_3-c_4) [173], mainly due to the incorporation of MSPN onto the cotton fiber surface. The volume shrinkage can enhance the robust bonding between fiber and MSPN, enabling the fiber to resist deterioration from washing and daily friction.

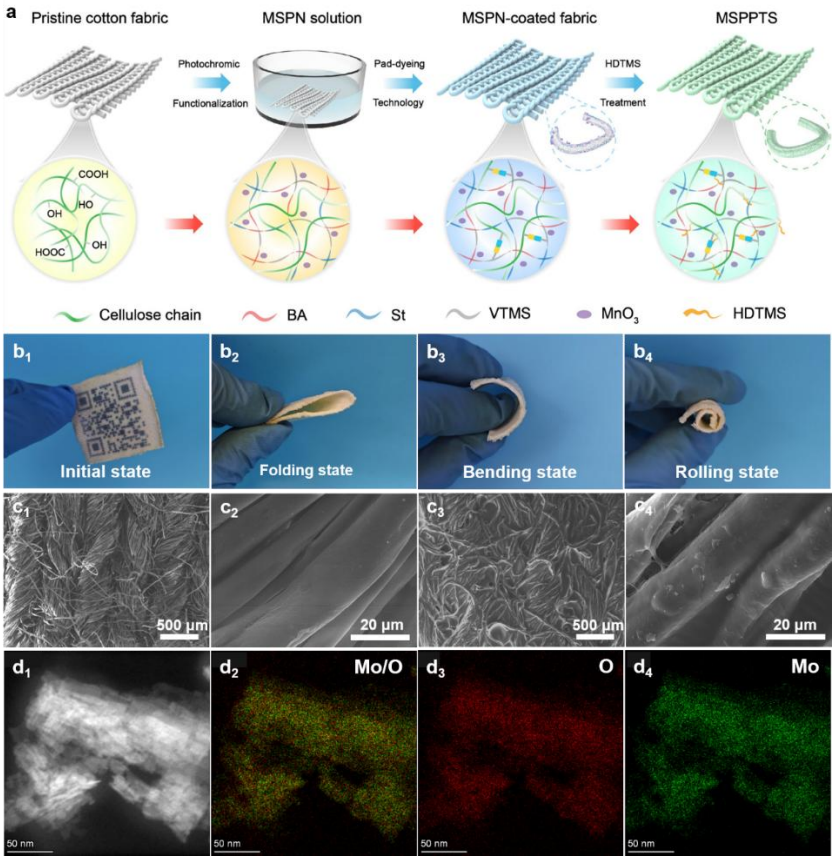

Figure 4.1 The fabrication of MSPPT and characterization of MoO_3 nanoparticles. a) Schematic diagram of procedure for preparing MSPPTs. b_1-b_4) Images of the MSPPTs under different deformations (initial, folding, bending, and rolling). c_1-c_2) Surface morphology of the pristine cotton fabric. c_3-c_4) Surface morphology of the MSPPTs. d_1-d_4) High-resolution image and the element distribution of the prepared MoO_3 nanoparticles.

Figure 4.2 provides a more detailed visualization through SEM images at varying magnifications to substantiate the aforementioned findings. The morphology and element distribution of the high-resolution images of the prepared MoO_3 nanoparticles were investigated using TEM technology. Figure 4.1d_1 displays the high-resolution image of the MoO_3 nanoparticles with a nanoflake structure. EDS elemental analysis

(Figure 4.1d_2-d_4) shows the homogeneous distribution of different elements (O and Mo), confirming the successful preparation of the MoO_3 nanoparticles. In this section, the characterization and evaluation results of previously prepared MoO_3 nanoparticles and WPTs are presented and discussed.

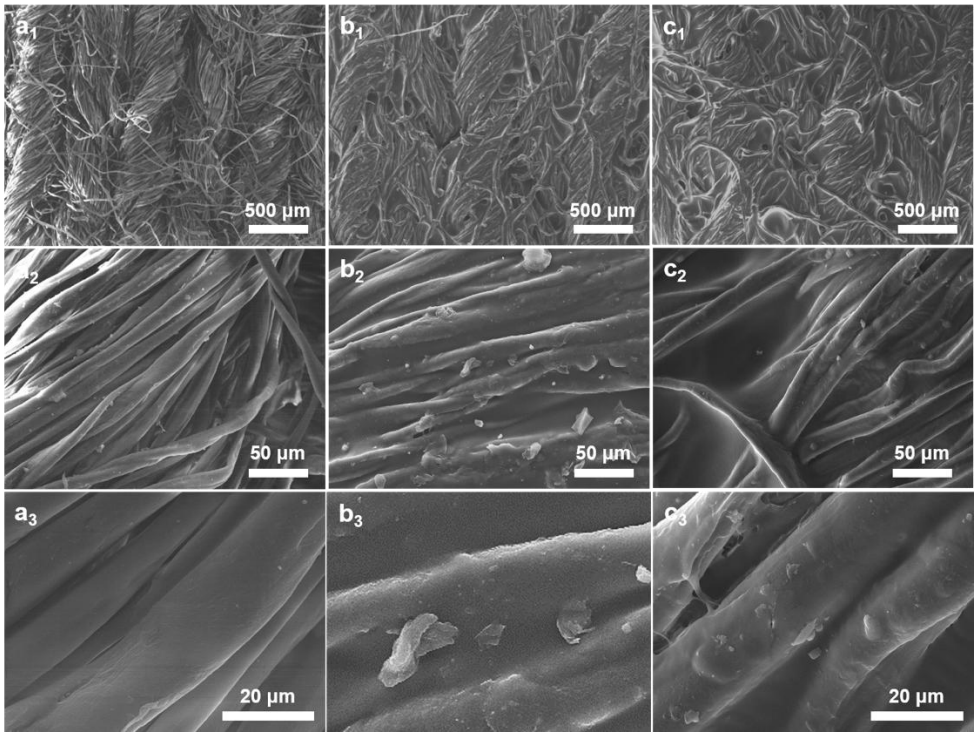

Figure 4.2 SEM images of a_1-a_3) the pristine cotton fabric, b_1-b_3) MSPN-coated fabric, and c_1-c_3) MSPPT at varying magnifications.

In this study, three kinds of MoO_3 nanoparticles were synthesized from $(NH_4)_2MoO_4$, $(NH_4)_6Mo_7O_{24}$, Na_2MoO_4, as detailed experimental section. In this research study, these nanoparticles are defined as MA, MB, and MC, respectively. The MoO_3 nanoparticles from different molybdenum sources were applied to the fabric *via* the coating method to evaluate their photochromic properties. As shown in Figure 4.3, clearly identifiable patterns could be printed on the cotton fabrics using a UV lamp, indicating the MoO_3 nanoparticles from MA, MB, and MC have good photochromic performance.

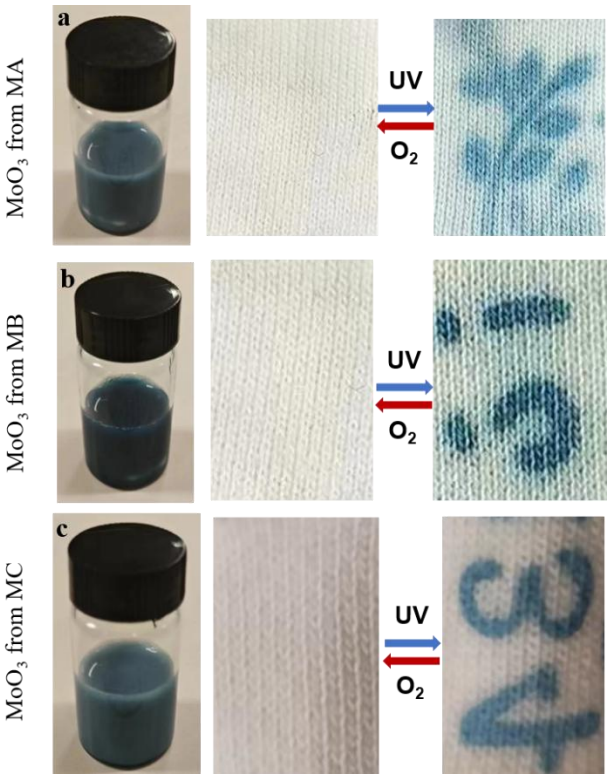

Figure 4.3 a) Photos of MoO_3 nanoparticles solution from MA, photochromic cotton fabric before and after UV irradiation. b) Photos of MoO_3 nanoparticles solution from MB, photochromic cotton fabric before and after UV irradiation. c) Photos of MoO_3 nanoparticles solution from MC, photochromic cotton fabric before and after UV irradiation.

To further verify the photochromic performance of the MoO_3 nanoparticles from MA, MB, and MC, the UV-vis absorption spectrum was measured. Among the three samples, the cotton fabric coated with MC-sourced MoO_3 nanoparticles achieves the highest saturated UV absorbance (>1.2 at 750 nm). The corresponding values for MA and MB are approximately 0.85 and 1.1, respectively (Figure 4.4). This indicates that the MoO_3 nanoparticles from MC possess a more pronounced color change under UV irradiation.

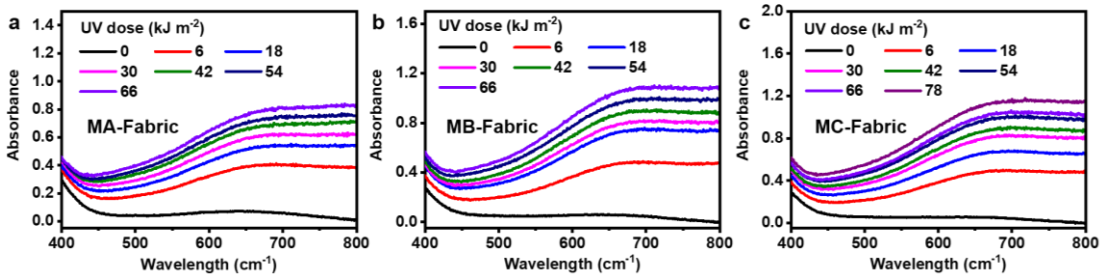

Figure 4.4 a) UV-vis absorption spectrum of cotton fabrics coated with the MoO_3 nanoparticles from MA. b) UV-vis absorption spectrum of cotton fabrics coated with the MoO_3 nanoparticles from MB. c) UV-vis absorption spectrum of cotton fabrics coated with the MoO_3 nanoparticles from MC.

The air permeability of cotton fabrics before and after functionalization was also measured and evaluated. The pristine cotton fabric shows exceptional air permeability, with a value of about 146 mm s^{-1}. After treatment with MSPN and a hydrophobic agent, the air permeability remains at a high level of around 105 and 98 mm s^{-1}, respectively (Figure 4.5). This is attributed to the MSPN coating covering some holes in the fabric where the fibers are interwoven.

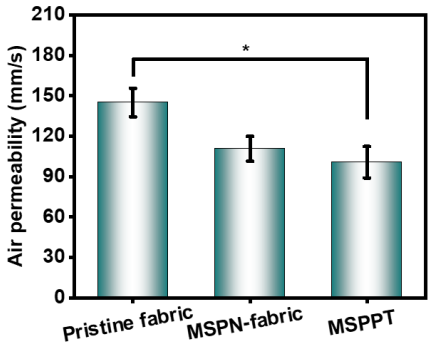

Figure 4.5 Air permeability of cotton fabrics before and after treatment.

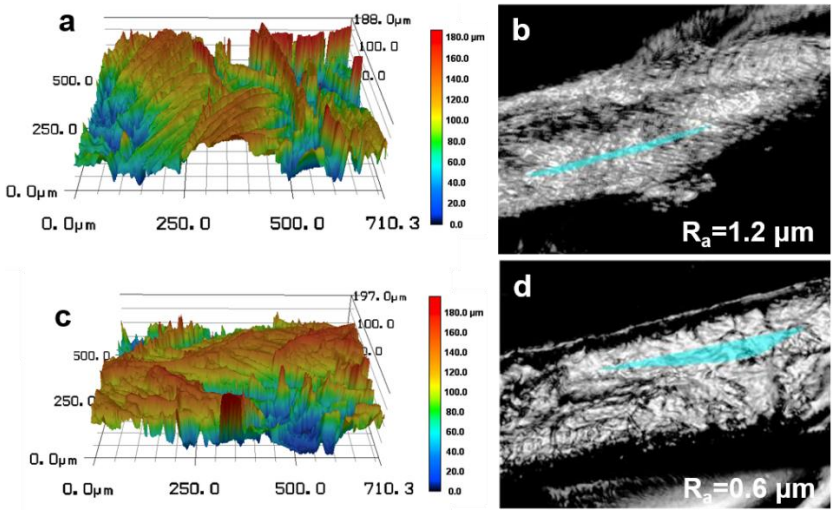

Figure 4.6 (a) Surface roughness of pristine cotton fabric. (b) High-resolution image showing the roughness of pristine cotton fabric. (c) Surface roughness of the MSPPT. (d) High-resolution image showing the roughness of the MSPPT.

The MSPPTs have a lower roughness (0.6 μm) than the roughness of pristine cotton fabric (1.2 μm) because of the MSPN coating. As shown in Figure 4.7, MSPPTs also showed good antifouling performance. Dusts such as sepiolite powder (0.5 g) and coffee (2 mL) were placed on the photochromic fabric for 30 and 2 min, respectively. The dust on the fabric can be easily washed away by water owing to the excellent hydrophobic property of the fabric. Especially, these dusts can still be easily washed away by water even if MSPPTs has been washed for 5 times, proving the antifouling performance of the MSPPTs.

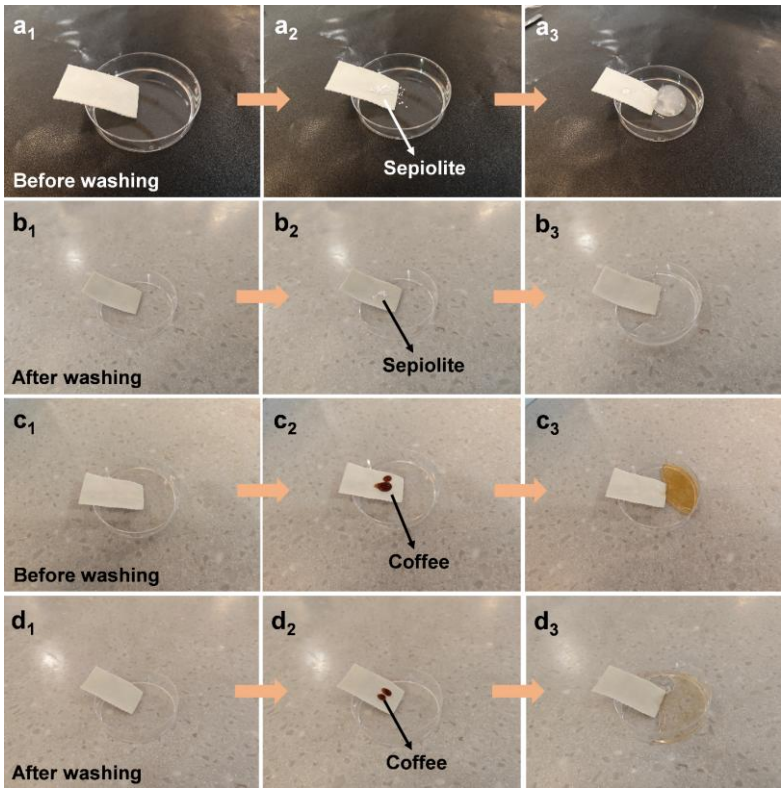

Figure 4.7 Photographs showing antifouling property of the MSPPTs using different stains such as (a, b) sepiolite and (c, d) coffee before and after washing.

As illustrated in Figure 4.8a, the absorbance intensity of fabrics with MoO_3 nanoparticles shows a slight decrease in 4 days. The absorbance values for cotton fabrics coated from MA, MB, and MC decrease from about 0.83, 1.15, and 1.27 to 0.65, 1.01, and 1.14, respectively, showing that the MoO_3 nanoparticles from MC have a longer retention time. Therefore, MoO_3 nanoparticles prepared from MC will be employed for subsequent research experiments.

The size distribution of the synthesized MoO_3 nanoparticles is depicted in Figure 4.8b, revealing a predominant size range between 60 and 250 nm. The diminutive dimensions of MoO_3 nanoparticles facilitate their adhesion to the cotton fiber surface. According to the standard powder diffraction documents JCPDS 21-0569 and JCPDS 35-0609, Figure 4.8c shows that the diffraction peak corresponds to the

product comprising of both the hexagonal phase of MoO_3 (h-MoO_3) and the orthorhombic phase of MoO_3 (α-MoO_3). The absence of characteristic peaks for impurities indicates the high purity of the MoO_3 nanoparticles. The band gap energy is recognized as a pivotal factor in determining the photochromic performances of the MoO_3 nanoparticles. Compared with pure h-MoO_3 or α-MoO_3, the hexagonal and orthorhombic phases of MoO_3 show narrower band gaps and lower band gap energy. This characteristic is advantageous for the separation of e^- and h^+, providing an enhanced diffusion path for the photoinduced proton, thereby leading to a better photochromic effect of MoO_3[174, 175]. Figures 4.8d_1 and d_2 exhibit the TEM images of the prepared MoO_3 nanoparticles, which predominantly manifest as secondary nanoflakes. The hydrothermal formation of the MoO_3 nanoparticles involves two principal stages: (1) nucleation and growth of the primary MoO_3 nanoflakes and (2) oriented aggregation of the primary nanoflakes to form secondary nanoflakes[176]. The formation of the nanoflake particles exhibits a length of around 100 nm, a width of about 15 nm, and an aspect ratio of 6.67. The high-resolution TEM images in Figure 4.8e demonstrate the lattice spacing of 0.210 nm, corresponding to the (2 0 0) crystal plane of MoO_3 nanoparticles. According to the results of SAED patterns (Figure 4.8f), the samples are well-crystallized, consistent with the XRD analysis.

The influence of pad-dyeing cycles on the MSPPTs' photochromic performance and flexibility was also examined, as depicted in Figure 4.8g. When the concentration of the MoO_3 nanoparticles is 5 mg mL^{-1}, the absorbance value of modified cotton fabric rises significantly from about 0.82 to 1.45 as the pad-dyeing times increase from 1 to 3. However, the absorbance remains stable at around 1.45 when the pad-dyeing cycles increase from 3 to 4. Following three pad-dyeing cycles, the flexibility of photochromic fabric greatly rises from around 40 to 69 mm. Additionally, increasing the number of

pad-dyeing cycles from 3 to 4 significantly increases flexibility to around 81 mm. To achieve a balanced property of the photochromic performance and flexibility of the functionalized fabric, the MSPPT treated with 3 cycles was selected for the subsequent investigation. Figure 4.8h demonstrates that the photochromic performance of the MSPPT improves as the concentration of the MoO_3 nanoparticles increases. The obtained photochromic fabric exhibits an absorbance of approximately 0.7 at a concentration of 1.5 mg mL^{-1}. The absorbance reaches around 1.43 when the concentration reaches 5 mg mL^{-1}. Subsequently, the absorbance rises slowly to approximately 1.49 with a concentration of 7 mg mL^{-1} and then only reaches around 1.51 at a concentration of 10 mg mL^{-1}. Considering the complexity and efficiency of the process, the MSPPT treated with a concentration of 5 mg mL^{-1} was chosen for further study.

The mechanical properties, including breaking strength and strain, as depicted in Figure 4.8i, demonstrate that the MSPN coating improves breaking strength, decreases elongation, and increases modulus. The untreated cotton fabric has a breaking strength of around 63 N, slightly decreasing to approximately 60 N after treatment with an alkali solution. Following the application of the MSPN coating, that valve increases to about 103 N. The MSPN coating with high mechanical strength can promote a stronger bond between fibers. In addition, the robust covalent connection between the negatively charged species in the MSPN and the positively charged functional groups in the cotton fiber significantly augments the fabric's tensile strength. The breaking strength of MSPPT experiences a little fall to approximately 100 N, suggesting that the inclusion of a hydrophobic chemical does not result in any harm to the cotton fabric. The initial tensile strain of the untreated cotton fabric and the fabric treated with alkali is roughly 135.6% and 156.6%, respectively. However, after applying the MSPN coating and

treating it with a hydrophobic agent, the tensile strain drops significantly to around 43% and 46.4%, respectively. Figure 4.8j illustrates the alterations in the surface hydrophilicity of these textiles as the dipping times vary. The contact angle of the original cotton fabric decreased rapidly from about 12° (at a dipping time of 0 s) to 0° after 10 s. This decrease can be attributed to the presence of hydrophilic functional groups, such as hydroxyl and carboxyl groups, on the surface of the cotton fibers. In contrast, the MSPN-coated fabric shows higher contact angles, reaching approximately 110° (at a dipping time of 0 s) and 71° (with dipping time is 10 s), respectively. Following the HDTMS treatment, the MSPPT exhibits a significant increase in contact angles, reaching approximately 135°. Furthermore, the high contact angles of 130° are maintained for 10 s due to the removal of oxygen-related functional groups. A high contact angle can decrease the infiltration of H_2O_2 solution into the fabric, thereby minimizing the detrimental effects of the oxidant on the photochromic characteristics of MoO_3 nanoparticles. This also ensures that the patterns on the MSPPT can be easily erased when exposed to H_2O_2 solution. In addition, the change of surface macrostructure before and after functionalization can also be observed through the change of fiber surface roughness (Figure 4.6).

Figure 4.8k shows the FT-IR spectrum of the cotton fabrics before and after functionalization. There are characteristic peaks at approximately 1,082 cm^{-1}, 1,649 cm^{-1}, and 2,858 cm^{-1}, corresponding to the asymmetric stretching vibration of Si-O-Si, C=C stretching, and asymmetrical C-H stretching, respectively. After applying the MSPN coating, the peaks at 1,649 cm^{-1} and 2,858 cm^{-1} decrease in intensity, while a new peak at 1,082 cm^{-1} appears[177], indicating a successful combination between MSPN coating and fiber surface. Additionally, the MSPPT shows a peak at approximately 2,858 cm^{-1}, which signifies the presence of CH_3 and CH_2 bonds,

attributed to the long-chain alkyl hydrophobic fabric surface induced by HDTMS treatment[178]. The functionalization process significantly alters the surface elemental composition. The pristine cotton fabric has 57.45% carbon, 2.34% nitrogen, 40.18% oxygen, 0.01% silicon, and 0.01% molybdenum in terms of atomic percentages. The modification of MSPN alters the values to 67.29%, 3.13%, 29.22%, 0.25%, and 0.11% (Figure 4.8l), confirming the successful coating of MSPN on the cotton fiber surface. After undergoing HDTMS treatment, the Si content increases to 0.43%, but Mo content remains stable, indicating successful hydrophobicization of the MSPN-fabric.

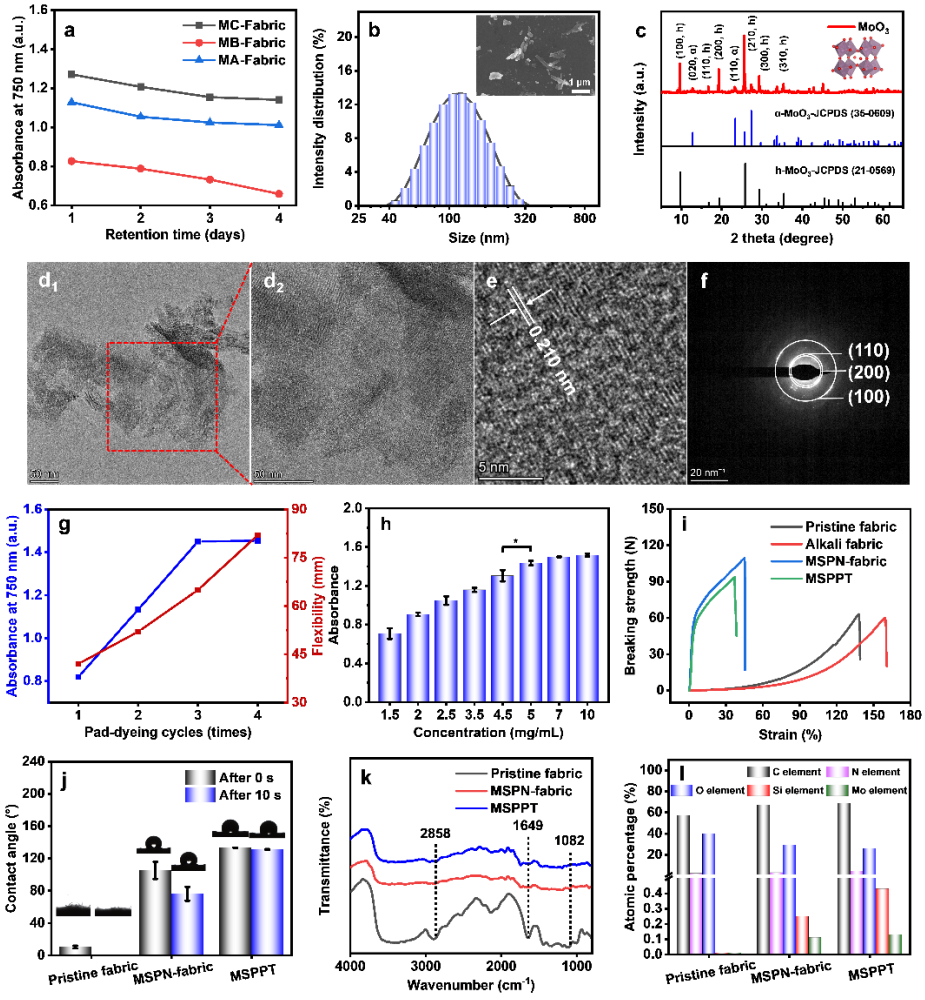

Figure 4.8 Characterization of the MoO_3 nanoparticles and fabrics. a) UV-vis

absorption spectrum of cotton fabrics coated with the MoO_3 nanoparticles from MA, MB, and MC. b) The size distribution of the prepared MoO_3 nanoparticles. c) XRD patterns of the prepared MoO_3 nanoparticles. d_1-d_2) TEM images of the prepared MoO_3 nanoparticles. e) The high-resolution TEM image of the MoO_3 nanoparticles. f) SAED patterns of the synthesized MoO_3 nanoparticles. g) The absorbance changes and flexibility of the MSPPT with increasing pad-dyeing cycles. h) The absorbance changes of the MSPPT with increasing concentration of MoO_3 nanoparticles. i) The tensile strain of the pristine fabric, alkali treated fabric, MSPN-coated fabric, and MSPPT. j) Variations in contact angle of samples with time increases. k) FT-IR spectra of the original cotton fabric, MSPN-coated fabric, and MSPPT. l) Element content of the cotton fabrics before and after modification.

Figure 4.9 depicts the fabrics' thermal stability before and after treatment. These fabrics exhibit weight loss when the temperature rises. Between a temperature range of 20 and 800°C, there is an approximate weight loss of 90%. Moisture evaporation causes a slight decrease in value at temperatures below 100°C. At around 400°C, cellulose in the cotton fiber begins to decompose, resulting in a substantial weight reduction. Compared with the pristine cotton fabric, the MSPPT shows a weight loss at about 420°C due to the decomposition of polymer chains in the MSPN. In addition, the MSPPT shows less weight loss owing to the excellent thermal stability of the MoO_3 nanoparticles.

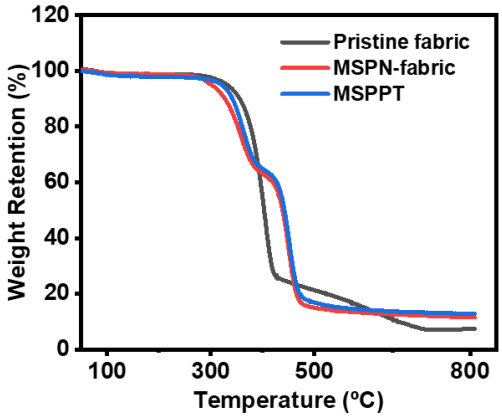

Figure 4.9 Thermal stability of the cotton fabrics before and after treatment.

The SEM image in Figure 4.10 shows the polymer network's tight encapsulation of MoO_3 nanoparticles.

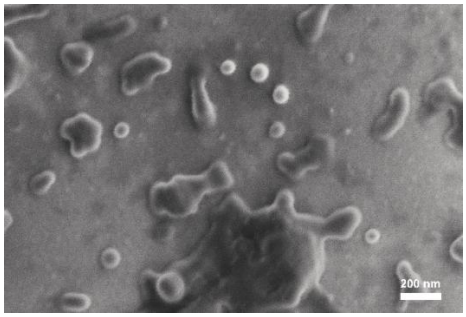

Figure 4.10 SEM image of the MSPN.

Additionally, the prepared MSPN has outstanding dispersibility in water and remains stable when stored at ambient temperature, as the sodium lauryl sulfate (SDS) absorbs onto the MSPN surface, resulting in a high zeta potential (-58.7 mV) that prevents aggregation (Figure 4.11).

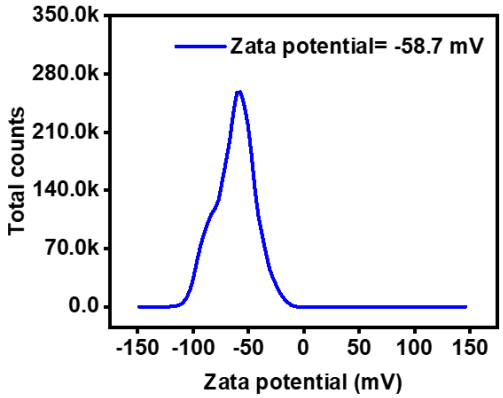

Figure 4.11 Zeta potential of MSPN solution.

Moreover, an abrasion-resistance test in Figure 4.12 reveals that the MSPPTs are highly durable against abrasion after washing for 5 times. After abrasion for 10,000 cycles, the MSPPTs didn't have apparent rupture and still displayed great photochromic property, which can be attributed to the tight combination between MoO_3 nanoparticles and fabric.

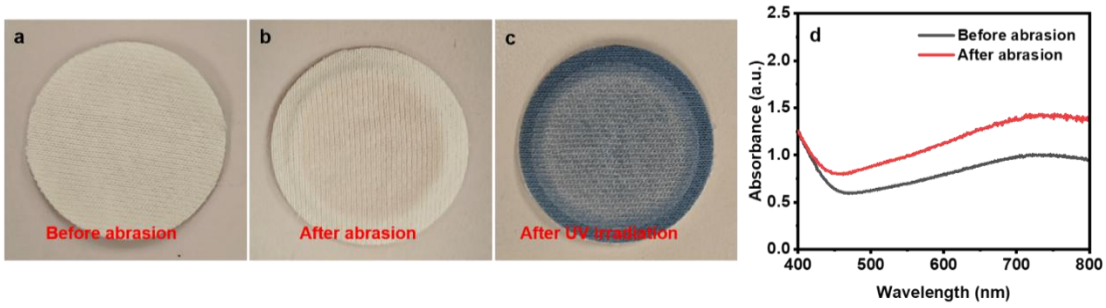

Figure 4.12 Photographs of MSPPTs a) before abrasion and b) after abrasion. c) Photographs of abrased MSPPTs after UV irradiation with UV dose of 60 kJ m^{-2}. d) UV-vis absorbance spectra of MSPPTs before and after abrasion.

The fabrication procedure and bonding mechanism of MSPN were further evaluated. Interparticle cross-linking between St and BA can be facilitated by the cross-linker VTMS (Figure 4.13a). During the radical polymerization process, the $Si(OCH_3)_3$ groups in VTMS undergo hydrolysis to produce Si-OH groups[179]. The cotton fabric,

composed of cellulose, is rich in positively charged functional groups like carboxyl, while the polymer has a significant number of negatively charged groups, such as silanol groups. Strong covalent bonding between Si-OH and carboxyl group (Figure 4.13b) ensures the stability and fastness of the polymer coating on the cotton fabric surface. Figure 4.13c depicts the schematic design illustrating the integration of MSPN with cotton fabric. The MoO_3 nanoparticle, with its photochromic properties, functions as a monomer and engages in copolymerization, imparting photochromic characteristics to the polymer network. Smaller MoO_3 nanoparticle size can lead to larger surface areas of MSPN, hence enhancing its photochromic properties. Simultaneously, the polymer network acts as a protective barrier for the MoO_3 nanoparticles. This barrier enables smooth color switching using common household disinfectant (H_2O_2 solution) and prevents degradation caused by the alkaline chemicals in laundry detergents.

Furthermore, the MSPPTs exhibit remarkable stability in complicated-varying microenvironments between photochromic fabrics and human skin, including various PH, temperature, and humidity caused by daily wear, washing, and human movements. The MSPPTs were immersed in acid, artificial sweat, and alkali solution with pH of 2, 6.5, and 9 for 12 h to assess their stability in different pH environments. As shown in Figure 4.13d, the UV absorbance of MSPPTs treated with the acid and artificial sweat solution remains stable, and the UV absorbance of MSPPT treated with alkali solution shows a relative decrease. This suggests that MSPPT is very stable in a range of pH environments. The MoO_3 nanoparticle, an acidic oxide, can generate molybdate and lose its photochromic properties in an alkali solution with a pH greater than 8. It is clear that MSPPTs can handle chemical reactions from alkaline solutions when compared to cotton fabric directly coated with MoO_3 nanoparticles. This resistance is critical for

daily soaking and washing laundry with detergent. This demonstrates that the strong encapsulation for MoO_3 by a self-synthesized polymer network and the tight coating of long-chain silane groups enable the MSPPTs to maintain their outstanding photochromic performance in an alkaline environment. Figure 4.13e reveals the MSPPTs have excellent stability in the face of temperature fluctuations ranging from -30 to 60°C. In a wide living temperature range (0-40°C), even at 60°C, the MSPPTs maintain excellent photochromic performance with UV absorbance reaching approximately 1.45. The MoO_3 nanoparticles with excellent thermal stability allow MSPPTs to maintain great photochromic properties at changing temperatures. The UV absorbance of MSPPTs in Figure 4.13f shows a gradual decline from about 1.5 to 1 when exposed to a relative humidity of approximately 90% for 10 days. High humidity does not significantly affect the photochromic textiles, indicating their versatility in various conditions. This can be attributed to the condensation reaction between HDTMS and hydroxyl groups in the MSPN-coated fabric, endowing it with high hydrophobicity and minimal water adsorption. Meanwhile, HDTMS can reduce the surface tension of the fabric by modifying the rough surface[180], resulting in improved hydrophobicity. These findings confirm that the MSPPTs retain stable photochromic responses under diverse and harsh environmental conditions—including broad pH variations, extreme temperatures, and high humidity—enabled by the protection of the polymer network and hydrophobic surface modification.

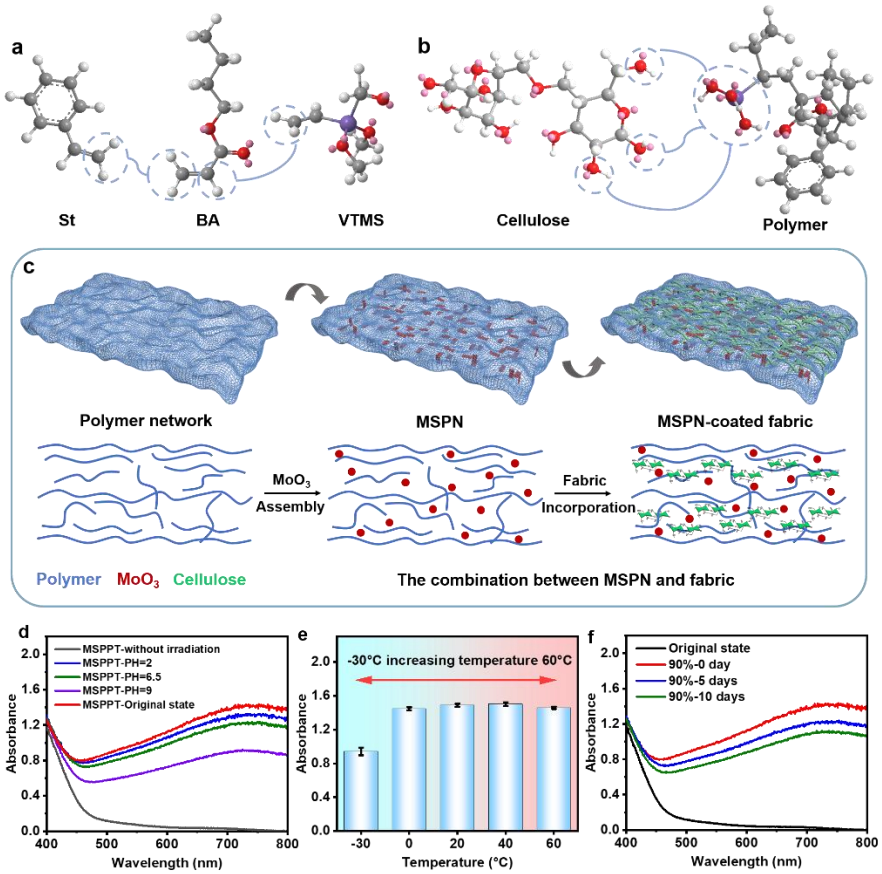

Figure 4.13 Illustration of combination mechanism for preparing photochromic fabrics and stability of the MSPPTs. a) Schematic of combination mechanism between St, BA and VTMS. b) Illustration of mechanism combining cellulose and polymer. c) Schematic diagram of combination between MSPN and cotton fabric. d) The absorbance of MSPPTs in the different PH environments. e) The absorbance change of MSPPTs in the different temperatures (from -30 to 60°C). f) The absorbance change of MSPPTs with the humidity of 90 in 10 days.

When the MSPPTs are exposed to UV radiation with a wavelength of 365 nm, their color changes significantly from pale yellow to blue. Figure 4.14 indicates the alterations in the electronic configuration of the constituent materials throughout the photochromic transformation, thereby clarifying the underlying photochromic

mechanism of the MSPPTs.

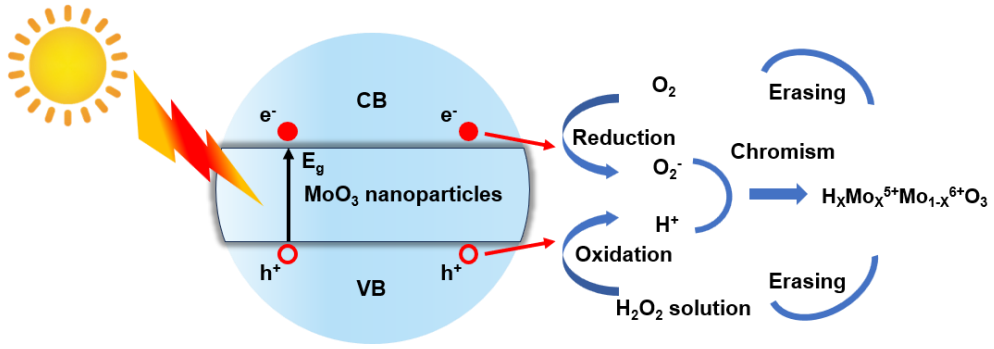

Figure 4.14 The variation of electronic structure of the components during the photochromic process, clarifying the photochromic mechanism of the MoO_3 nanoparticles.

When the MoO_3 nanoparticle is exposed to UV light, photons with energy exceeding the bandgap (hv > Eg) elevate electrons from the valence band to the conduction band while creating an equivalent number of holes in the valence band. The excitation leads to the creation of electron-hole pairs, as depicted in Equation 1. The MSPPTs, inherently retaining moisture either on their surface or within their structure, generate the required protons for the photochromic response through the interaction of the adsorbed water with holes, as shown in Equation 2. Subsequently, these protons are combined with the MoO_3 nanoparticle, resulting in the formation of $H_xMo_x^{V}Mo_{1-x}^{VI}O_3$ (as shown in Equation 3). Concurrently, the Mo^{6+} captures one electron from its vicinity, transitioning to Mo^{5+} (Equation 4). The intervalence charge transfer between the newly formed Mo^{5+} (valence band) and the adjacent Mo^{6+} (conduction band) prompts the MoO_3 nanoparticles to adopt a blue coloration (Equation 5) [164]. Upon reintroduction to an oxygen-rich environment (H_2O_2 solution), the Mo^{5+} is reoxidized to Mo^{6+}, causing the MoO_3 nanoparticles to revert to their original pale-yellow state.

$$MoO_3+hv \rightarrow MoO_{3*}+e^-+h^+ \qquad (1)$$

$$2h^{+}+H_2O \rightarrow 2H^{+}+O \quad (2)$$

$$MoO_3+xe^{-}+xH^{+} \rightarrow H_xMo_x^{V}Mo_{1-x}^{IV}O_3 \quad (3)$$

$$Mo^{6+}+e^{-} \rightarrow Mo^{5+} \quad (4)$$

$$hv+Mo_A^{5+}+Mo_8^{6+} \rightarrow Mo_A^{6+}+Mo_8^{5+} \quad (5)$$

Photochromic wearables with a long retention period can rapidly change from a colored state to a colorless state, making them suitable for easy everyday wear and photo-patterning applications. An essential aspect of sustainable and personal everyday wear is the use of a secure and convenient fading technique.

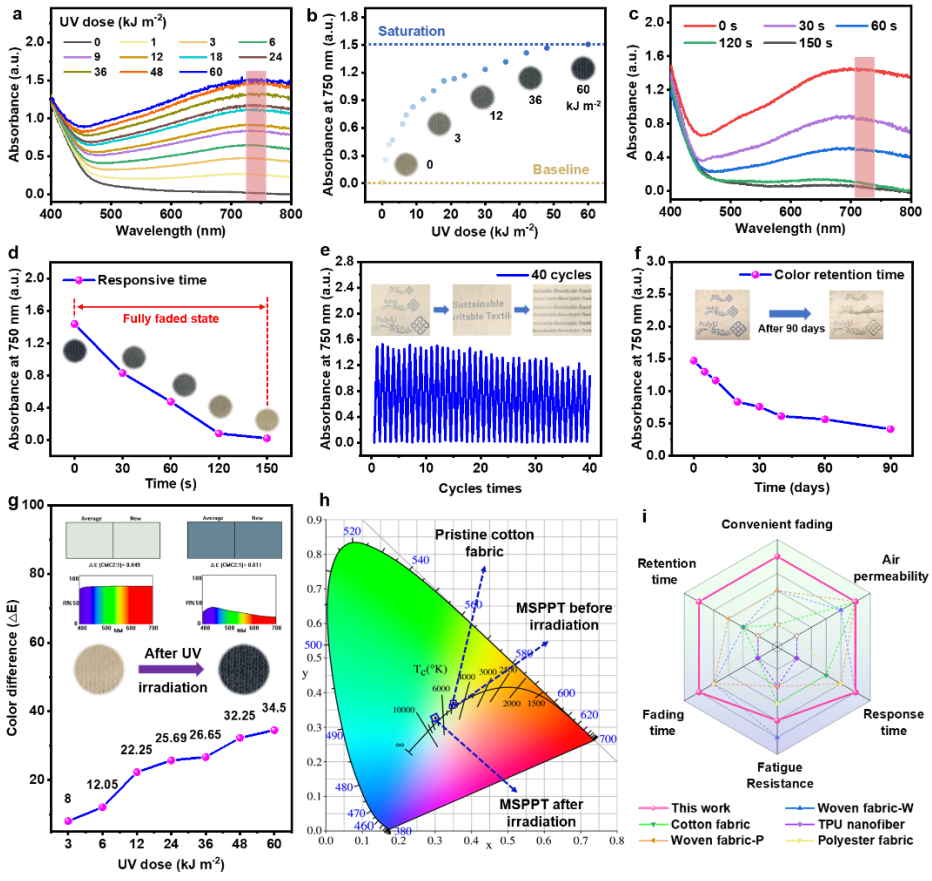

Figure 4.15 Photochromic performances of the MSPPTs. a) UV-vis absorbance spectra of the MSPPTs with increasing exposure to UV light (λ= 365 nm). b) Absorbance at 750 nm as a function of UV dose for the MSPPTs. c) UV-vis absorbance spectra of the MSPPTs in the process of color-fading with increasing time. d) Absorbance at 750 nm

as a function of fading time for the MSPPTs. e) Absorption intensity represents the fatigue resistance of the MSPPTs switching color from pale yellow to blue. f) The change in UV-vis absorbance at 750nm indicates the retention time of the MSPPTs in 90 days. g) Color difference (ΔE) of the MSPPTs with increasing UV dose as well as the recorded coloration process of the photochromic fabrics *via* Macbeth Color-Eye 7000A under CIE standard illuminant D65 and 10° standard chromaticity. h) CIE coordinate diagrams of pristine cotton fabric and the MSPPTs before and after UV irradiation in the (x, y) chromaticity diagram. i) Comparison of the performances between various photochromic wearables.

Unlike other photochromic fabrics that require the use of hazardous and hard-to-find chemicals, the MSPPTs can realize a rapid fading cycle (in 150 s) using household disinfectant (2% H_2O_2 solution) at 50°C. H_2O_2 solution, a popular household disinfection water, is an environmentally friendly oxidant widely used in paper bleaching, wastewater treatment, oxidant substrate, and wound disinfection[181-183]. The photochromic properties of MSPPTs were evaluated using a UV-vis spectrophotometer. Figure 4.15a shows a wide absorption band at around 750 nm, which can be attributed to the conversion of Mo^{6+} to Mo^{5+}[184]. The absorption intensity of MSPPTs at a wavelength of 750 nm increases as the UV dose increases until it reaches a saturation point at a UV dose of 60 kJ m^{-2}. This is accompanied by a noticeable shift in the color of the MSPPTs from pale yellow to blue following exposure to UV light (Figure 4.15b). Figure 4.16 displays the detailed images depicting the hue alteration in the MSPPTs as the duration of UV irradiation increases. Next, the MSPPTs were sprayed with 2% H_2O_2 solution and placed in an oven set at a temperature of 50°C. The absorbance peak experiences a substantial decline as the treatment time increases, eventually reaching a plateau at 150 s (Figure 4.15c). Meanwhile, the MSPPTs returned

to their original pale-yellow state following treatment with a 2% H_2O_2 solution. The value decreases from approximately 1.5 to 0, reaching its minimal level (Figure 4.15d).

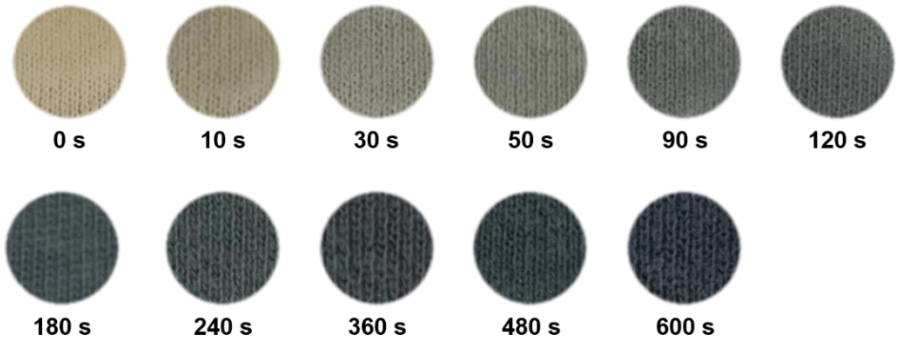

Figure 4.16 Images of color change in the MSPPT with the increase in UV irradiation time.

When producing wearable photochromic fabrics, evaluating their fatigue resistance and how long they can retain their color is important[156]. Figure 4.15e illustrates the fatigue resistance of the photochromic cotton fabrics by measuring the absorbance levels in both colored and bleached states. The absorption intensity of MSPPTs at a wavelength of 750 nm shows a modest decline from approximately 1.5 to 1 after 40 cycles. This indicates that MSPPTs have excellent fatigue resistance and hold significant promise in the realm of sustainable photo-patterning information records and customizable textiles. In Figure 4.15f, the absorbance of MSPPTs decreases from around 1.5 to 0.41 in 90 days, revealing that MSPPTs possess excellent color retention. The MSPPT exhibits the most prolonged color retention compared to all other reported photochromic textiles. Moreover, after undergoing 20 cycles of washing, the absorbance of photochromic fabrics consistently and moderately decreases from approximately 1.03 to 0.46 in 60 days (Figure 4.17). This shows that the MSPPTs can still exhibit outstanding photochromic characteristics after repeated washing. The high fatigue resistance, stability, and color retention time suggest that the MSPPTs have

considerable practical application potential in sustainable, long-term, efficient, and stable photo-patterning fabrics, even in harsh situations such as washing.

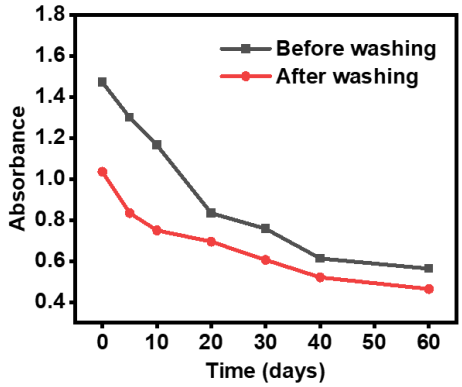

Figure 4.17 Absorbance of MSPPTs before and after washing.

The color difference (ΔE) and chromaticity are further measured to illustrate the reversible photochromic properties of MSPPTs. Color difference in Figure 4.15g exhibits the MSPPTs experience an obvious color change during the photochromic process. When the UV dose reaches 6 kJ m^{-2}, the ΔE is 12.05 (ΔE > 12). The ΔE then rises to 34.5 when the UV dose is increased to 60 kJ m^{-2}. In addition, increased UV dosage causes a steady decline in the reflectance of the MSPPTs. Figure 4.15h depicts the CIE 1931 chromaticity diagram of the pristine cotton fabric as well as the MSPPTs before and after UV irradiation. The pristine cotton fabrics exhibited a negligible color change in the (x, y) chromaticity diagram relative to the MSPPTs before UV irradiation, indicating that the modification process did not significantly affect the color dimensions. When exposed to 365 nm UV light, the MSPPTs' coordinates are far distant from those before UV irradiation, revealing an apparent color gap. In this work, MoO_3 nanoparticles were employed as photochromic materials to prepare photochromic fabrics for the first time, and polymer network and long chain silyl group were innovatively used to provide encapsulation and protection for MoO_3 nanoparticles.

Table 4.1 Performance comparison of our photochromic fabric with reported

photochromic fabrics

Substrate	Photochromic material	Response time (s)	Fading time	Retention time (days)	Fatigue resistance (cycles)	Air permeability	Fading *via* household disinfectant	Cost	Refs
Cotton fabric	$Na_4W_{10}O_{32}$	< 60	120 min	0.08	> 20	✓	×	Low	[101]
Woven cotton fabric	WO_3	5	5 min	> 7	> 100	✓	×	Low	[161]
Cotton fabric	PMoA	< 60	-	> 10	> 20	✓	×	High	[73]
Woven cotton fabric	ZnO	5	50 s	0.09	> 35	×	×	High	[160]
Woven cotton fabric	PMoA	30	-	> 15	> 10	✓	×	High	[157]
TPU nanofiber	WO_3	300	30 min	0.5	> 6	×	×	High	[185]
Cotton fabric	Spiropyran	10	50 s	0.003	> 20	✓	×	High	[97]
Polyester fabric	Hackmanites	15	50 min	0.03	> 20	-	×	Low	[186]
Knitted cotton fabric	MoO_3	10	2.5 min	> 90	> 40	✓	✓	Low	This work

Table 4.2 Performance evaluation of various photochromic fabrics (grade is divided into 5 grades)

Substrate	Color retention	Fatigue resistance	Convenient fading approach	Air permeability	Response time	Fading time	Refs
Woven cotton fabric-P	3	2	3	5	4	4	[157]
Woven cotton fabric-W	2	5	3	4	5	4	[161]
Cotton fabric	2	3	1	5	3	1	[101]
TPU nanofiber	1	2	1	1	1	1	[185]
Polyester fabric	1	3	1	1	4	4	[186]
Knitted cotton fabric	5	4	5	5	5	5	This work

The MSPPTs show comprehensive and extraordinary photochromic properties,

including the longest color retention time, convenient and safe fading method, good air permeability, excellent fatigue resistance, fast fading time, and short response time (Figure 4.15i, Table 4.1, and Table 4.2).

Color retention refers to the capacity of photochromic fabrics to maintain their coloration state after exposure to UV irradiation. Long color retention time can ensure that photochromic fabrics possess long-term clear photo-patterning in the sustainable application. To enhance the clarity and professionalism of comparing and evaluating the color retention capacity of various photochromic fabrics. The color retention ability is categorized into five grades: the first grade represents a duration of less than 1 day, the second grade represents a duration of 1–10 days, the third grade represents a duration of 11–30 days, the fourth grade represents a duration of 31–60 days, and the fifth grade represents a duration beyond 60 days.

The number of reversible writing-erasing cycles that photochromic fabric can perform is known as fatigue resistance. High fatigue resistance allows photochromic fabrics to maintain vitality and function after repeated use in sustainable photo-patterning and information encryption applications. To enhance the clarity and professionalism of comparing and evaluating the fatigue resistance of various photochromic materials. Five grades categorize the fatigue resistance: the first grade corresponds to 1–5 cycles, the second grade to 6–10 cycles, the third grade to 11–30 cycles, the fourth grade to 31–60 cycles, and the fifth grade to more than 60 cycles.

An indispensable requirement for the commercialization and widespread adoption of photochromic fabrics is the availability of a convenient and secure technique to erase the coloration state of these fabrics. In order to provide a more precise and professional comparison and evaluation of the convenient fading strategy, Convenient fading is categorized into five levels. The first level requires either specialized equipment (such

as an ozone machine or solar simulator) or a fading time that exceeds half of the retention time. In the second level, the fading temperature surpasses 100°C. In the third level, laboratory equipment is required like an oven to raise the temperature to 80-100°C. Additionally, a powerful oxidant such as potassium persulfate, hypochlorous acid, or ozone is employed. In the fourth level, laboratory equipment is required like an oven to raise the temperature to 60-80°C and household disinfectants such as alcohol and hydrogen peroxide are used. Level 5: Utilize household heating appliances such as induction cookers and kettles, maintaining a temperature range of 40-60°C. Additionally, employ household disinfectants such as alcohol and hydrogen peroxide.

Air permeability is defined as a fabrics' ability to allow air to pass through it. High fabrics' air permeability can minimize the accumulation of heat and moisture, reducing the risk of skin irritations and infections. In order to enhance the clarity and professionalism of comparing and evaluating the air permeability of various photochromic materials, Air permeability is categorized into five levels. The first level is less than 5 mm/s, the second level is between 5 and 10 mm s^{-1}, the third level is between 10 and 100 mm s^{-1}, the fourth level is between 50 and 100 mm s^{-1}, and the fifth level is greater than 100 mm s^{-1}.

In practical photo-patterning and information security encryption applications, a fast response time can ensure a stable and smooth transition between the writing and erasing state as well as providing a dynamic and sensitive wearing experience. To enhance the clarity and professionalism of comparing and evaluating the response times of various photochromic materials. The response time is categorized into five grades: the first grade is greater than 300 s, the second grade is 101-300 s, the third grade is 31-100 s, the fourth grade is 11-30 s, and the fifth grade is 1-10 s.

The rapid fading time can ensure a seamless shift of color throughout the photochromic fabric's repeated writing-erasing process. To enhance the clarity and professionalism of comparing and evaluating the fading time of various photochromic fabrics. The fading time is categorized into five grades: the first grade is > 24 h, the second grade is 6-24 h, the third grade is 1-6 h, the fourth grade is 5-60 min, and the fifth grade is < 5 min.

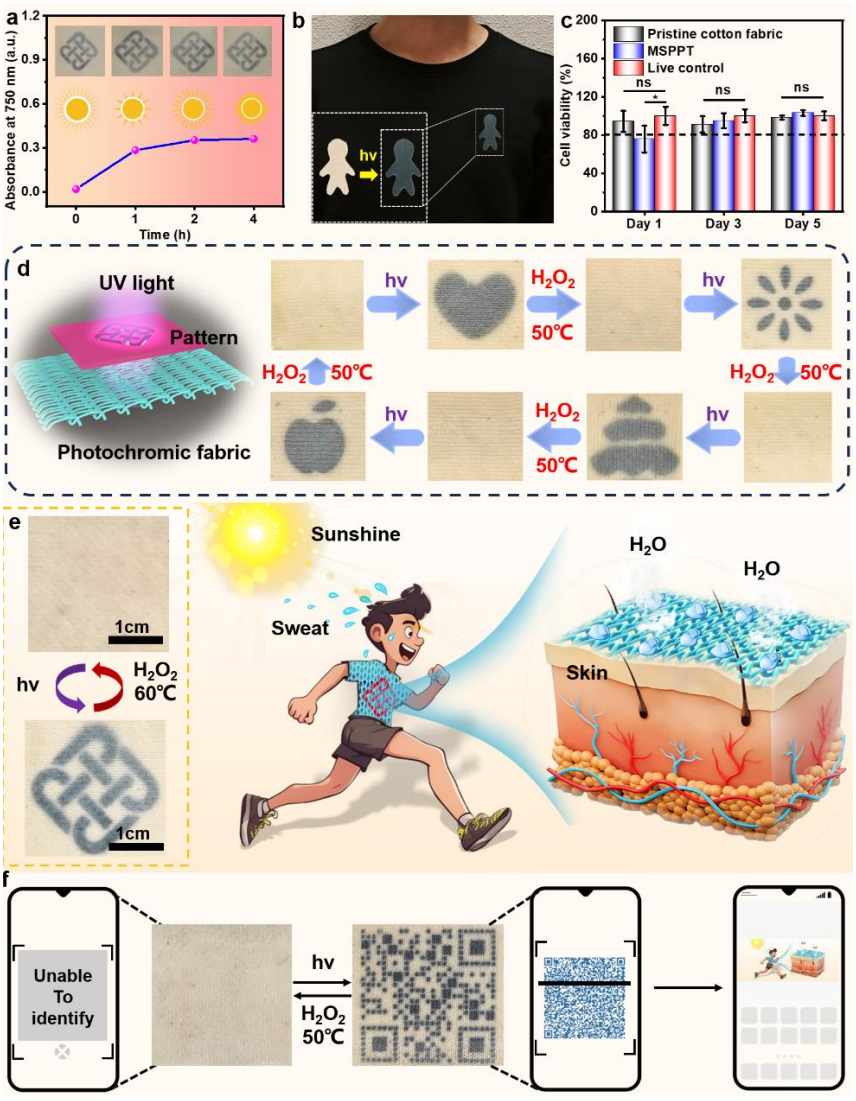

Figure 4.18 Practical application of MSPPTs. a) Photochromic response of MSPPTs under the sunlight. b) Photography of MSPPT connected to the clothing. c) Cell

viability for the pristine cotton fabric, MSPPTs, and control after 1, 3 and 5 days of incubation. d) Patterns are repetitively displayed on the MSPPTs by employing a photomask and UV lamp. e) Schematic design of the system that consists of a photochromic device worn on the skin and its interaction with the environment. f) Utilization of MSPPTs for encryption in information security.

The photochromic fabric's insensitivity to solar irradiation can ensure that the patterns on the cloth remain visible throughout prolonged outdoor wear and sports activities. Figure 4.18a shows that after 4 hours of intense sunlight exposure (a UV index of 7,175 mW m^{-2}), the absorption intensity of the vacant region on the MSPPT surface increases to approximately 0.34. Despite this, the pattern remains visible. It can be understood that the MSPPT can maintain a clear pattern in the presence of sunlight. Figure 4.18b displays an image of the clothes with an MSPPT, illustrating the seamless integration of the MSPPT into the clothing for reversible photochromic applications in everyday wear. In addition, a cytotoxicity test and a skin allergic reaction test were carried out to evaluate the biocompatibility of MSPPTs with human skin. This is crucial for guaranteeing the safety of daily wear, preventing harm to human skin, and promoting sustainable and environmentally friendly development. Figure 4.18c demonstrates that MSPPTs exhibit a cell viability of around 104% (> 100%) after 5 days, which is comparable to the pristine cotton fabric (98%). The detailed optical density (OD) value of the pristine cotton fabric, MSPPTs, and control are shown in Figure 4.19, displaying a progressive increase in OD values over time.

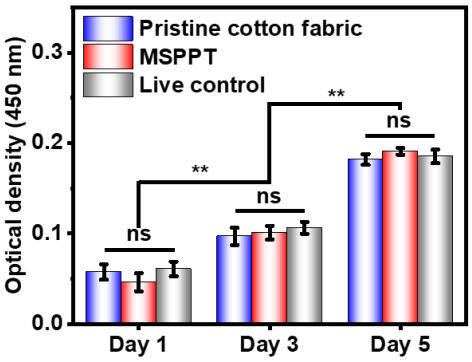

Figure 4.19 Absorption at 450 nm in MTT assay of different incubation groups after 1, 3 and 5 days of incubation.

Additionally, the skin allergic reaction test results also proved that MSPPT has no harm to the skin (Figure 4.20). It can be directly attached to the skin without any additional treatment and is non-irritating to human skin even after 72 h of application. These prove that the polymer-coated MoO_3 nanoparticles can endow cotton fabric with excellent biocompatibility, ensuring daily wear safety and avoiding human skin injury.

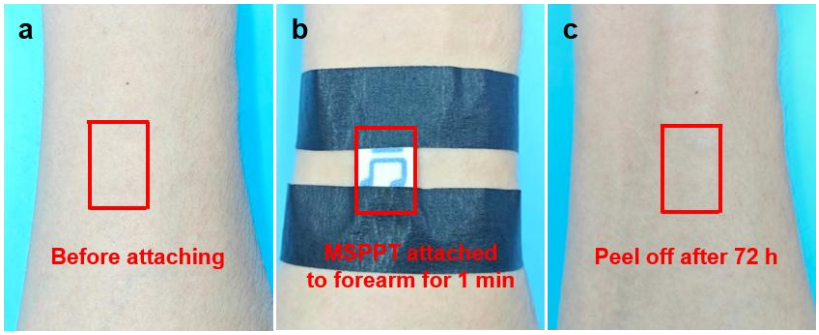

Figure 4.20 Digital images showing the skin irritation results of MSPPTs on the forearm

Sustainable photo-patterning experiments of MSPPTs have been made for rewritable image information. The writing and erasing of the clearly identifiable patterns such as heart, flower, pine, and apple are exhibited on the MSPPTs (Figure 4.18d). These printed patterns can be easily erased by using a 2% concentration of H_2O_2

solution at 50℃ for 150 s, and they can remain visible under environmental conditions for at least 90 days.

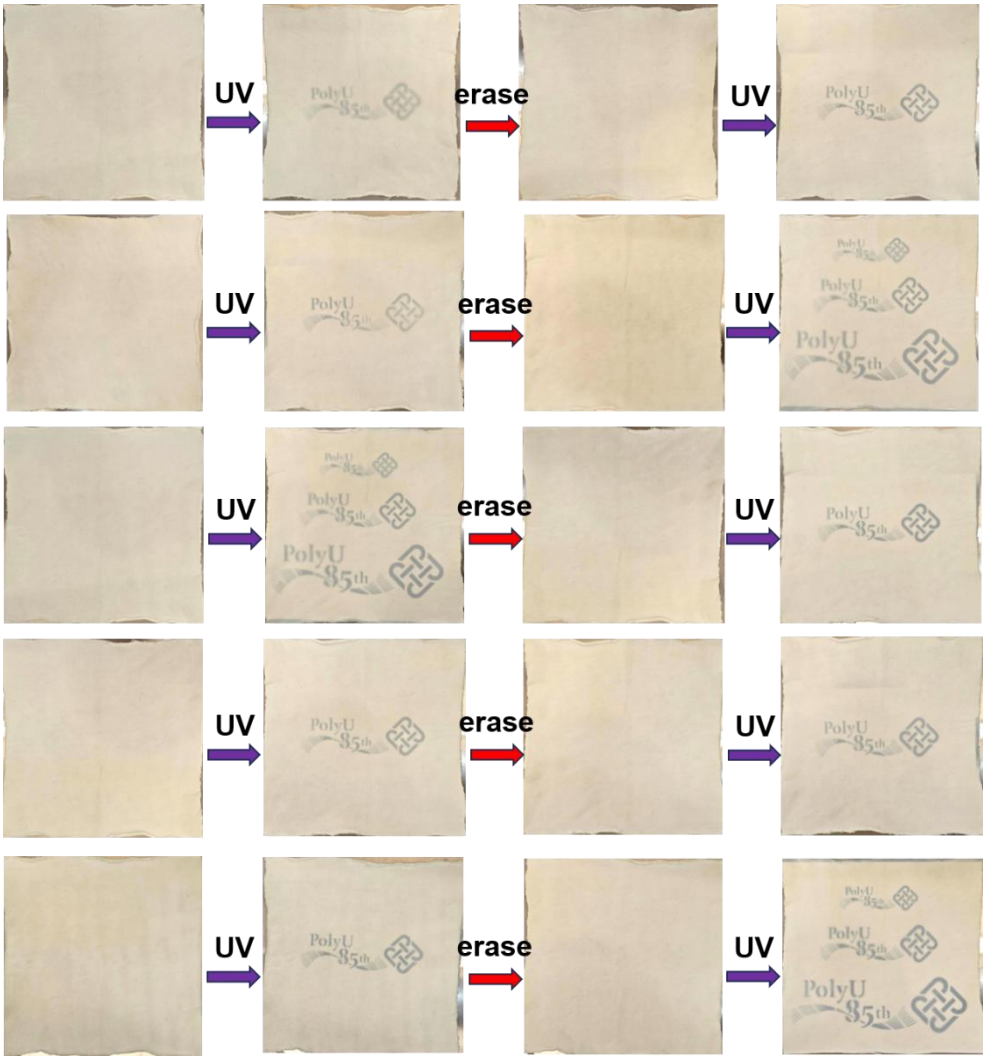

Figure 4.21 The images showing the writing-erasing cycles of MSPPT.

Furthermore, Figure 4.21 displays the writing-erasing cycles of MSPPT (with a size of 400 cm^2) repeated 10 times, showing that MSPPTs can be applied to sustainable photo-patterning. Figure 4.18e presents a schematic design of a photochromic device-environment system that demonstrates the practical application of MSPPTs. The porous structure of MSPPTs allows for the unrestricted release of body metabolites (heat and perspiration) into the air. Besides, for an extended period of time, one can readily

identify the clear patterns on MSPPTs, free from the influence of bodily metabolites like perspiration and heat, and environmental factors like sunshine and humidity. In order to implement MSPPTs' information storage and encryption functionality, the image represented in Figure 4.18e was encoded and stored in a QR code. By using a UV lamp to irradiate the skeletonized QR code mask, a clear QR code was displayed on the surface of MSPPTs with a resolution of about 1 mm (Figure 4.18f). Mobile phones can quickly recognize the QR code and navigate to the web page containing Figure 4.18e. Besides, the QR code on the MSPPTs still can be quickly recognized by mobile phones after indoor lighting irradiation for 90 days (Figure 4.22). These illustrate that MSPPTs can remain stable under long-term indoor lighting irradiation as well as possess significant potential for application in anti-counterfeiting marks and information security encryption.

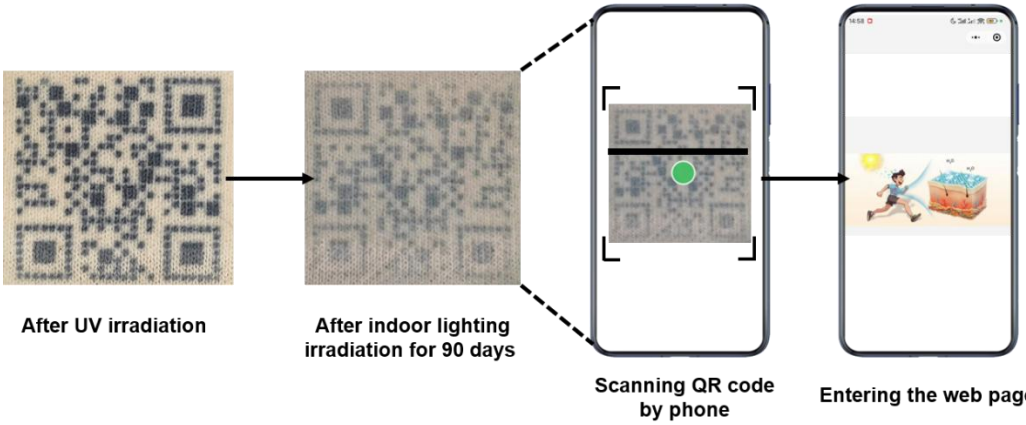

Figure 4.22 Images displaying the QR code on the MSPPTs can be recognized by phone after indoor lighting irradiation for 90 days.

4.3 Summary

In summary, a fiber-based photochromic wearable is developed using a scalable technology to modify the cotton fabrics with MSPN and long chain silyl group,

endowing the cotton fabrics with excellent photochromic performance. The photochromic fabric has excellent color-switching capacity under direct exposure to UV light and home wound disinfectant (from pale yellow to blue). The MSPPT exhibits excellent photochromic performance, such as superior fatigue resistance and reversibility (> 40 times), quick light response (reach color saturation with a UV dose of 60 kJ m^{-2}), and outstanding color retention capability (> 90 days). Through effective coating from long-chain silane groups and the strong encapsulation of a self-synthesized polymer network, this photochromic wearable can maintain great photochromic performance (fast writing-erasing cycles and excellent color retention time) after experiencing 20 cycles of washing and against the deterioration of acid solution, alkali solution and sweat (pH 2.0-9.0). Moreover, this photochromic fabric possesses the capacity to maintain a clear pattern when exposed to visible sunlight and exhibits excellent biocompatibility (cell viability > 100%). These characteristics make it a promising choice for everyday use in outdoor activities. Besides, the practical applications of the MSPPT in the domains of flexible wearable, photo-patterning, and information encryption have been demonstrated by writing-erasing of the clearly identifiable patterns and QR code identification system. In particular, this concept of using a MoO_3-based self-synthesized polymer network for the creation of photochromic dyes can be extensively applied to the fiber-based photochromic wearables. It paves a new route for achieving scalable, rapidly responsive, and color-retaining photochromic textiles in the field of sustainable photo-patterning recording/storage, smart textiles, and information security encryption.

Chapter 5. Sustainable Photochromic Wearables with Excellent Retention and Superior Stability for Customizable Patterns and Information Security Encryption

5.1 Introduction

The first work focuses on solving the combination fastness of photochromic materials and fabrics to prepare photochromic fabrics in large scale. Although it achieves excellent photochromic performance, durability and biocompatibility, their wearing comfort remains limited due to inadequate flexibility and breathability, which hinder the long-term wear. To realize a comfortable photochromic wearable system, it is necessary to further focus on improving the comfort and flexibility of fabrics without compromising photochromic performance.

The growing need for aesthetics, customization, and diverse textiles has propelled advancements in fiber-based wearables, including stimuli-switching devices, thermal-regulated textiles, wearable sensors, and antibacterial fabrics[146, 148-150, 187-189]. Consumers will discard and replace conventional garments featuring static patterns after repeated use because of their monotonous, immutable, and antiquated designs. This has led to the release of a massive amount of chemicals and human living products into the environment, escalating manufacturing cost and pollution. Fiber-based photochromic wearables are considered optimal for reducing costs and addressing environmental issues owing to their excellent light responsiveness, favorable fatigue resistance and reversibility, and diverse functionalities[152, 157, 190]. These wearables provide individuals with personalized options while demonstrating boundless inventiveness and potential in the convergence of technology and fashion.

Photochromic wearable that utilizes photochromic materials can switch their colors by the reversible transformation of photochromic materials between two states[154, 191, 192]. These wearables demonstrate considerable potential in optical data storage/recording, customizable patterns, photonic memory, ink-free printing, information security encryption, and optoelectronic devices[151, 156, 193, 194]. Currently, the research on photochromic wearables mostly focuses on improving their light response speed, color change intensity, and reversibility. Nevertheless, it is still a considerable challenge to develop fiber-based photochromic fabrics with great scalability, long color retention, and excellent environment-stability in face of the complex manufacturing process and inevitable environmental changes. Great scalability can markedly decrease manufacturing expenses, accelerate production processes, and improve the commercialization of production. Furthermore, longer color retention guarantees that the designs on photochromic wearables remain clear and visible after prolonged use, making them suitable for everyday wear. Excellent environment-stability enables photochromic wearables to keep stable photochromic performance despite fluctuations in the surrounding environment. Improving the commercialization and dissemination of photochromic textiles for attractive applications necessitates that these materials swiftly display distinct patterns, retain them for an extended period, and enable a rapid writing-erasing cycle for information transformation. Therefore, it is essential to develop scalable photochromic wearables with excellent color retention and extraordinary environmental stability for customizable patterns and information security encryption applications.

Photochromic materials, including organic materials such as spiropyran, spirooxazine, and diarylethene; transition metal oxides such as titanium dioxide, tungsten trioxide, and MoO_3 and polyoxometalates[154, 160-162, 195], have been

incorporated into fiber-based photochromic wearables for sustainable applications. MoO_3 is a multifaceted n-type semiconductor with potential applications in photochromic and electrochromic systems, electronics, catalysis, sensors, energy storage devices, and superconductors[164, 165] MoO_3 demonstrates excellent reversibility, rapid color transitions, high fatigue resistance and durability, and long color retention[165, 166], making it an exemplary option for photochromic wearables. However, the advancement of rewritable wearables based on MoO_3 continues to pose a significant barrier. When photochromic materials are incorporated into the fabric substrate through physical stress or weak interaction, it eventually leads to the degradation of the stability, durability, and photochromic functionality of photochromic fabrics after prolonged wear. In addition, the detergent (pH>8) used in the washing process will neutralize MoO_3, which will completely eliminate its photochromic properties. By putting photochromic materials inside microcapsules, sensitive substances can be physically enclosed in a protective matrix or wall materials. This protects the core materials from reactive and corrosive environments, resulting in better durability, fatigue resistance, and photochromic performance. Chitosan, a nitrogen-containing polysaccharide, has garnered significant interest in biomedicine, water treatment, cosmetics, food industry, textile industry, and agriculture owing to their inherent non-toxicity, biodegradability, biocompatibility, and antimicrobial properties[196-198]. Chitosan is a natural polymer that can be used as the wall of microcapsules. Its amino (NH_2) and hydroxyl (OH) groups help it stick strongly to textiles by reacting and coordinating with them. In addition, when a crosslinking agent is added to chitosan and nanoparticles, they can form a shell-core structure that effectively encloses the nanoparticles within the chitosan[199, 200]. Also, anions in SA can interact with cations in chitosan through electrostatic adsorption, bringing more

protection for MoO_3 nanoparticles even against damage from the outside. Therefore, it is important to develop a photochromic fabric with MM nanoparticles that can keep its photochromic properties even after being washed many times and exposed to different environmental conditions.

In this chapter, we have designed and developed a long-retention-time and highly environment-stability photochromic wearables utilizing MoO_3 for customizable patterns and information security encryption. The MM nanoparticles are incorporated into cotton fabrics through covalent grafting, utilizing their sheath-core structure. The integration is further stabilized as $-NH^{3+}$ on the nanoparticle surface engages with -COOH in SA via electrostatic forces and dehydration reactions, forming the photochromic wearables. The photochromic wearable shows great reversible "writing-erasing" capability (> 30 cycles), fast light response (color saturation with a UV dose of 48 kJ m^{-2}), and outstanding color retention capability (> 60 days). Additionally, this photochromic wearable has excellent environment-stability in avoiding the corrosion of repeated washing (15 cycles), various pH (pH 2.0–9.0), and temperature (-30–60°C) environments, benefiting from the tight encapsulation of chitosan and SA. Moreover, this photochromic fabric maintains a distinct pattern under both indoor and sunlight exposure and exhibits great biocompatibility (cell viability > 95%), indicating its suitability for daily use and athletic activities. As an application, a rewritable T-shirt and a QR code information security encryption system are demonstrated to validate the feasibility of the practical applications in customizable patterns and information security encryption. This study provides insights into the design and manufacture of scalable, long-color-retention, and environment-stable MoO_3-based wearable photochromic wearables, paving the way for realizing tremendous advancement in sustainable and smart textiles.

5.2 Results and Discussion

Figure 5.1a exhibits the fabrication procedure of SA/MM/Epoxy pristine cotton fabrics (SAME-PCFs) employing microcapsules technique, covalent grafting, and dehydration reactions. Initially, the PCFs were subject to NaOH solution treatment to eliminate oils and impurities, hence augmenting the presence of supplementary functional groups on the fiber surface. Subsequently, the PCFs were modified using KH560 to introduce epoxy groups onto the cotton fiber surface, resulting in E-PCFs. Next, E-PCFs were submerged in a MM nanoparticle solution, facilitating covalent interaction between E-PCFs and MM nanoparticles, hence resulting in the formation of ME-PCFs. Ultimately, SAME-PCFs were attained by integrating ME-PCFs with SA via electrostatic interactions and dehydration processes. The comprehensive materials and manufacturing methods are detailed in the experimental section.

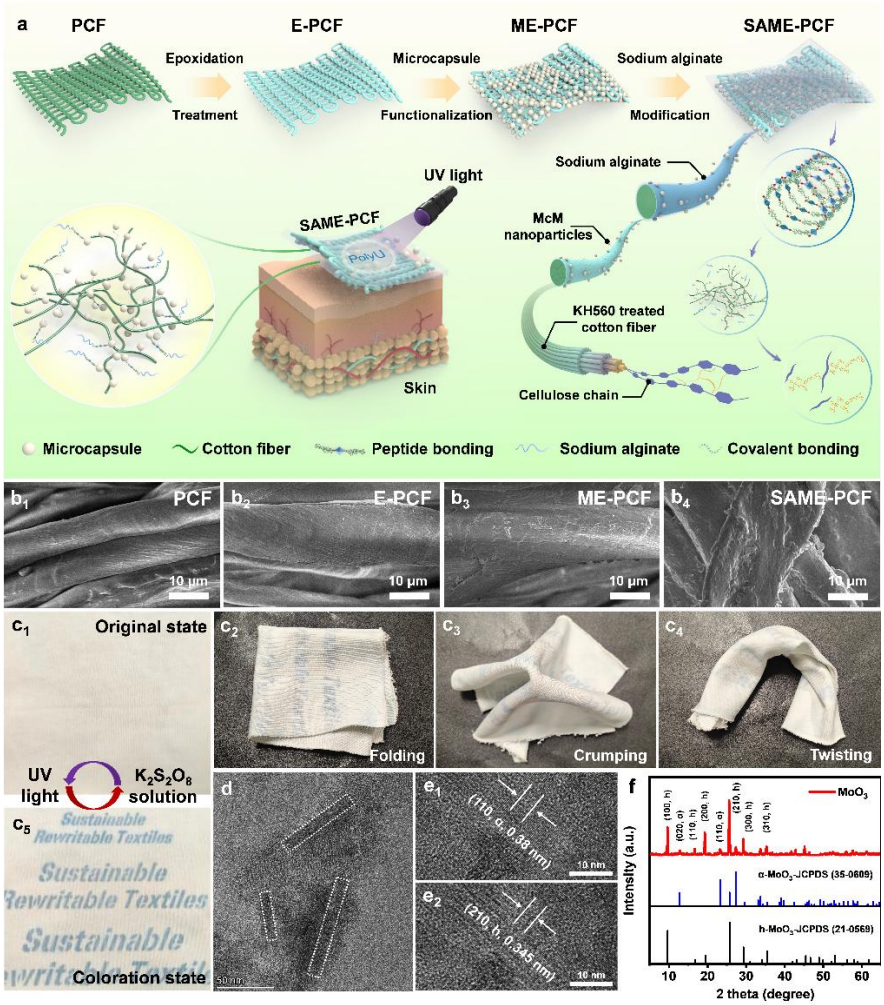

Figure 5.1 The fabrication of SAME-PCFs and characterization of MoO_3 nanoparticles and SAME-PCFs. a) Schematic diagram of procedure for preparing SAME-PCFs. b_1-b_4) Surface morphology of PCF SAME-PCFs. c_1-c_5) Images of the SAME-PCFs in different states (original state, folding state, crumping state, twisting state, and coloration state). d) TEM images of the prepared MoO_3 nanoparticles. e) High-resolution TEM image of the MoO_3 nanoparticles. f) XRD patterns of the prepared MoO_3 nanoparticles.

The SEM pictures of PCF, E-PCF, ME-PCF, and SAME-PCF were presented to illustrate alterations in fiber surface morphology. Figure 5.1b_1 illustrates the distinctive

wrinkling and scale architecture of the PCF's surface. After being treated with KH560, the cotton fiber surface attains a smooth texture with uniform folds (Figure 5.1b_2), showing successful modification of KH560. After the treatment with the MM nanoparticles, the ME-PCF surface exhibits increased roughness and a scaly texture akin to that of MoO_3 nanoparticles (Figure 5.1b_3), demonstrating the successful covalent grafting of MM nanoparticles. Figure 5.1b_4 displays a rougher cotton fiber surface, attributable to the tight adsorption of SA on the fiber surface. Figure 5.2 offers a comprehensive depiction via SEM images at different magnifications to corroborate the previously reported findings. Figures 5.1(c_1-c_4) illustrate the SAME-PCFs under various deformations (i.e., original, folding, crumpling, and twisting), demonstrating their remarkable flexibility and ease of integration into everyday fabrics. Figure 1C_5 shows the capability of SAME-PCFs to create and eliminate customizable patterns under UV light exposure and $K_2S_2O_8$ solution.

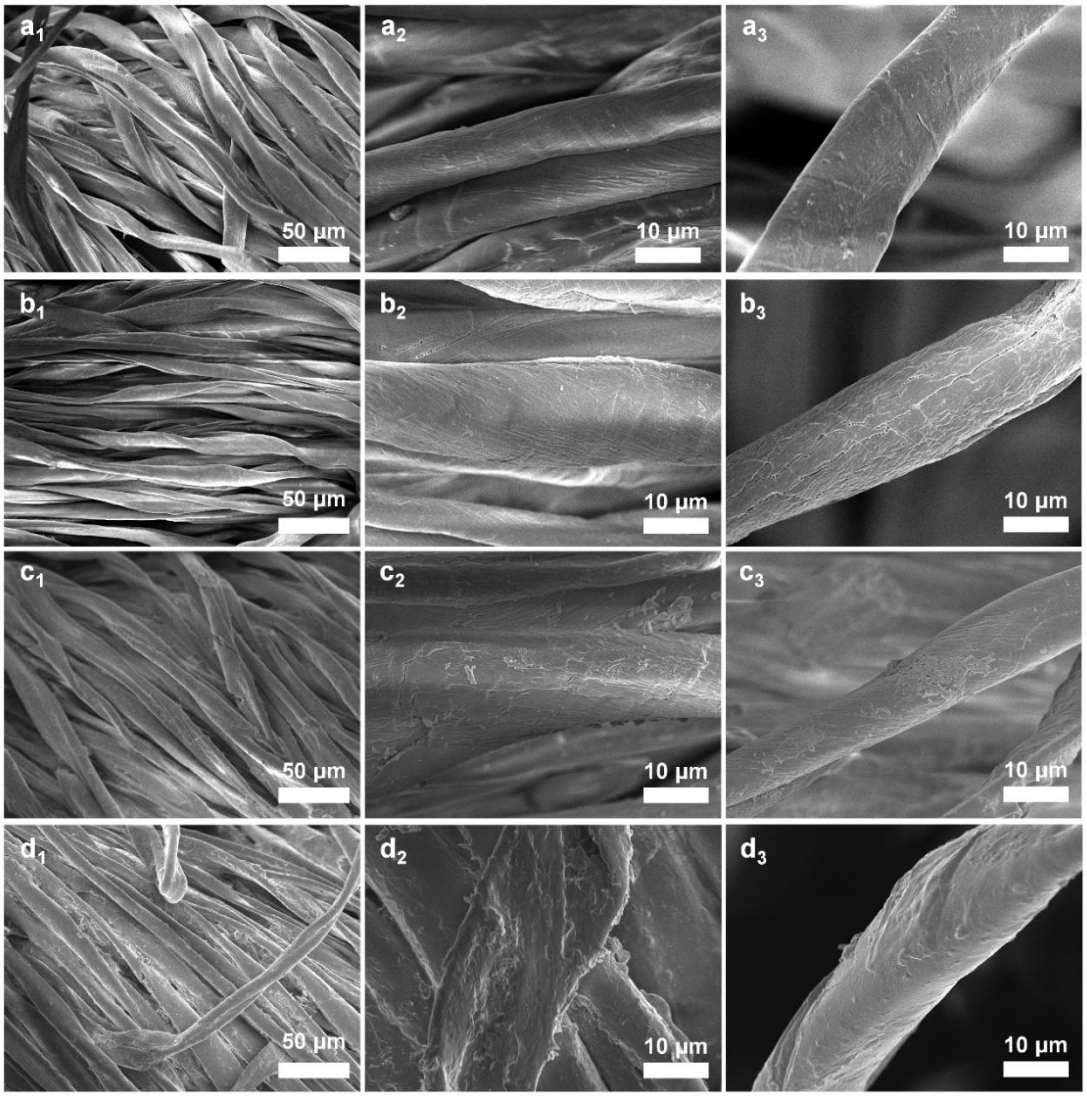

Figure 5.2 SEM images of a_1-a_3) the PCF, b_1-b_3) E-PCF, c_1-c_3) ME-PCF, and d_1-d_3) SAME-PCF at varying magnifications.

The morphology and structure of MoO_3 nanoparticles underwent further characterization. TEM images indicate that the synthesized MoO_3 nanoparticles' predominant morphological structure comprises nanosheets (Figure 5.1d). The nanosheet particles exhibit lengths between 50 and 100 nm, widths between 10 and 15 nm, and aspect ratios from 3.33 to 10. Hydrothermal synthesis of MoO_3 nanoparticles is depicted in Figure 5.3, which primarily comprises the nucleation and development

of the MoO_3 nanoflakes and the formation of secondary nanoflakes through directed aggregation of the primary nanoflakes.

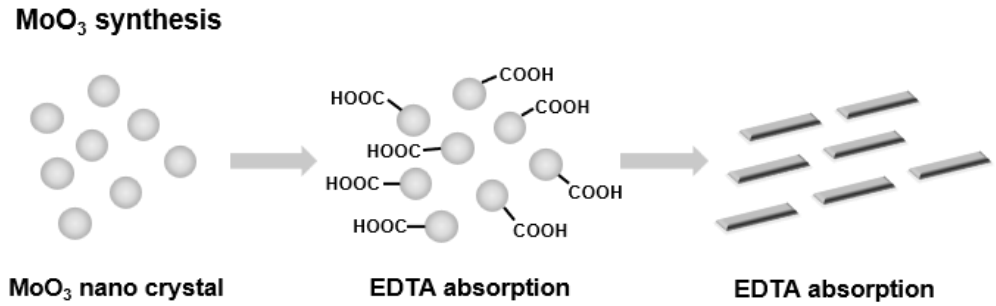

Figure 5.3 Schematic illustration of the formation mechanism of MoO_3 nanoparticles.

Figure 5.1e_1 and e_2 present high-resolution TEM pictures that demonstrate the lattice plane distance of 0.38 and 0.345 nm. These measurements pertain to the crystal plane in MoO_3 nanoparticles, indexed as (1 1 0, α) and (2 1 0, h). Figure 5.4 depicts the size distribution of the MoO_3 nanoparticles, indicating a primary size range of 60 to 250 nm, consistent with the TEM images. The nano-sheet and small-sized MoO_3 nanoparticles can be more easily combined with fibers along their surfaces, enhancing bonding strength and improving photochromic properties.

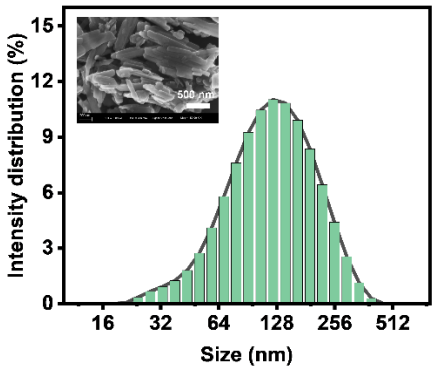

Figure 5.4 Size distribution of the MoO_3 nanoparticles.

According to the standard powder diffraction files JCPDS 21-0569 and 35-0609, Figure 5.1f illustrates that the diffraction peak results from both the h-MoO_3 and the α-

MoO_3. The hexagonal and orthorhombic phases of MoO_3 have a narrower band gap and smaller band gap energy. This property facilitates the separation of electrons and holes while enhancing the diffusion of photo-induced protons, leading to a better photochromic effect[174, 175].

We further assessed the binding mechanism in the manufacture of SAME-PCFs (Figure 5.5a). During the epoxidation treatment, KH560 easily hydrolyzes in water and converts alkyl siloxane into silanol. The cotton fabric, consisting of cellulose, is abundant in positively charged functional groups, such as hydroxyl groups. The silanol in KH560 reacts directly with hydroxyl groups on the cotton fiber surface, leaving the epoxy groups on the surface of PCF exposed, creating the E-PCF (chemical reaction i). In the chemical reaction ii, MoO_3 nanoparticles cross-link with the amino group on the surface of the chitosan and the aldehyde group of GA solution, leading to the formation of the MM nanoparticles with shell-core structure. In the subsequent next step iii, a nucleophilic addition reaction takes place, and the strong covalent bonds are made between the $-NH^{3+}$ groups on the shell of the MM nanoparticles (at pH 5) and epoxy groups on the surface of E-PCF. Robust covalent bonding can guarantee the stability and durability of the MM nanoparticles on the ME-PCF's surface. In the chemical reaction iv, the $-NH^{2+}$ on the wall material of the microcapsule is converted into $-NH^{3+}$ and the carboxyl group in the SA molecule remains as -COOH at pH 5. The extra $-NH^{3+}$ on the surface of MM nanoparticles attracts the -COOH in SA through electrostatic force and dehydration reaction, and the SAME-PCFs are obtained.

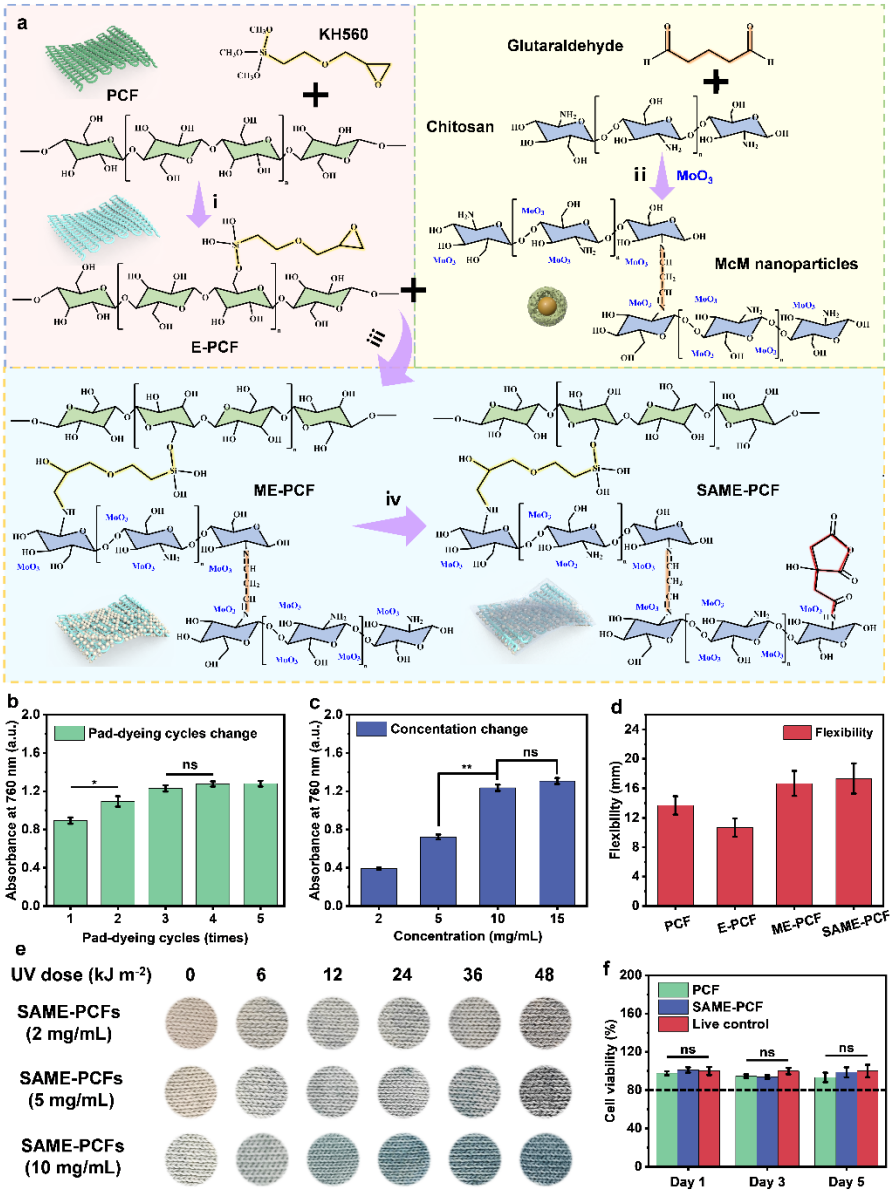

Figure 5.5 The binding mechanism and performance of the photochromic fabrics. a) The bonding mechanism for fabricating SAME-PCFs. b) Photographs of SAME-PCFs with different MM nanoparticle concentrations. c) The absorbance changes of the SAME-PCFs with increasing pad-dyeing cycles. d) The absorbance changes of the SAME-PCFs with increasing concentration of MM nanoparticles. e) The change in flexibility for preparing SAME-PCFs. f) Cell viability for the PCF, SAME-PCFs, and control after 1, 3, and 5 days of incubation.

Figure 5.5b shows how the UV-vis absorbance of SAME-PCFs changed after going through different pad-dying cycles. When the concentration of MM nanoparticles is 10 mg mL^{-1}, the absorbance of SAME-PCF is about 0.89. It goes up to about 1.23 when the number of pad-dyeing cycles goes from 1 to 3. Afterwards, the absorbance only attains around 1.28 as the pad-dyeing cycles rise from 3 to 5. We also evaluated the effect of concentration on the photochromic performance of SAME-PCFs subject to 3 pad-dyeing cycles (Figure 5.5c). The absorbance of the SAME-PCFs increases from around 0.4 to 1.23 as the concentration of MM nanoparticles escalates from 2 to 10 mg mL^{-1}. Thereafter, the absorbance gradually increases to about 1.30 at a concentration of 15 mg mL^{-1}. Given the procedure's complexity and efficiency, the SAME-PCF subject to 3 pad-dyeing cycle iterations at a concentration of 10 mg mL^{-1} was selected for future investigation. Figure 5.5d illustrates that the PCF and E-PCF exhibit greater flexibility, measuring 13.7 mm and 11 mm, respectively. Following the alteration of cotton fibers with MM nanoparticles and SA, they retain remarkable flexibility, measuring approximately 16.7 and 17.3 mm. The superior flexibility ensures that the photochromic wearables conform closely to the intricate deformations of the human body. Upon irradiation with UV light (λ = 365 nm), all the photochromic textiles progressively transitioned to blue (Figure 5.5e). However, SAME-PCFs treated with 10% MM nanoparticles show a stronger photochromic reaction when exposed to the same UV light as SAME-PCFs treated with 2% and 5% concentrations of MM nanoparticles. Cytotoxicity and skin allergy tests confirmed the excellent biocompatibility of SAME-PCFs, crucial for daily use safety, human skin protection, and sustainable and eco-friendly development. Figure 5.5f illustrates that SAME-PCFs maintain a cell vitality of approximately 99% (> 80%) after 5 days, which is equivalent to the viability of PCFs (93%). Figure 5.6 illustrates the optical density (OD) values of

the PCF, SAME-PCFs, and control, indicating a gradual increase in OD values over time.

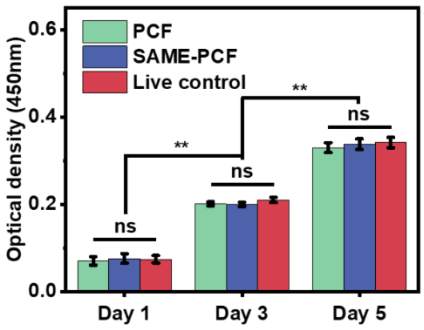

Figure 5.6 Absorption at 450 nm in MTT assay of different incubation groups after 1, 3 and 5 days of incubation.

Furthermore, the findings of the skin allergic reaction test demonstrated that SAME-PCF is non-harmful to the skin (Figure 5.7). One can directly apply it to the skin without any additional treatment, and it continues to be non-irritating even after 72 hours of application. These demonstrate that the SAME-PCF, possessing superior biocompatibility, satisfies the criteria for wear safety and prevents harm to human skin.

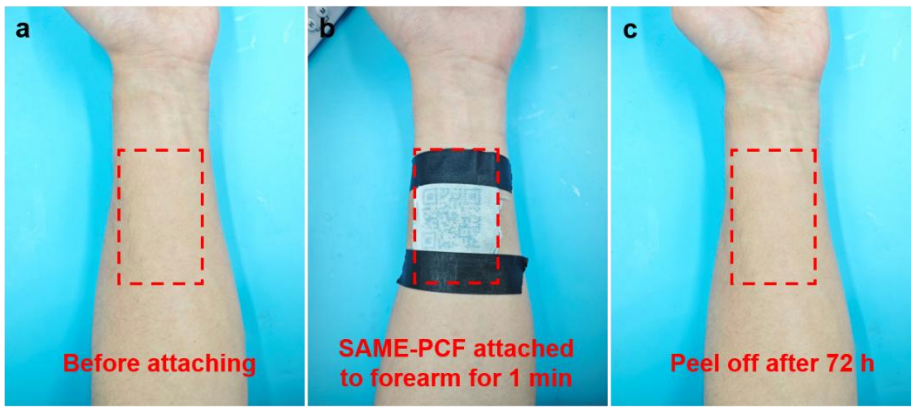

Figure 5.7 Digital images showing the skin irritation results of SAME-PCFs on the forearm.

Figure 5.8a illustrates the mechanical properties of the PCF, E-PCF, ME-PCF, and

SAME-PCF. The application of MM nanoparticles and SA enhances breaking strength, elongation, and modulus.

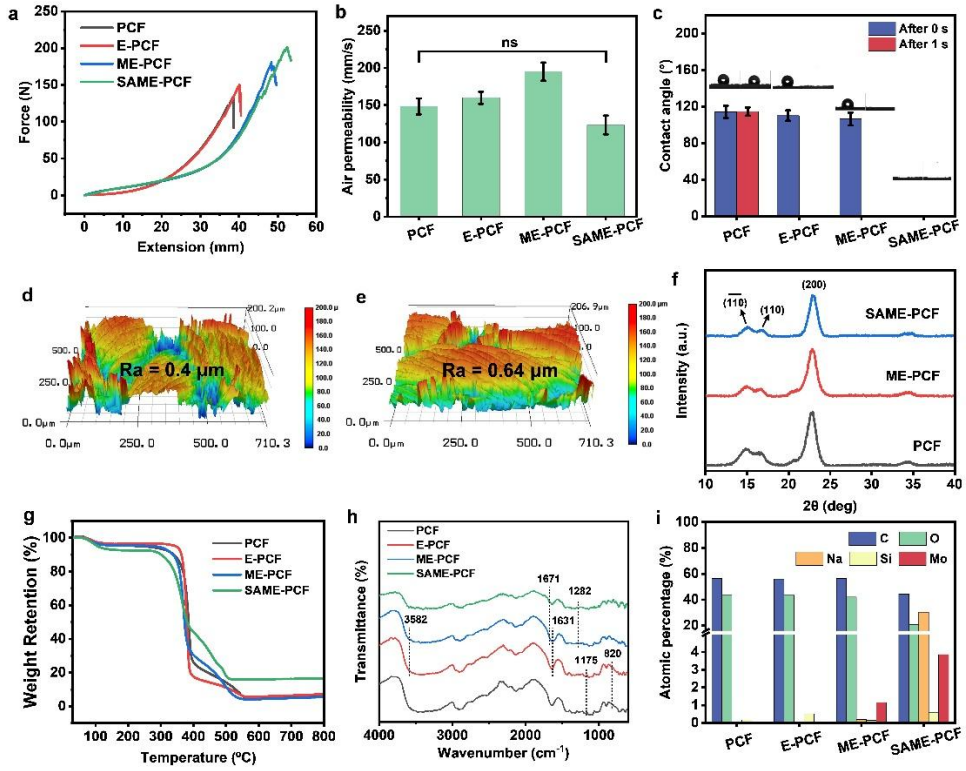

Figure 5.8 Characterization of the MoO_3 nanoparticles and fabrics. a) The force-elongation of the PCF, E-PCF, ME-PCF, and SAME-PCF. b) Air permeability of cotton fabrics before and after treatment. c) Contact angle of the cotton fabrics before and after functionalization. d) Surface roughness of the PCF. e) Surface roughness of the SAME-PCF. f) XRD profile of PCF, ME-PCF, and SAME-PCF. g) Thermal stability of the cotton fabrics before and after modification. h) FT-IR spectra of the PCF, E-PCF, ME-PCF, and SAME-PCF. i) Element content of the cotton fabrics before and after functionalization.

The PCF and E-PCF exhibit breaking strengths of around 131.5 N and 155 N, respectively. The strength rises to approximately 181.3 N following treatment with a solution of MM nanoparticles. After the SA solution modification, the valve's force

increases to roughly 204 N. The PCF and the E-PCF exhibit initial elongation of around 38.3 and 40.1 mm, respectively. The elongation markedly increases with the application of MM nanoparticles and SA coating, attaining approximately 48.4 and 52.4 mm, respectively. The incorporation of MM nanoparticles with high mechanical strength and SA enhances the connection between fibers. Meanwhile, the robust covalent connection between the negatively charged components of the MM nanoparticles and the positively charged functional groups of the cotton fiber substantially enhances the mechanical properties of the fabric. We evaluated and examined the air permeability of cotton fabrics prior to and during functionalization. Figure 5.8b shows the PCF has exceptional air permeability, with an air resistance of about 148 mm/s. After treatment with KH560 and MM nanoparticles solution, the air permeability rises to approximately 160 and 195 mm/s, respectively. Following SA modification, the air permeability of the SAME-PCF exhibits a minor reduction to roughly 123.3 mm/s while still maintaining a high level. The SA coating obscures some apertures in the fabric where the fibers interlace, leading to the reduction. High air permeability of SAME-PCF can facilitate the expulsion of human metabolites, including sweat and heat, into the ambient environment; hence, it preserves the comfort of photochromic fabrics throughout wear. Figure 5.8c illustrates the alterations in the surface hydrophilicity of these textiles as the dipping times vary. All sample contact angles exhibit 0° after 5 s (Figure 5.9). The PCF exhibits a contact angle of approximately 114.2° (with a dipping duration of 0 seconds), decreasing to roughly 108.2° after 1 s. The E-PCF and ME-PCF show contact angles of 110° and 106.3° (with a dipping duration of 0 s), rapidly decreasing to 0° after 1 s of dipping. This is due to the abundance of hydrophilic functional groups on the surface of cotton fiber, including hydroxyl and carboxyl groups. Conversely, the contact angle of SAME-PCF remains

at 0° from 0 s to 5 s owing to the exceptional hydrophilicity of SA. The coating of MM nanoparticles and SA retains the excellent hydrophilicity and wearing comfort of the fabric.

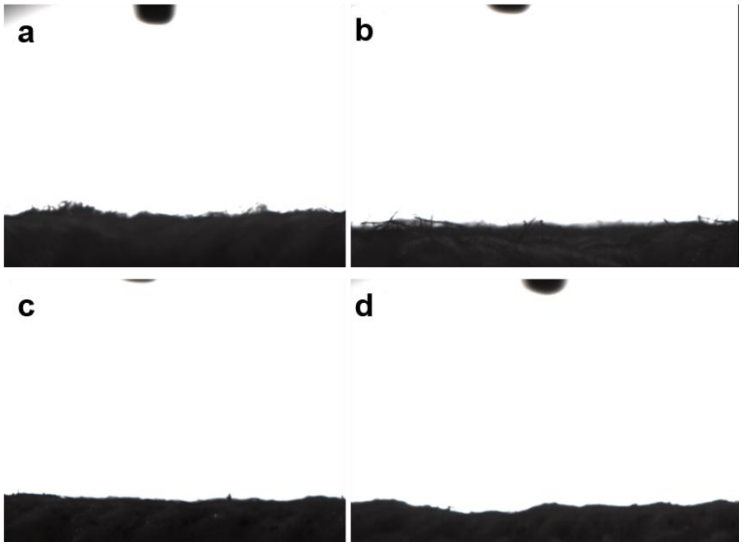

Figure 5.9 Images of contact angle for the (a) PCF, (b) E-PCF, (c) ME-PCF, and (d) SAME-PCF.

The alteration in the surface macrostructure of samples pre- and post-functionalization is also evident through surface roughness (Figure 5.10). The SAME-PCF has a higher roughness (0.64 μm) than the PCF (0.4 μm) because of the presence of MM nanoparticles and SA coating (Figures 5.8d, e).

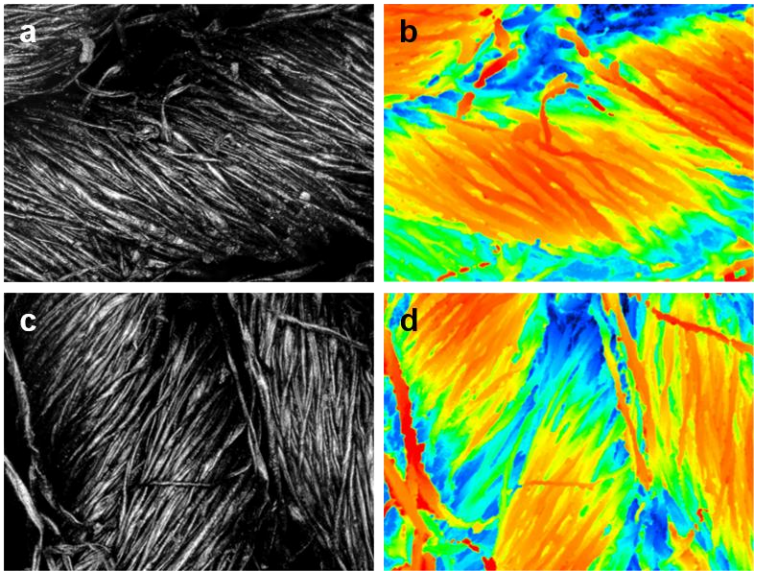

Figure 5.10 a) Image of the PCF. b) High-resolution image showing the roughness of the PCF. c) Image of the SAME-PCF. d) High-resolution image showing the roughness of the SAME-PCF.

Additionally, SAME-PCF and ME-PCF exhibit analogous XRD patterns to those of PCF. This suggests that the arrangement of cellulose molecules did not change after MM nanoparticles and SA modification (Figure 5.8f) [188]. Figure 5.8g illustrates the thermal stability of PCF, E-PCF, ME-PCF, and SAME-PCF. As the temperature rose from 30 to 800°C, the samples experienced significant weight loss, exceeding 80%. The weight reduction noted at approximately 100°C is primarily owing to water evaporation within the fiber. At roughly 350°C, these fabrics experienced weight loss due to the decomposition of cellulose in cotton fibers. Prior to 380°C, the E-PCF demonstrates improved stability and less weight loss owing to the modification of KH560. The ME-PCF exhibits thermal degradation between 270 and 320°C, attributable to the decomposition and oxidation of chitosan. Moreover, the incorporation of MoO_3 nanoparticles in ME-PCF and SAME-PCF leads to a reduction in both the rate and extent of weight loss at roughly 400°C. Furthermore, SAME-PCF

indicates that the weight drops at 200°C is attributable to the disintegration of the SA framework, which results in the creation of an intermediate stable product. The procedure removes adjacent hydroxyl groups as water molecules. The continued oxidative breakdown of the SA carbide is responsible for the observed weight loss at a temperature of 520°C. Figure 5.8h shows the FT-IR spectra of cotton fabrics before and after functionalization. Characteristic peaks are observed at approximately 820 cm^{-1}, 1,175 cm^{-1}, 1,282 cm^{-1}, 1,631 cm^{-1}, 1,671 cm^{-1}, and 3,582 cm^{-1}, corresponding to the bending vibrations of C-C, the asymmetric stretching vibration of Si-O-Si, the free -COO^-, the vibration of -COOH, the C=N of the Schiff base, and the stretching vibration of -NH_2, respectively. The peaks at 820 cm^{-1} and 1,175 cm^{-1} signify that KH560 has successfully adapted to PCF. The modification of MM nanoparticles induced ME-PCF shows new peaks at 1,631 cm^{-1} and 3,582 cm^{-1}, attributed to the effective cross-linking of chitosan by GA. Additionally, following the application of the SA coating, the peaks at around 1,282 cm^{-1} and 1,671 cm^{-1} emerge owing to the amplification of free -COO-. The proportion of surface elements in the samples changed significantly during the photochromic functionalization process. The PCF reveals an atomic makeup of 56.35% carbon, 43.44% oxygen, 0% natrium, 0.17% silicon, and 0.04% molybdenum. The KH560 modification changes the values to 55.95%, 43.51%, 0.02%, 0.51%, and 0.01% (Figure 5.8i), and the increase in Si content validates the successful modification of the silane coupling agent for the PCF. Following the amalgamation of MM nanoparticles with cotton fiber, the Mo content rises to 1.16%, indicating effective microcapsule modification. After SA treatment, the Na content greatly increases to 30.41%, showing successful combination between SA the ME-PCF. Figure 5.11 illustrates the elemental distribution on the fiber, indicating a homogeneous distribution of the respective elements without any aggregation.

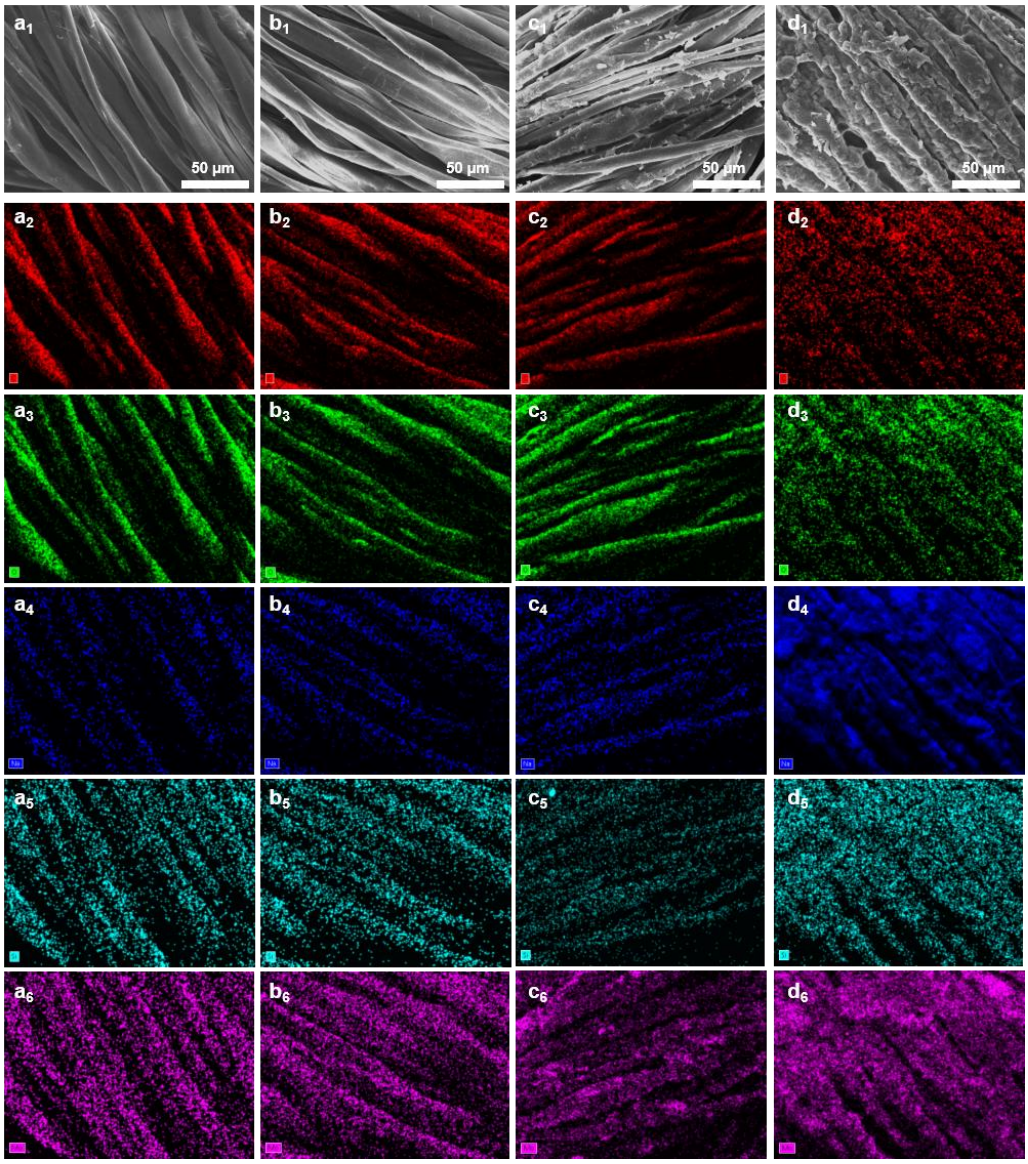

Figure 5.11 SEM images and element distribution of samples. a) SEM image and C, O, Na, Si, and Mo distribution of the PCF. b) SEM image and C, O, Na, Si, and Mo distribution of the E-PCF. c) SEM image and C, O, Na, Si, and Mo distribution of the ME-PCF. d) SEM image and C, O, Na, Si, and Mo distribution of the SAME-PCF.

The chemical composition and bonding states of the photochromic wearables were further investigated using XPS. Figure 5.12 shows the distinct peaks at 285.0 eV, 532 eV, 400 eV, 231.0 eV, 1071 eV, and 101 eV attributed to C 1s, O 1s, N 1s, Mo 3d, Na

1s, and Si 2p respectively. The C and O elements come from the cellulose of the PCFs, as well as the N, Mo, Na, and Si elements come from MM nanoparticles and SA.

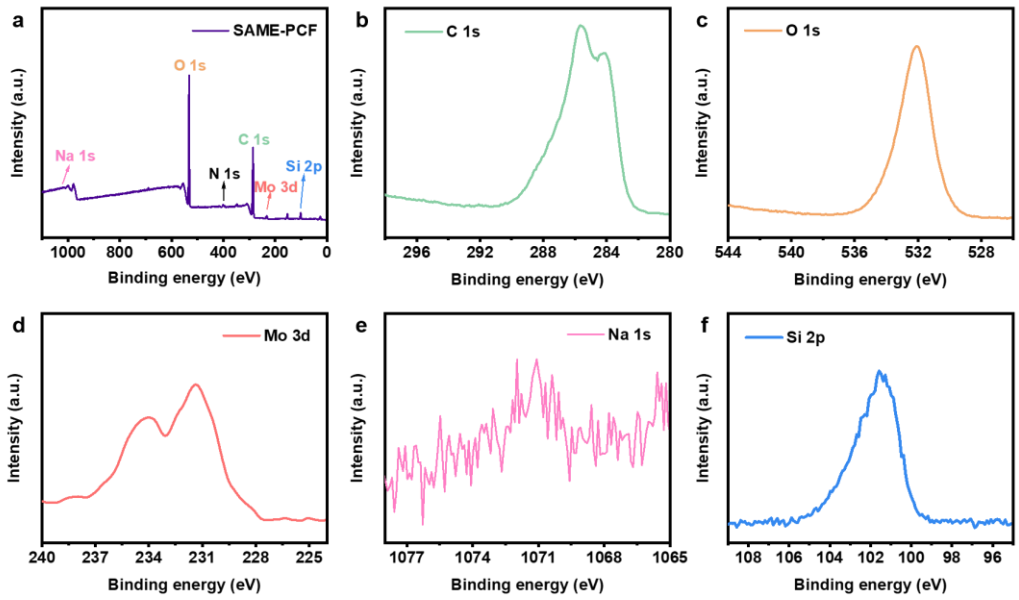

Figure 5.12 a) XPS spectra of SAME-PCF. b) C 1s XPS spectrum of SAME-PCF. c) O 1s XPS spectrum of SAME-PCF. d) Mo 3d XPS spectrum of SAME-PCF. e) Na 1s XPS spectrum of SAME-PCF. f) Si 2p XPS spectrum of SAME-PCF.

The photochromic reaction and the potential photochromic mechanism of the SAME-PCF are shown in Figure 5.13a. Upon exposure to UV light, the SAME-PCF transitions in color from pale yellow to blue, proving that photochromic properties of MoO_3 nanoparticles were not impacted by Chitosan encapsulation. The color shift is attributable to the photochemical reduction of MM nanoparticles. Hydrogen protons participating in the reduction of Mo^{6+} likely originate from the hydroxyl groups of chitosan molecules, since chitosan tightly encapsulates MoO_3 nanoparticles. Hydrogen protons on the photochromic fabric are transferred to the metal atom Mo^{6+} via the charge transfer bridge in chitosan, leading to the reduction of Mo^{6+} to Mo^{5+} and the conversion of heteropoly blue[73, 164]. After being treated with a $K_2S_2O_8$ solution, it

reverts to its original color through a reverse reaction involving electron transfer from Mo^{5+} atom to oxygen molecules.

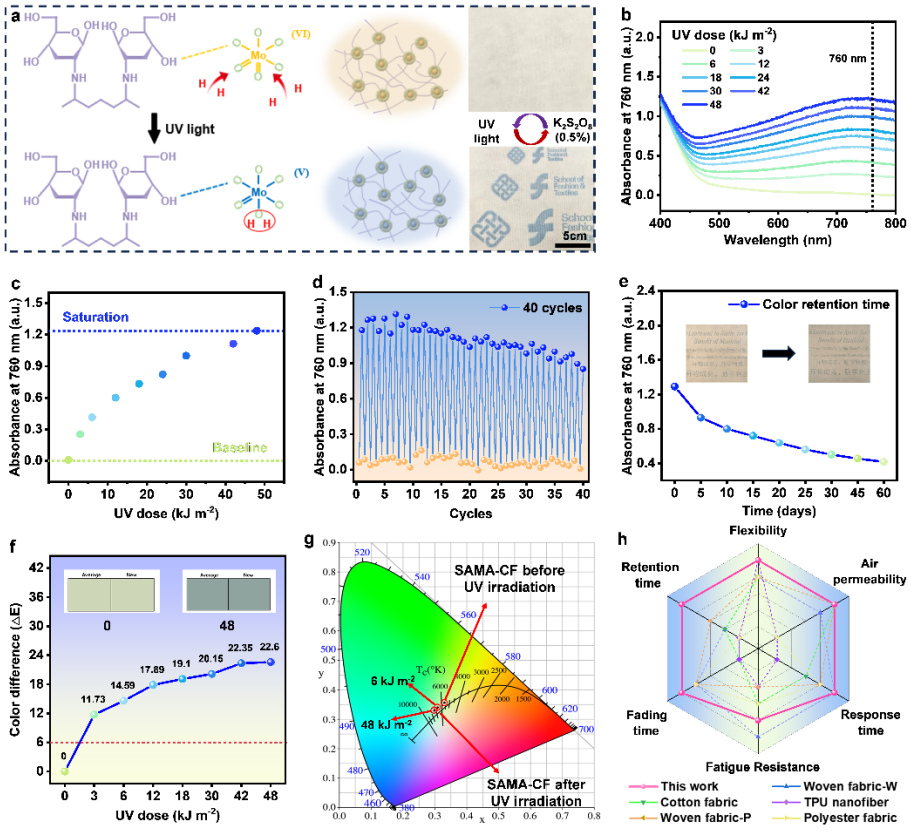

Figure 5.13 Photochromic mechanism and performances of the SAME-PCFs. a) Photochromic reaction mechanism of SAME-PCFs. b) UV-vis absorbance spectra of the SAME-PCFs with increasing exposure to UV light (λ= 365 nm). c) Absorbance at 760 nm as a function of UV dose for the SAME-PCFs. d) Absorption intensity represents the fatigue resistance of the SAME-PCFs switching color from pale yellow to blue. e) The change in UV-vis absorbance at 760 nm indicates the retention time of the SAME-PCFs in 60 days. f) Color difference (ΔE) of the SAME-PCFs with increasing UV dose *via* Macbeth Color-Eye 7000A under CIE standard illuminant D65 and 10° standard chromaticity. g) CIE coordinate diagrams of pristine cotton fabric and the SAME-PCFs before and after UV irradiation in the (x, y) chromaticity diagram. h)

Comparison of the performances between various photochromic wearables.

The alterations in the electronic structure of the materials is illustrated throughout the photochromic transformation, hence enhancing comprehension of the photochromic mechanism of the SAME-PCFs. When UV light interacts with MoO_3 nanoparticles, the photon energy exceeds the bandgap (hv > Eg). This induces the migration of electrons from the valence band to the conduction band, simultaneously generating an equivalent number of holes in the valence band. The excitation leads to the generation of electron-hole pairs, as seen in Equation (1). The SAME-PCFs, which intrinsically hold moisture inside their structure, generate the requisite protons for the photochromic reaction by the interaction of the adsorbed water with holes, as seen in Equation (2). The MoO_3 nanoparticle subsequently acquires these protons, resulting in the generation of $H_xMo_x^{V}Mo_{1-x}^{VI}O_3$, as depicted in Equation (3). Simultaneously, Mo^{6+} acquires one electron from its surroundings, converting to Mo^{5+} (Equation 4). The charge transfer between the newly formed Mo^{5+} in the valence band and the adjacent Mo^{6+} in the conduction band induces a blue coloration in the MoO_3 nanoparticles (Equation 5)[164]. Upon reintroduction to an oxygen-rich environment ($K_2S_2O_8$ solution), the Mo^{5+} is reoxidized to Mo^{6+}, causing the MoO_3 nanoparticles to revert to their original pale-yellow state. XPS measurement was used to characterize the valence changes of Mo atoms, showing the content changes in Mo^{6+} and Mo^{5+} of the SAME-PCFs before and after UV irradiation. After UV irradiation, the content of Mo^{5+} increase slightly, because some Mo^{6+} are transferred to Mo^{5+} when they get an electron from its surroundings.

$$MoO_3+hv\rightarrow MoO_{3*}+e^-+h^+ \quad (1)$$

$$2h^++H_2O\rightarrow 2H^++O \quad (2)$$

$$MoO_3+xe^-+xH^+\rightarrow H_xMo_x^{V}Mo_{1-x}^{IV}O_3 \quad (3)$$

$$Mo^{6+}+e^{-}\rightarrow Mo^{5+} \quad (4)$$

$$hv+Mo_A{}^{5+}+Mo_8{}^{6+}\rightarrow Mo_A{}^{6+}+Mo_8{}^{5+} \quad (5)$$

The photochromic performances of SAME-PCF, including coloration intensity, response time, retention time, and color difference, were then measured and assessed using a UV-vis spectrophotometer. Figure 5.13b shows a broad absorption band near 760 nm, attributable to the reduction of Mo^{6+} to Mo^{5+}.[184] The absorption intensity of SAME-PCF at a wavelength of 760 nm increases from approximately 0.01 to 1.23 with increasing UV dose, until it reaches a saturation point at a UV dose of 48 kJ m^{-2}. This is accompanied by a noticeable shift in the color of the SAME-PCF from pale yellow to blue following exposure to UV light (Figure 5.13c). The images in Figure 5.14 display the alteration in color of SAME-PCF as the UV irradiation time increases. Then, the absorption intensity of SAME-PCF undergoes an obvious decline after treatment of a 0.5% $K_2S_2O_8$ solution with a temperature of 80°C.

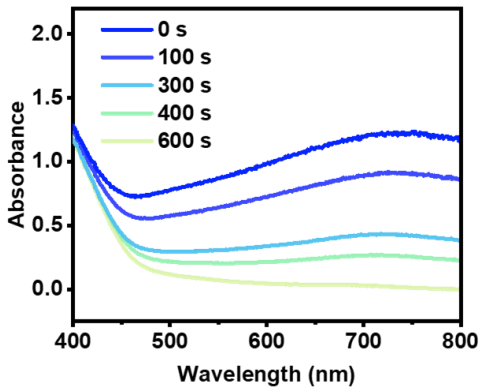

Figure 5.14 UV-vis absorbance spectra of the MSPPTs in the process of color-fading with increasing time.

In the production of wearable photochromic fabrics, it is essential to assess their fatigue resistance and color retention duration[156]. Figure 5.13d illustrates the fatigue resistance of the photochromic wearables by quantifying the absorbance levels in both

colored and bleached conditions. The absorption intensity of SAME-PCFs at a wavelength of 760 nm shows a slight decrease from around 1.2 to 0.85 after 40 cycles, suggesting that SAME-PCFs possess exceptional fatigue resistance and offer considerable potential in customizable photo-patterning information storage/recording. Figure 5.13e illustrates that the absorbance of SAME-PCFs diminishes from around 1.2 to 0.41 over 60 days, indicating that SAME-PCFs exhibit remarkable color retention. The SAME-PCFs demonstrate one of the longest color retention durations among all reported photochromic textiles. The exceptional fatigue resistance and prolonged color retention indicate that the SAME-PCFs have significant practical application potential in sustainable, long-lasting, and efficient customizable photo-patterning textiles. Color difference (ΔE) and chromaticity are additionally quantified to demonstrate the coloration intensity of SAME-PCFs. The color variation in Figure 5.13f demonstrates that the SAME-PCFs undergo a significant color transformation during the photochromic process. At a UV dosage of 3 kJ m^{-2}, the ΔE is 11.73 (ΔE > 6). The ΔE then escalates to 22.6 as the UV dose is augmented to 48 kJ m^{-2}. Furthermore, elevated UV exposure results in a consistent reduction in the reflectance of the SAME-PCFs (Figure 5.15).

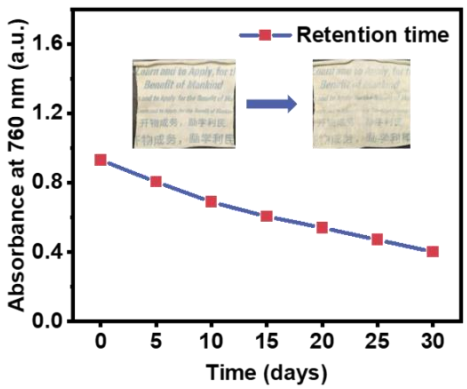

Figure 5.15 Absorbance of SAME-PCFs before and after washing.

Figure 5.13g depicts the CIE 1931 chromaticity diagram of the PCF and SAME-PCFs after exposure to UV irradiation. When exposed to 365 nm UV light with the UV dose of 6 and 48 kJ m^{-2}, the SAME-PCFs' coordinates are far distant from the PCF, revealing an apparent color gap. Compared with existing photochromic fabrics, SAME-PCFs demonstrate comprehensive advantages, including excellent flexibility, superior air permeability, great fatigue resistance, great color retention time, short fading time, and fast response time (Figure 5.13h, Table 5.1, and Table 5.2).

Table 5.1 Performance comparison between our photochromic fabric and reported photochromic fabrics

Substrate	Photochromic material	Response time (s)	Fading time	Retention time (days)	Fatigue resistance (cycles)	Air permeability	Flexibility	Refs
Cotton fabric	$Na_4W_{10}O_{32}$	< 60	120 min	0.08	> 20	✓	-	[101]
Woven cotton fabric	WO_3	5	5 min	> 7	> 100	✓	38	[161]
Cotton fabric	PMoA	< 60	-	> 10	> 20	✓	21	[73]
Woven cotton fabric	ZnO	5	50 s	0.09	> 35	×	-	[160]
Woven cotton fabric	PMoA	30	-	> 15	> 10	✓	33	[157]
TPU nanofiber	WO_3	300	30 min	0.5	> 6	×	-	[185]
Cotton fabric	Spiropyran	10	50 s	0.003	> 20	✓	-	[97]
Polyester fabric	Hackmanites	15	50 min	0.03	> 20	-	-	[186]
Knitted fabric	MoO_3	10	2.5 min	> 90	> 40	✓	69	[190]
Knitted cotton fabric	MoO_3	10	10 min	> 60	> 40	✓	17	This work

Table 5.2 Performance evaluation of various photochromic fabrics (grade is divided

into five grades).

Substrate	Color retention	Fatigue resistance	Flexibility	Air permeability	Response time	Fading time	Refs
Woven cotton fabric-P	3	2	4	5	4	4	[157]
Woven cotton fabric-W	2	5	4	4	5	4	[161]
Cotton fabric	2	3	4	5	3	1	[101]
TPU nanofiber	1	2	5	1	1	1	[185]
Polyester fabric	1	3	4	1	4	4	[186]
Knitted cotton fabric	5	4	5	5	5	5	This work

Color retention denotes the ability of photochromic wearables to preserve their color state following exposure to UV light. Extended color retention duration guarantees that photochromic fabrics maintain long-lasting clarity in customizable patterns for sustainable applications. To enhance the clarity and professionalism of comparing and evaluating the color retention capacity of various photochromic fabrics. The color retention ability is categorized into five levels: the first level indicates a duration of less than 1 day, the second level indicates a duration of 1–10 days, the third level indicates a duration of 11–30 days, the fourth level indicates a duration of 31–60 days, and the fifth level indicates a duration beyond 60 days.

Fatigue resistance refers to the quantity of reversible writing-erasing cycles that photochromic fabric may undergo. High fatigue resistance enables photochromic materials to preserve their life and functionality following repeated use in customizable patterns and information encrypting applications. To enhance the clarity and professionalism of comparing and evaluating the fatigue resistance of various photochromic materials. Five level categorize the fatigue resistance: the first level corresponds to 1–5 cycles, the second level to 6–10 cycles, the third level to 11–30 cycles, the fourth level to 31–60 cycles, and the fifth level to more than 60 cycles.

A highly flexibility can enhance the overall user experience by making the photochromic wearables more comfort, durability, and more satisfied. To facilitate a more accurate and professional comparison and assessment of flexibility. Flexibility is classified into five levels. The first level is the wearables cannot be bent, the second level is the wearables can be slightly bent, the third level is the wearables based on nonwoven fabrics and polymers can be easily bent, the fourth level is the wearables based on woven fabrics can be easily bent, and the fifth level is the wearables based on knitted fabrics and nanofibers can be easily bent.

Air permeability is described as a fabric's capacity to allow air to pass through it. High fabrics' air permeability can diminish the accumulation of heat and moisture, hence lowering the likelihood of skin irritations and infections. To enhance the clarity and professionalism of comparing and evaluating the air permeability of various photochromic materials, Air permeability is categorized into five levels. The first level is less than 5 mm/s, the second level is between 5 and 10 mm/s, the third level is between 10 and 100 mm/s, the fourth level is between 50 and 100 mm/s, and the fifth level is greater than 100 mm/s.

In practical customizable patterns and information security encryption applications, a rapid response time guarantees a steady and seamless transition between writing and erasing states, while also delivering a dynamic and responsive user experience. To enhance the clarity and professionalism of comparing and evaluating the response times of various photochromic materials. The response time is categorized into five levels: the first level is greater than 300 s, the second level is 101-300 s, the third level is 31-100 s, the fourth level is 11-30 s, and the fifth level is 1-10 s.

The rapid fading time can ensure a seamless shift of color throughout the photochromic fabric's repeated writing-erasing process. To enhance the clarity and

professionalism of comparing and evaluating the fading time of various photochromic fabrics. The fading time is categorized into five levels: the first level is > 24 h, the second level is 6-24 h, the third level is 1-6 h, the fourth level is 5-60 min, and the fifth level is < 5 min.

Photochromic wearables frequently encounter diverse environmental alterations, including pH variations and laundering, during everyday use; thus, assessing their stability in intricate and dynamic conditions is crucial. Because MoO_3 is an acidic oxide, it takes part in a neutralization reaction in alkaline conditions that makes molybdate and water. Detergents like alkaline solutions (pH > 8) can entirely eradicate the photochromic properties of MoO_3. MoO_3 nanoparticles can be contained within a small area of chitosan by encasing them in chitosan and SA. This can protect them from damage from the outside, such as acidic and alkaline solutions and washing. Figure 5.16a shows that chitosan surrounds MoO_3 nanoparticles, and MM nanoparticles treated with SA can easily and quickly change colors when exposed to UV light and a $K_2S_2O_8$ solution. The images of the MoO_3 and MM nanoparticles are shown in Figure 5.16b. Compared to the MoO_3 nanoparticles (Figure 5.16b_1), the MM nanoparticles possess the coarse and uneven surface that is similar to polymer wrinkle (Figure 5.16b_2). This shows that the MM nanoparticles form a shell-core structure with MoO_3 nanoparticles as the core and chitosan as the shell. We show a schematic diagram of the acid- and alkali-resistant photochromic wearable system in Fig. 5.16c to show how stable SAME-PCFs are in complex environments. The chitosan and SA network forms a protective barrier around the MoO_3 nanoparticles. This barrier not only facilitates reversible color switching using $K_2S_2O_8$ solution but also prevents performance degradation from acidic solution or alkaline laundry detergents.

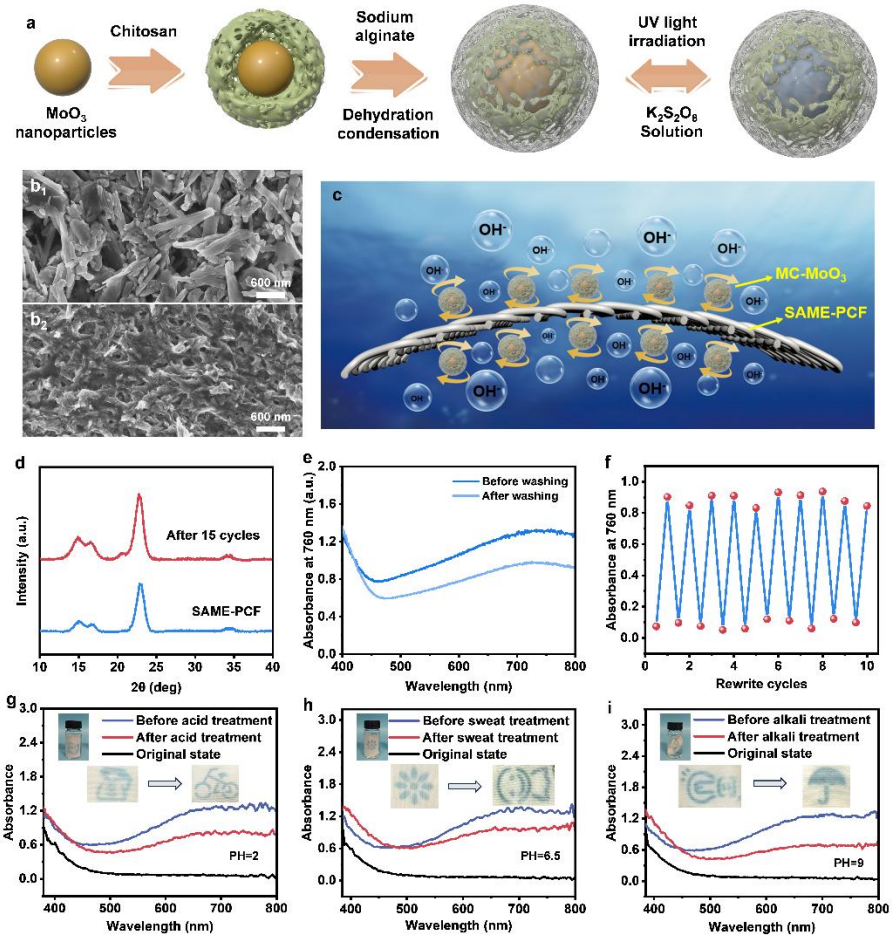

Figure 5.16 Stability of Photochromic performances of the SAME-PCFs. a) Schematic diagram of MoO_3 nanoparticles encapsulated by chitosan and SA. SEM images of the b_1) MoO_3 nanoparticles b_2) MM nanoparticles. c) Illustration of SAME-PCFs showing great stability in facing varying pH environments. d) XRD patterns of SAME-PCFs before and after washing. e) The UV-vis absorbance spectra of SAME-PCFs with UV irradiation of 48 kJ m^{-2} after washing. f) Absorption intensity represents the fatigue resistance of the SAME-PCFs after washing. g) The change in absorbance of SAME-PCFs after acid treatment. h) The change in absorbance of SAME-PCFs after sweat treatment. i) The change in absorbance of SAME-PCFs after alkali treatment.

The XRD profiles of SAME-PCFs show the same diffraction patterns before and

after washing (Figure 5.16d), verifying that the washing process did not change the structure of the materials. We then assessed the photochromic performance of SAME-PCFs using a UV-vis spectrophotometer after washing. As shown in Figure 5.16e, the absorption intensity of SAME-PCFs at a wavelength of 760 nm shows a modest decline from approximately 1.3 to 0.85 after undergoing 15 cycles of washing. Figure 5.16f illustrates that the absorbance value of SAME-PCFs is approximately 0.85 following a repeated pattern over 10 cycles after washing. The SAME-PCFs exhibit excellent washing fastness, which is essential for routine soaking and laundering with detergent. In addition, this photochromic fabric has exceptional stability over a range of pH settings (pH: 2-9). Figures 5.16g and h exhibit that the UV absorbance of SAME-PCF treated with the acid and artificial sweat solution remains stable, and Figure 5.16i shows the UV absorbance of SAME-PCF treated with alkali solution shows a relative decrease. This demonstrates that the strong encapsulation for MoO_3 by chitosan and the SA enables the SAME-PCFs to maintain their outstanding photochromic performance even when the pH level changes. The exceptional washing fastness and remarkable environment-stability indicate that the SAME-PCFs have significant practical application potential in sustainable, long-term, efficient, and stable photo-patterning fabrics, even under adverse conditions. The high fatigue resistance, great washing fastness, and excellent stability suggest that the SAME-PCFs have considerable practical application potential in customizable patterns sustainable and information security encryption, even in harsh situations.

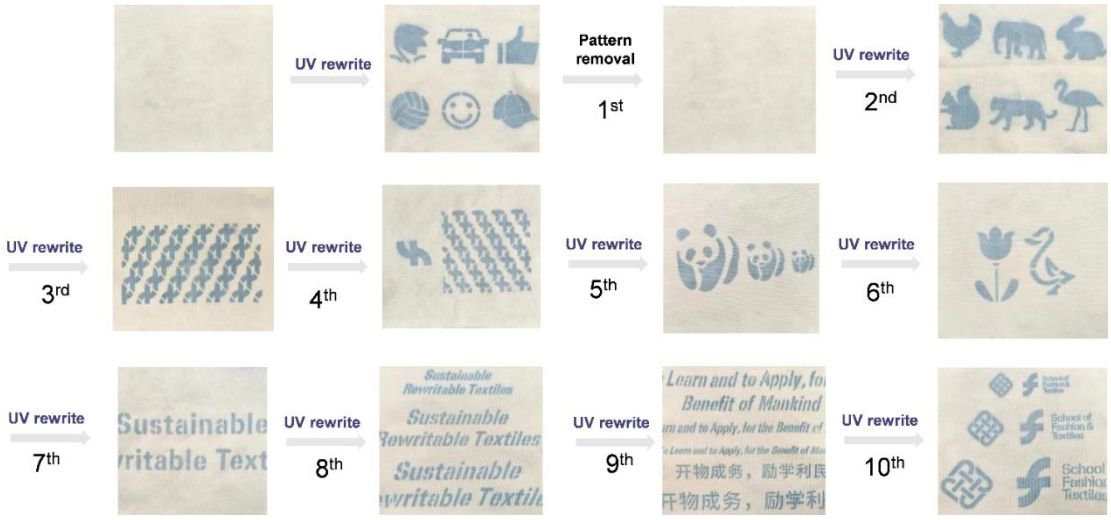

Figure 5.17 The images showing the 10 writing-erasing cycles of SAME-PCFs with a size of 400 cm^2 before washing.

The stability of photochromic fabric across a broad temperature range and its insensitivity to sun radiation guarantee that the designs on the fabric remain distinct throughout several seasons for prolonged outdoor use and athletic endeavors. Figure 5.18a reveals the SAME-PCFs have stable photochromic properties during temperature variations between -30 to 60°C, which is attributed to the excellent thermal stability of the MoO_3 nanoparticles. Figure 5.18b illustrates that the absorption intensity of SAME-PCFs rises to around 0.3 at a wavelength of 760 nm following one day of indoor light exposure, without compromising the clarity of the fabric pattern. Figure 5.18c shows that the absorption intensity of unoccupied area on the SAME-PCFs rises to about 0.45 after sunlight exposure for 6 h (a UV index of 7, 175 mW/m^2). These demonstrate that the SAME-PCF can maintain distinct patterns during prolonged indoor illumination and solar exposure. We have conducted experiments on customizable patterns of SAME-PCFs for rewritable image data. The SAME-PCFs demonstrate the inscription and removal of distinctly recognizable patterns, such as a plane, snowman, bus, and fork (Figure 5.18d). The printed designs are easily removable and maintain their

visibility in environmental conditions for at least 60 days. Furthermore, Figure 5.17 shows the writing-erasing cycles of 400 cm^2 SAME-PCFs that were done 10 times. This shows that SAME-PCFs can be easily used for scalable customizable patterns application. Figure 5.18e illustrates that the rewritable T-shirt, manufactured using the same production technique, possesses the capability to customize patterns. The patterns can be removed using an aqueous $K_2S_2O_8$ solution at 80°C, restoring the SAME-PCF T-shirt to its original pale-yellow state for subsequent UV printing, allowing the rewritable T-shirt to be adorned with various designs. After UV irradiation with a customized mask, the clearly identifiable pattern can be easily printed on the SAME-PCFT-shirt (Figure 5.18e_2). The pattern can be erased and other patterns can be printed by UV irradiation (Figure 5.18e_3). Figure 5.18e_4 shows the photos of volunteers wearing clothes, and the patterns are clearly visible. Furthermore, the exceptional stability and durability guarantee the longevity of the SAME-PCF T-shirt under typical wear and usage conditions. To execute SAME-PCFs' information storage and encryption capabilities, the image depicted in Figure 5.16c was encoded and stored within a QR code. When a UV lamp was used to shine on the skeletonized QR code mask, a clear QR code showed up on the surface of the SAME-PCFs, with a resolution of about 1 mm (Figure 5.18f). Mobile phones can swiftly identify the QR code and direct users to the webpage featuring Figure 5.16c. This demonstrates that SAME-PCFs have considerable potential for use in anti-counterfeiting marks and information security encryption.

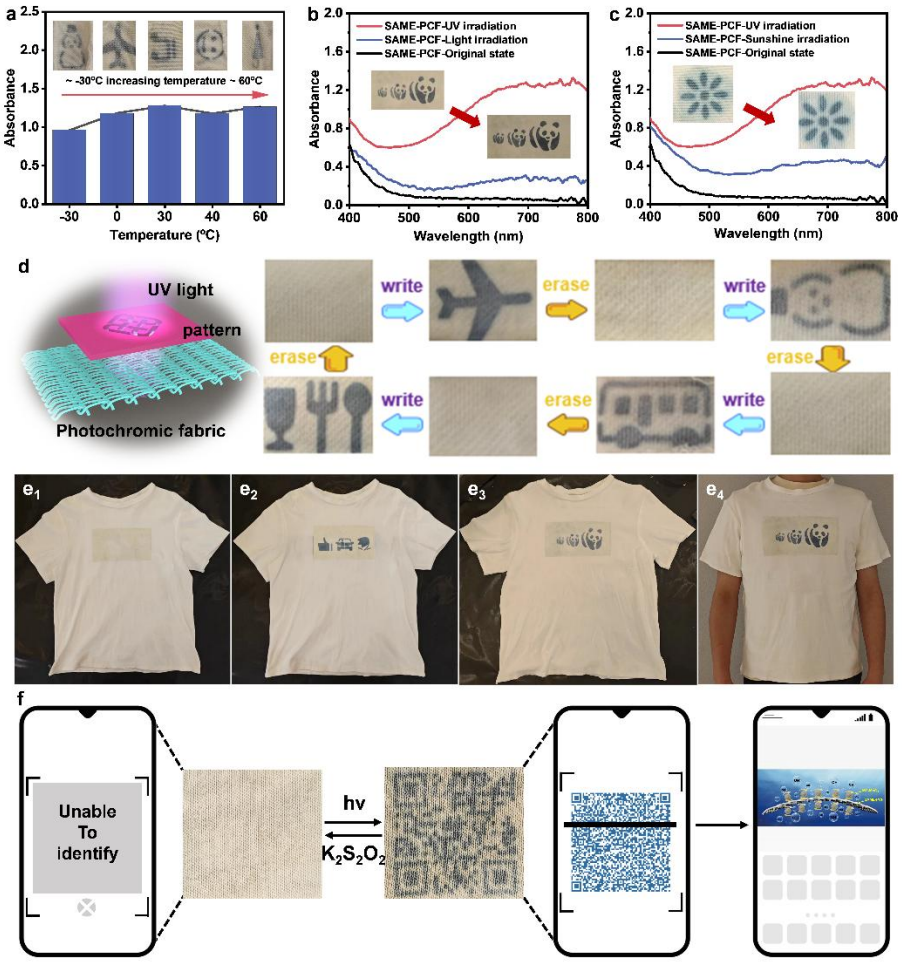

Figure 5.18 Practical application of SAME-PCFs. a) The absorbance change of SAME-PCFs in the various temperatures. b) The absorbance of SAME-PCFs under the indoor light. c) The absorbance of SAME-PCFs under the sunshine. d) Images showing the customizable patterns of SAME-PCFs for rewritable image data. e) Images displaying the volunteer wearing the photochromic textile with different patterns. f) Application of SAME-PCFs in QR code information security encryption system.

5.3 Summary

In summary, we design and employ a scalable technology for developing photochromic fabrics by integrating the MM nanoparticles with sheath-core structure

into PCFs through covalent bonds and combining MM nanoparticles with SA by electrostatic force and peptide linkage. The prepared photochromic fabric shows reversible color conversion from pale yellow to blue under exposure to UV light and $K_2S_2O_8$ solution. The SAME-PCF possesses excellent photochromic performance including great fatigue resistance (> 40 cycles), fast light response reaching color saturation with a UV dose of 48 kJ m^{-2}, and superior color retention time (> 60 days). Owing to the encapsulation of chitosan and SA for MoO_3 nanoparticles, the photochromic wearable has great stability in various harsh environments such as acid solution, alkali solution, sweat (pH 2.0-9.0), indoor and sunshine irradiation, and sustain repeated washing. Moreover, this photochromic fabric exhibits great wearability with excellent flexibility of 17 mm and biocompatibility (cell viability > 95%). These characterizations promote it as a promising choice for daily wear and sports. Besides, a rewritable T-shirt and a QR code information security encryption system by the SAME-PCFs have been presented, demonstrating its potential in the domains of customizable patterns, flexible rewritable textile, and information security encryption. In particular, this concept of using encapsulation technology to endow MoO_3 nanoparticles with durability and stability for the creation of MoO_3-based photochromic dyes can be extensively applied to the photochromic wearables. It paves a new route for achieving scalable, sensitive light response, environment-stability, and color-retaining photochromic textiles in the field of customizable patterns recording/storage, smart textiles, and information security encryption.

Chapter 6. Highly Stretchable and Biocompatible Gelatin Biogels for Bioelectronic and Healthcare Applications

6.1 Introduction

Having established photochromic textiles for dynamic visual interfaces, we turn to a complementary requirement: wearables capable of continuous physiological monitoring. Such applications demand materials that closely match the soft, dynamic nature of biological tissues while maintaining stable electrical signaling. To address these challenges, developing a wearable system that integrates high stretchability, cyclic durability, and biocompatibility, thereby extending our wearable platform toward multifunctional health-sensing systems has become crucial.

Wearable electronic devices have emerged as transformative technologies owing to their enormous potential in real-time health monitoring, human-computer interaction, and personalized medical diagnosis[201]. They can seamlessly conform to the complex curves of the human body and continuously collect physiological signals, providing critical data for disease early warning, rehabilitation assessment, and vital sign management. Significant progress has been achieved with stretchable strain sensors capable of acquiring precise signals from both subtle physiological motions (e.g., respiration, phonation) and large-scale deformations (e.g., joint articulation). Advanced bioelectronics enable capture diverse bioelectric signals (including EMG, ECG, EOG, and EEG)[202], and they can even be safely and reliably applied to implantable scenarios to achieve deeper physiological information acquisition or therapeutic intervention. However, developing a comprehensive, fully-integrated multifunctional electronic network capable of seamless whole-body coverage—simultaneously

monitoring mechanical deformations, multiplexed bioelectric activities, and implantable functionalities—remains a formidable challenge.

Wearable electronics, such as hydrogel sensors, which can establish a robust and conformal interface between bioelectronics and living tissues is paramount for accurate, high-fidelity physiological signal recording[203, 204]. Natural hydrogels, such as gelatin, SA, and chitosan, are promising candidates with their inherent biocompatibility, biodegradability, and natural abundance. These materials can effectively conform to body surfaces, detecting both large deformations and subtle strains, while serving as electrodes for electrophysiological signal acquisition[205]. Furthermore, their excellent biocompatibility and biodegradability enable implantation with minimized mechanical and biological rejection. Among these, gelatin—a collagen hydrolysate—stands out. It offers high water content, excellent biocompatibility, degradability, and abundant active groups that facilitate functional modification[206]. These properties make gelatin an ideal matrix for multifunctional flexible electronic platforms integrating sensing, electrophysiological monitoring, and implantable devices[207]. However, gelatin-based hydrogels suffer from limitations including poor mechanical strength, rapid dehydration in ambient environments, low ionic conductivity, and inadequate stability under cyclic stretching. Strategies to overcome these challenges have been explored, such as building double networks or interpenetrating networks with other polymers (e.g., PAM or polyvinyl alcohol) to enhance mechanical strength; chemical cross-linking (e.g., via glutaraldehyde or methacrylate followed by photo crosslinking) to significantly enhance mechanical integrity and dissolution resistance; incorporating hygroscopic agents (e.g., glycerol, sorbitol) to retain moisture; and enhancing ionic conductivity through post-synthesis immersion in salt solutions (e.g., LiCl, NaCl, KCl)[208] or by incorporating conductive fillers (e.g., PEDOT:PSS,

graphene, carbon nanotubes). However, developing gelatin-based hydrogels that combine high mechanical strength and toughness, long-term environmental stability (hydration retention), high and stable ionic conductivity, and excellent fatigue resistance remains a considerable challenge.

PCA-Zn, a natural moisturizing factor (NMF) component of skin, regulates hydration, elasticity, and ionic conductivity. Beyond its inherent hygroscopicity that mitigates rapid water loss [8], PCA-Zn delivers mobile Zn^{2+} ions, substantially enhancing ionic conductivity essential for high-fidelity electrophysiological signal acquisition. Concurrently, its carboxyl groups ionically crosslink with amine groups in gelatin, directly reinforcing the hydrogel's mechanical integrity. The intrinsic biocompatibility, antibacterial efficacy, and wound-healing properties of Zn^{2+} establish PCA-Zn as an ideal candidate for durable, biocompatible bio-interfaces. In addition, cellulose nanofibers (CNF) consisting abundant surface hydroxyl groups can form a hydrogen bond-reinforced network with gelatin[209], markedly improving mechanical strength and cyclic stability. Its hierarchical structure establishes nanofluidic ion channels[210], synergistically boosting conductivity alongside PCA-Zn. Integrating XG—a biocompatible polysaccharide—as a physical crosslinker introduces entangled molecular chains that dissipate energy, endowing the hydrogel with high stretchability, elasticity, and fatigue resistance.

In this chapter, we design a highly stretchable, biocompatible, and multifunctional gelatin-based biogel integrating PCA-Zn, CNFs, and XG (G-ZCX biogel) through synergistic ionic crosslinking and hydrogen bonding. This strategy utilizes PCA-Zn for ionic conductivity and dynamic crosslinking, while physical entanglement and hydrogen bonding brought from CNFs and XG further enhance hydrogels' mechanical properties. The prepared biogel achieves low modulus (0.1-0.5 MPa), high

stretchability (286.7%), and fatigue resistance (>10,000 cycles), ensuring chemomechanical tissue matching and high ionic conductivity. Furthermore, the G-ZCX biogel enables seamless wearability for full-range body motion detecting and high-accuracy gesture recognition (99.8%). An advanced bioelectronics platform is established through the biogel to monitor multimodal electrophysiological signals (EMG/ECG/EOG/EEG) with excellent signal fidelity (signal-to-noise ratio (SNR): 26.3 dB). Cell Cytotoxicity and in vivo implantation experiments demonstrate the excellent biocompatibility of the G-ZCX biogel, with inflammation essentially eliminated after 14-day implantation. This work presents a comprehensive technique and multipurpose platform for highly stretchable and biocompatible hydrogel-based electronic devices, demonstrating great potential for applications in flexible wearable electronics, implantable electronics, telemedicine, and medical rehabilitation.

6.2 Results and Discussion

PCA-Zn, a constituent of the NMF, demonstrates intrinsic hygroscopic properties that reduce rapid water loss. The liberated Zn^{2+} ions from PCA-Zn are uniformly distributed inside the hydrogel, acting as mobile charge carriers that confer substantial ionic conductivity. The protonated amino groups ($-NH_3^+$) of PCA-Zn ionically cross-link with the carboxylate groups ($-COO^-$) in gelatin, resulting in a stable network. Nanocellulose and XG offer nanoscale reinforcement via hydrogen bonding and molecular entanglement, respectively, thereby augmenting mechanical strength, structural stability, and water retention capacity. A stretchable, biocompatible, and multifunctional biogel is developed using a multi-layered synergistic cross-linking approach. The schematic fabrication process for the G-ZCX biogels is depicted in Figure 6.1a. Initially, gelatin powder was thoroughly dissolved in deionized water.

PCA-Zn was subsequently introduced and agitated for 30 mins. CNFs were subsequently included, and the mixture was agitated for an additional hour. XG was subsequently included and agitated for an additional hour to yield G-ZCX biogels. The materials and fabrication procedures are detailed in the experimental section.

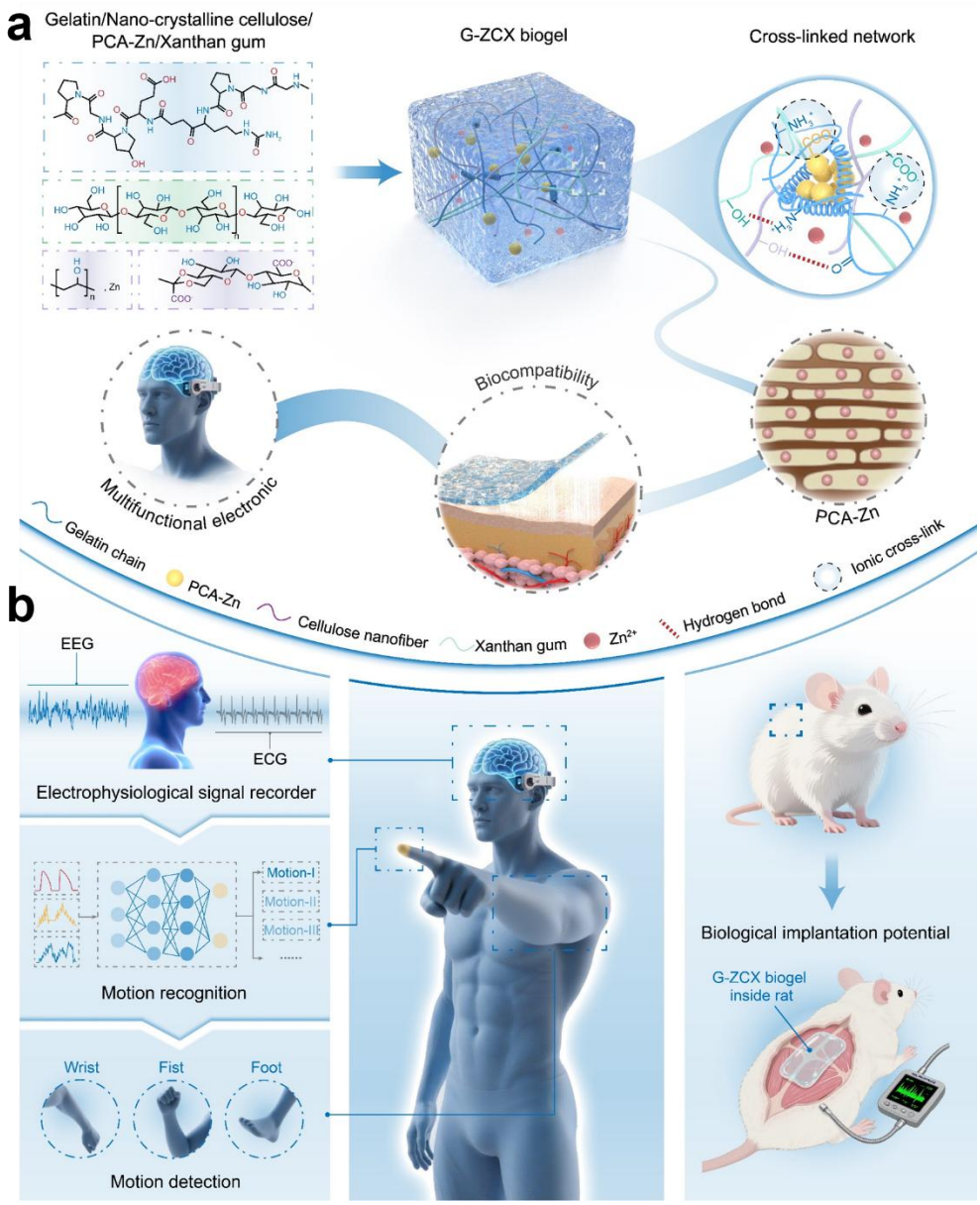

Figure 6.1 Schematic preparation of G-ZCX biogels and its multifunctional electronic applications. a) Fabrication procedure of the G-ZCX biogels. b) Bioelectronic and healthcare applications of G-ZCX biogels.

The G-ZCX biogels, consisting all all-natural and safe components, exhibit high stretchability, exceptional biocompatibility, and versatile functionality, demonstrating transformative potential for next-generation wearable and implantable bioelectronics. Leveraging its 286.7% elongation and robust tissue adhesion, the hydrogel achieves seamless conformation to dynamic joints and tissues, facilitating high-fidelity monitoring of complex physiological activities. As demonstrated in Figure 6.2b, we constructed a multifunctional whole-body sensing network by integrating this hydrogel directly onto the skin or wearable devices. This platform enables real-time tracking of full-body kinematics (e.g., limb motions) and subtle gesture recognition (e.g., finger articulation, speech-associated movements), highlighting its potential for movement analysis and medical rehabilitation. When coupled with Ag/Cl electrodes, the hydrogel permits continuous acquisition of key electrophysiological signals—including EMG, ECG, EOG, and EEG—enabling comprehensive human electrophysiological monitoring. Critically, the hydrogel's inherent biocompatibility supports its use in implantable medical devices for long-term muscle and cardiac signal acquisition without triggering chronic immune responses. By bridging high-performance sensing, long-term biosafety, and adaptive biomechanical compatibility, this technology establishes a versatile platform for advanced medical diagnostics, intelligent human-machine interfaces, and closed-loop therapeutic systems.

Table 6.1 Biogel recipes with varying compositions.

	Gelatin/g	**PCA-Na/g**	**CNFs/g**	**XG/g**	**Deionized Water/mL**
G	1.5	0	0	0	8
G-Z-0.2	1.5	0.2	0	0	8
G-Z-0.5	1.5	0.5	0	0	8
G-Z-0.7	1.5	0.7	0	0	8
G-ZC-0.1	1.5	0.5	0.1	0	8
G-ZC-0.2	1.5	0.5	0.2	0	8

G-ZC-0.3	1.5	0.5	0.3	0	8
G-ZCX-0.08	1.5	0.5	0.1	0.08	8
G-ZCX-0.16	1.5	0.5	0.1	0.16	8
G-ZCX-0.24	1.5	0.	0.1	0.24	8

Stretchability is a fundamental mechanical property that determines the functional feasibility of hydrogels for multifunctional electronic applications. By adjusting the weight ratio of PCA-Zn, CNF, and XG on the properties of G-ZCX biogels, a series of biogel formulations were prepared. Details of these formulations can be found in Table 6.1. Furthermore, to ensure accurate mechanical testing without compromising the integrity of the test, a suitable fixture configuration was designed. As shown in Figure 6.2a, the breaking strain of the unmodified gelatin hydrogel was merely 70%. The incorporation of PCA-Zn markedly enhanced the elongation at break of the G-Z hydrogel. This results from the robust electrostatic interactions between the positively charged amide groups in gelatin and the negatively charged groups in PCA-Zn, markedly improving the stability of the gelatin network. With the addition of 0.5 g of PCA-Zn, the elongation at the break of the G-Z hydrogel attained a peak of 173.5%. The further incorporation of CNFs (0.1-0.7 g) with the addition of 0.5 g of PCA-Zn considerably improved the mechanical properties of the G-ZC hydrogel, elevating them from 173.5% to 226.9% (Figure 6.2b). The elevated specific surface area of the CNFs facilitates the formation of robust hydrogen bonds with the gelatin/PCA-Zn network, serving as physical crosslinks that impede molecular chain slippage and consequently augment the hydrogel's stretchability. Nevertheless, as the quantity of CNFs surpassed 0.1 g, the stretchability of the hydrogel network diminished. This decline is due to the incapacity of high-concentration CNFs to be encapsulated by the gelatin/PCA-Zn network and the creation of stress concentration spots following self-aggregation. The

incorporation of XG establishes a dynamic physical entanglement network inside the hydrogel matrix and increases the formation of hydrogen bonds, hence augmenting the stretchability of the gelatin hydrogel. At a dosage of 0.16 g, the G-ZCX biogel achieved a maximum elongation of 286.7% (Figure 6.2c). Additionally, the stress of hydrogel in Figure 6.2d shows the stress of hydrogel samples.

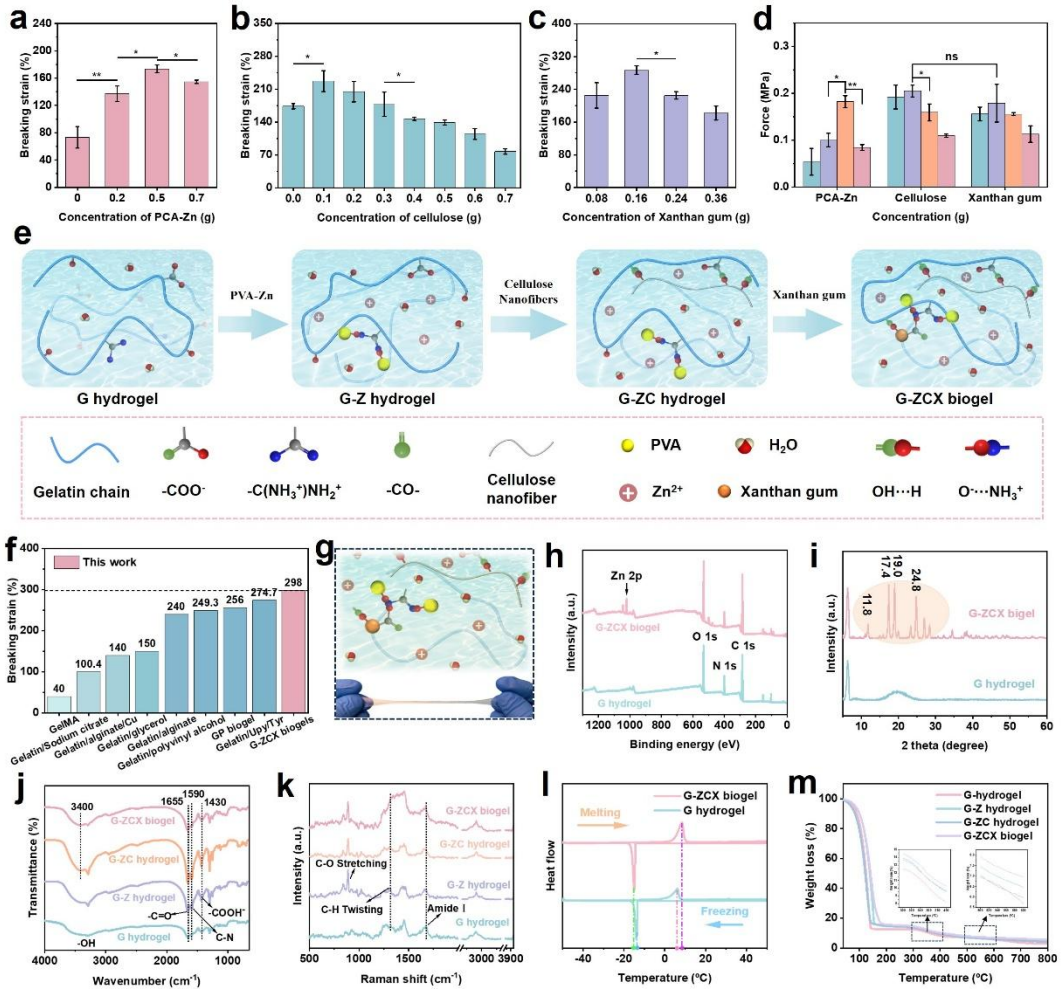

Figure 6.2 The performance of multifunctional G-ZCX biogels. a) The change of breaking strain with the increase in PCA-Zn, b) CNF, and c) XG. d) The change of breaking strength within different samples. e) The bonding mechanism for fabricating G-ZCX biogels. f) Comparison of the mechanical performance between the G-ZCX

biogels with gelatin-based hydrogels reported. g) Schematic diagram showing photographs of stretched G-ZCX biogels. h) XRD spectra, i) XPS spectra, j) FT-IR spectra, k) Raman spectra, l) DSC curves, and m) Thermal stability of gelatin hydrogel, G-Z hydrogel, G-ZC hydrogel, and G-ZCX biogel.

The bonding mechanism of the G-ZCX hydrogel is schematically illustrated (Figure 6.2e), demonstrating how various interactions among gelatin chains, PCA-Zn, CNFs, and XG establish a robust network. Initially, strong electrostatic interactions form between the carboxyl groups ($-COO^-$) in PCA-Zn and the amino groups ($-NH_3^+$) in gelatin, achieving ionic crosslinking. The pyrrolidone ring structure induces the gelatin chains from a disordered coiled state to an ordered conformation. The released Zn^{2+} ions act as a conductive medium within the hydrogel, facilitating enhanced ionic conductivity. Secondly, the abundant hydroxyl groups on the CNF surface establish hydrogen bonds with the carbonyl groups (C=O) in gelatin, enhancing the mechanical strength of the network and limiting chain slippage. Ultimately, the long-chain polysaccharide structure of XG creates physical entanglements inside the network, forming additional hydrogen bonds with the hydroxyl/amino groups, hence, enhancing network stability and energy dissipation (Figure 6.3).

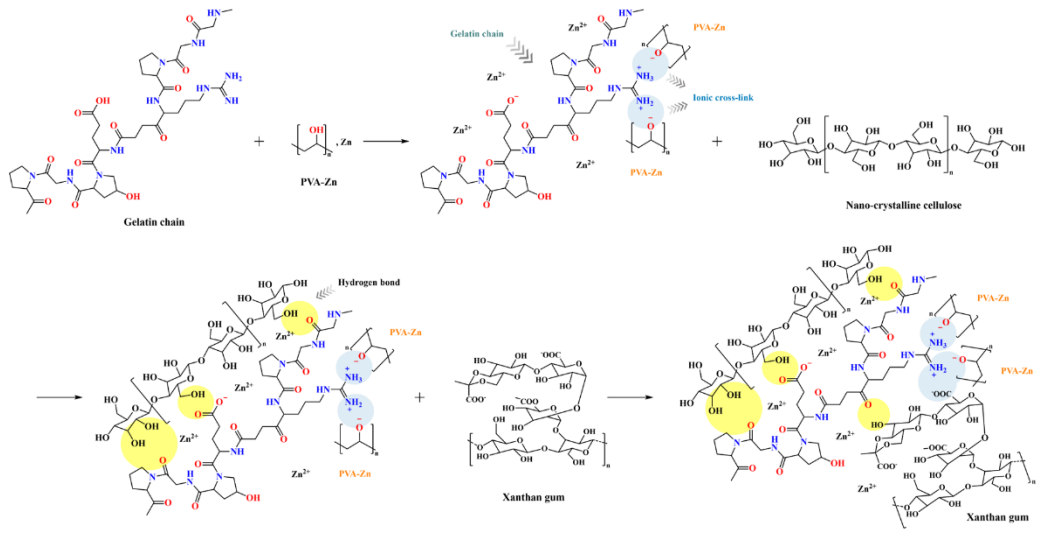

Figure 6.3 The bonding mechanism for fabricating G-ZCX biogels.

These effects synergistically construct a composite hydrogel network with high stretchability, excellent conductivity, and structural stability, establishing a basis for its multifunctional applications in wearable and implantable bioelectronic devices. The G-ZCX biogel displays superior elongation compared to other reported gelatin-based hydrogels to date (Figure 6.2f). The resultant G-ZCX biogel exhibited remarkable stretchability (Figure 6.2g). Upon stretching, the hydrogel network undergoes deformation, dynamically altering the distribution and migration of ions—changes that directly influence its mechanical behavior. As strain increases, Zn^{2+} ions migrate and reorganize along the oriented network, leading to local variations in ion concentration. This in turn modulates the electrostatic crosslinking density in a dynamic manner: regions enriched with ions exhibit strengthened crosslinks, which retard crack propagation, while the resistance encountered during ion migration further contributes to energy dissipation. Meanwhile, ion migration helps preserve conductive pathways within the network and offers an additional dissipation mechanism through the reformation of ionic bonds during chain slippage. The synergy of these ion-mediated processes enables the hydrogel to retain structural integrity via dynamic electrostatic crosslinking while dissipating energy through ion migration, even under high tensile strain. As shown in Figure 6.4, the fluid G-ZCX biogel spontaneously transforms into a gel state after being applied on the skin, and possesses mechanical strength and strong adhesion to the skin. These present extensive application opportunities for the forthcoming generation of wearable, high-performance bioelectronic devices in innovative domains such as tissue engineering, flexible electronics, and intelligent soft robotics.

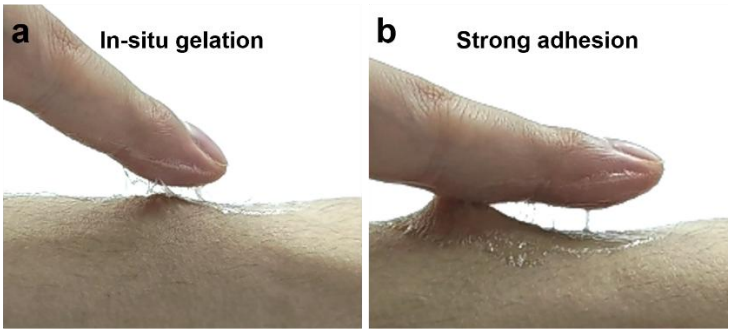

Figure 6.4 Photographs showing the a) on-skin painting capability of the G-ZCX biogel and b) its good adhesion with skin.

To investigate the interaction between gelatin and PCA-Zn, CNF, and XG in the G-ZCX biogel matrix, a series of characterizations were performed. XPS was first used to analyze the composition of the biogels. As shown in Figure 6.2h, G-ZCX biogel showed a characteristic peak of Zn compared to pure gelatin hydrogel. Figure 6.2i illustrates that the XRD pattern of the G-ZCX biogel exhibits a complete absence of the characteristic amorphous diffuse peak of gelatin ($2\theta \approx 20°$), indicating that the robust ionic crosslinking ($-NH_3^+\cdots^-OOC-$) of PCA-Zn organizes the disordered gelatin chains. The pronounced diffraction peaks of gelatin at low angles ($2\theta \approx 5°$) are preserved, signifying that the ionic crosslinking of PCA-Zn predominantly transpires in the amorphous area, hence preventing disruption of the intrinsically ordered gelatin template. Additionally, several novel groups of distinct diffraction peaks (e.g., 2θ = 11.8°/17.4°/19.0°/24.8°) signify the establishment of a Zn-mediated bio-organic framework (ZMOF) consisting of a ternary synergistic crystalline phase comprising PCA-Zn, CNF, and XG. Subsequently, FTIR and Raman spectroscopy were employed to further characterize the binding mechanism between gelatin and PCA-Na, CNF, and XG. Figure 6.2j illustrates a discernible trend emerged whereby with the incorporation of PCA-Zn resulted in an elevation of the intensities of characteristic peaks associated with gelatin at 1655 cm^{-1} (Amide I), 1590 cm^{-1} (Amide II), and the 1430 cm^{-1} ($-COO^-$

symmetrical stretching vibration). The increased intensities of the 1430 cm^{-1} and 1590 cm^{-1} peaks indicate that the addition of PCA-Zn initiates ionic bond-driven chemical crosslinking. Its carboxyl groups ($-COO^-$) form strong electrostatic bonds with amino groups ($-NH_3^+$) within gelatin, significantly enhancing the stability of biogel network[211]. In addition, the enhanced peak at 1655 cm^{-1} indicates that ionic crosslinking induces a conformational transition of gelatin from a disordered coil to an ordered conformation, alongside the incorporation of pyrrolidone rings inside PCA-Zn[212]. After the addition of CNFs, the peak at 1655 cm^{-1} was further enhanced, demonstrating the formation of hydrogen bonds between C=O in gelatin and O-H in cellulose. Furthermore, the incorporation of XG resulted in a notable broadening of the signal at 3400 cm^{-1}, signifying that XG facilitated the superposition of O-H and N-H, hence enhancing the hydrogen bond network. Raman spectroscopy further confirmed the interactions between gelatin and PCA-Zn, CNF, and XG (Figure 6.2k). The G-Z hydrogel exhibited distinct C–O stretching vibration peaks, ascribing to the increase in the number of carboxyl groups resulted from the incorporation of PCA-Zn. Moreover, the absorption peak of Amide I displayed a slight shift to lower wavenumbers[202], indicating that the ionic crosslinking between gelatin and PCA-Zn induced a conformational transition from a disordered coil to an ordered conformation of gelatin, as well as the formation of intermolecular interactions between gelatin and PCA-Zn. The shift in the C–H twisting signified robust electrostatic interactions between the -COO- of PCA-Zn and $-NH^{3+}$ of gelatin. The peaks exhibited minimal variation following the incorporation of CNFs. Furthermore, the addition of XG led to a splitting of the Amide I, indicating an enhanced hydrogen bonding network. Collectively, these findings confirm the interactions between gelatin and PCA-Zn, CNF, and XG, including hydrogen bonding and electrostatic attraction. Additionally, the water in the

G-ZCX biogel displayed differences in freezing and melting points relative to those in the gelatin hydrogel (Figure 6.2l). Water within the dense polymer matrix of the G-ZCX biogel froze at around -15.3°C and thawed at around 8.5°C, while water in the sparse polymer matrix of the gelatin hydrogel froze at approximately -13.7°C and thawed at about 6.0°C. Figure 6.2m illustrates the thermal stability of G hydrogel, G-Z hydrogel, G-ZC hydrogel, and G-ZCX biogel. The first weight loss appears at approximately 100°C, exceeding 80%, primarily attributable to the water evaporation within the hydrogel. Weight loss at approximately 350°C is attributed to the breakage of the polymer backbone. Moreover, compared to gelatin hydrogels, the others exhibited lower weight loss owing to improved thermal stability resulting from ionic crosslinking. At around 550°C, the mass exhibits negligible reduction owing to the oxidative degradation of the carbon framework. As the temperature was increased to 700 °C, the weight began to remain stable, and G-ZCX biogel showed the least weight loss due to the zinc compounds and the residues of XG carbonization products.

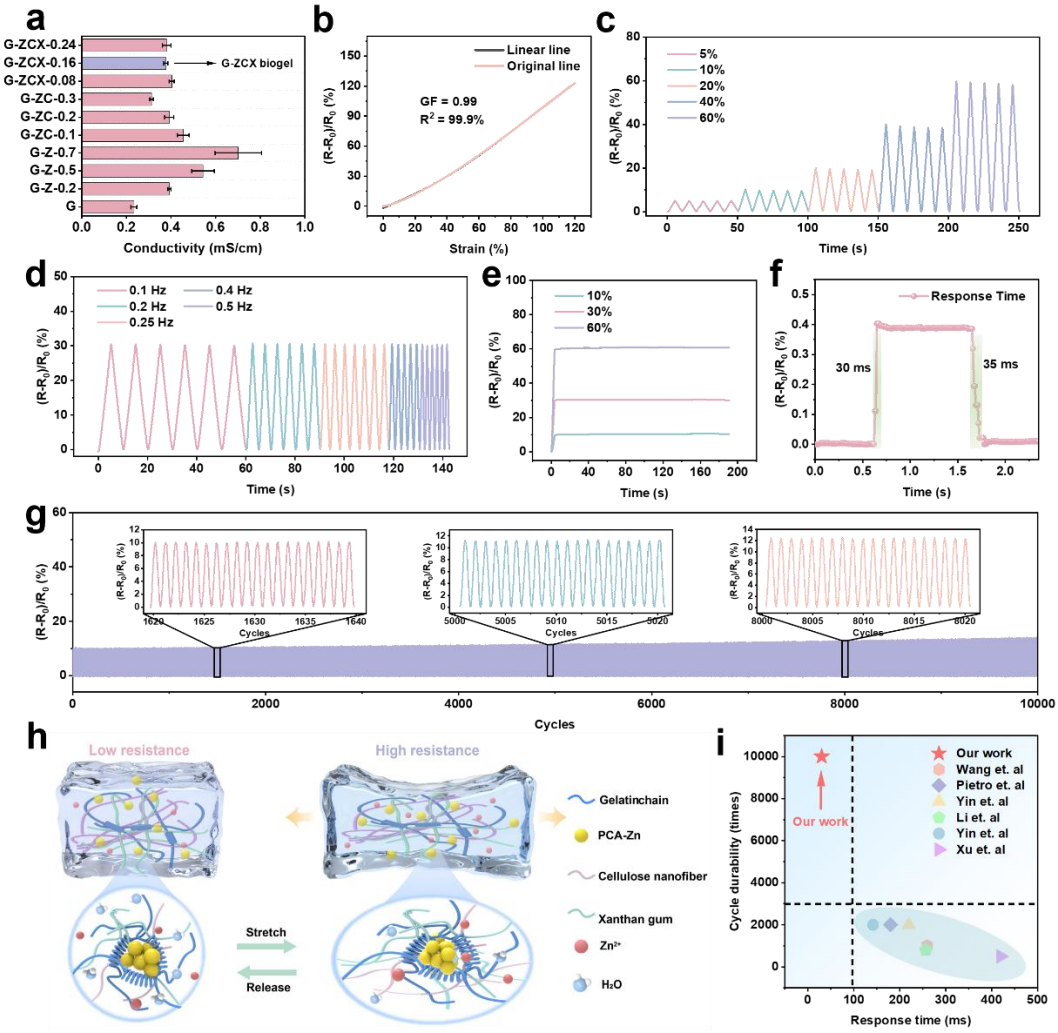

Figure 6.5 Sensing performance of the G-ZCX biogels. a) The conductivities of various hydrogel samples. b) Variations in relative resistance and gauge factor (GF) of the G-ZCX biogel. c) Relative resistance changes under different strain (5-60%). d) Electrical response to stretching-releasing strain at various frequencies (0.1-0.5Hz). e) The relative resistance changes at different strains for 3 mins. f) The response time of the G-ZCX biogel subjected to a fast-speed 0.5% strain. g) Cyclic durability of the G-ZCX biogel under a stretching-releasing strain of 10% for 10,000 cycles. h) Schematic illustration of the sensing mechanism. i) Comparison of the hysteresis and durability between the G-ZCX biogel with other previous works.

Various hydrogels with varying formulations were fabricated to assess the impact of PCA-Zn, CNF, and XG on the conductivity of the hydrogel. The comprehensive details of these formulations are presented in Table 6.1. Figure 6.5a shows the changes in the conductivity of the hydrogel at various phases. The incorporation of PCA-Zn introduces a substantial free ion (Zn^{2+}) into the hydrogel, hence enhancing the conductivity of the G-Z hydrogel. As the concentration of PCA-Zn increased, the conductivity of the G-Z hydrogel rose from 0.23 mS/cm to 0.70 mS/cm. The subsequent incorporation of CNFs obstructs ion migration pathways inside the hydrogel, leading to a reduction in conductivity. Upon the addition of 0.1 g of CNFs, the conductivity of hydrogel decreased to 0.40 mS/cm, then declining to 0.31 mS/cm with the incorporation of 0.3 g of CNFs. The incorporation of XG decreased the hydrogel conductivity to 0.38 mS/cm owing to the enhanced gel network that further impedes ion movement. 0.38 mS/cm.

Figure 6.5b illustrates the correlation between resistance change ($\Delta R/R_0$) and tensile strain. The hydrogel demonstrates great sensitivity and linearity during the stretching process, with a gauge factor (GF) of 0.99 that is calculated by $(\Delta R/R_0)/\varepsilon$ and a linearity of 99.9%. The high sensitivity facilitates the detection of small physiological signals and high-frequency signals; the exceptional linearity guarantees precise linear correlation of signals ($R^2 > 0.99$) and streamlined data processing. This illustrates the dependability of the G-ZCX biogel in sports rehabilitation, gesture recognition, and bioelectrical monitoring, establishing a data foundation for customized and personalized diagnosis and therapy. The dynamic repeatability of the G-ZCX biogels was evaluated by applying a cyclic stretch-release strain of 5–60% at a frequency of 0.1 Hz (Figure 6.5c) and a cyclic stretch-release strain of 30% in the frequency range of 0.1 to 0.5 Hz (Figure 6.5d). The biogel exhibited consistent and reliable resistive

responses, indicating the dynamic sensing stability and applicability of the hydrogel sensors for diverse strain-induced scenarios. The static strain stability of the hydrogel was evaluated under applied tensile strains of 10%, 30%, and 60% (Figure 6.5e). The G-ZCX biogel maintained stable electrical signals without overshoot or fluctuation, confirming excellent static stability for sensing applications. To quantify dynamic response time, we applied a step strain of 0.5% at 10 mm/s to the G-ZCX biogel (Figure 6.5f). The sensor demonstrated a rapid response time of 30 ms and recovery time of 35 ms, which are sufficient for epidermal strain sensing and physiological signal acquisition. Moreover, the sensor exhibited exceptional repeatability and consistent stability during 10,000 stretch-release cycles at 10% strain (Figure 6.5g), with the insets illustrating enlarged perspectives of the various stages of the cycle. A minor deviation was noted in the curves, attributable to the destruction of the hydrogel sensor network and moisture loss after prolonged stretching. The superior durability and stability of the G-ZCX biogel guarantee long-term motion monitoring and physiological electrical signal assessment. The sensing mechanism of G-ZCX biogels primarily involves polymer network deformation and water redistribution (Figure 6.5h). Under tensile strain, the hydrogel elongates and narrows, reducing its cross-sectional area and constricting conductive pathways. This geometry change increases electrical resistance (R) according to $R = \rho L/A$, where increased length (L) and decreased area (A) elevated R. Concurrently, the stretching process induces localized water migration, decreasing hydration in strained regions and concentrating mobile ions. This reduced hydration restricts ion mobility while simultaneously compressing ion channels through polymer network densification. Both phenomena synergistically enhance resistance. Compared with existing gelatin-based hydrogels, G-ZCX biogels have comprehensive advantages, including excellent stretchability, simple fabrication, cycling durability, fast response

time, and excellent biocompatibility (Figure 6.5i and Table 6.2).

Table 6.2 Performance comparison between gelatin-based hydrogels

Type	Fracture strain	Water retention ability	Conductivity	Fabrication time (h)	Fatigue resistance (cycles)	Response time (ms)	Biocompatibility	Refs
Gelatin/alginate	240%	No	Yes	4	1,000	260	No	[211]
Gelatin/alginate/Cu	140%	Yes	Yes	6	2,000	180	No	[213]
Gelatin/CNT/silk	90%	Yes	Yes	48	2,000	142	No	[214]
Gelatin/sodium citrate	100.4%	Yes	Yes	6	2,000	220	No	[215]
GP biogel	256%	Yes	Yes	2	No	-	No	[202]
Gelatin/glycerol	150%	Yes	No	2	No	500	No	[216]
Gelatin/$(NH_4)_2SO_4$	528%	No	No	14	No	-	No	[217]
GelMA	40%	No	No	40	No	-	Yes	[218]
Gelatin/CNF	250%	Yes	Yes	14	500	420	No	[219]
Gelatin/polyvinyl alcohol	249.3%	Yes	Yes	4	800	257	No	[220]
G-ZCX biogels	298%	Yes	Yes	2	10,000	30	Yes	This work

G-ZCX biogels have been advanced for use in medical rehabilitation and remote monitoring, encompassing the monitoring of body movement, identification of rehabilitation gestures, and acquisition of electrophysiological signals. Figure 6.6 illustrates the integration of hydrogels with wireless Bluetooth technology and software for the seamless and remote detection of subtle physical actions (such as respiration and speaking) and large deformations (such as joint movements). The G-ZCX biogel, when worn, detects the wearer's motions and produces real-time electrical output signals. The signals are then received and analyzed by the Bluetooth wireless device and transmitted to a smartphone for display. The signal of finger bending, elbow bending, breathing, speaking, walking, and running were rapidly and precisely captured of, highlighting the capabilities of G-ZCX biogels for wearable and real-time athletic training and remote observation.

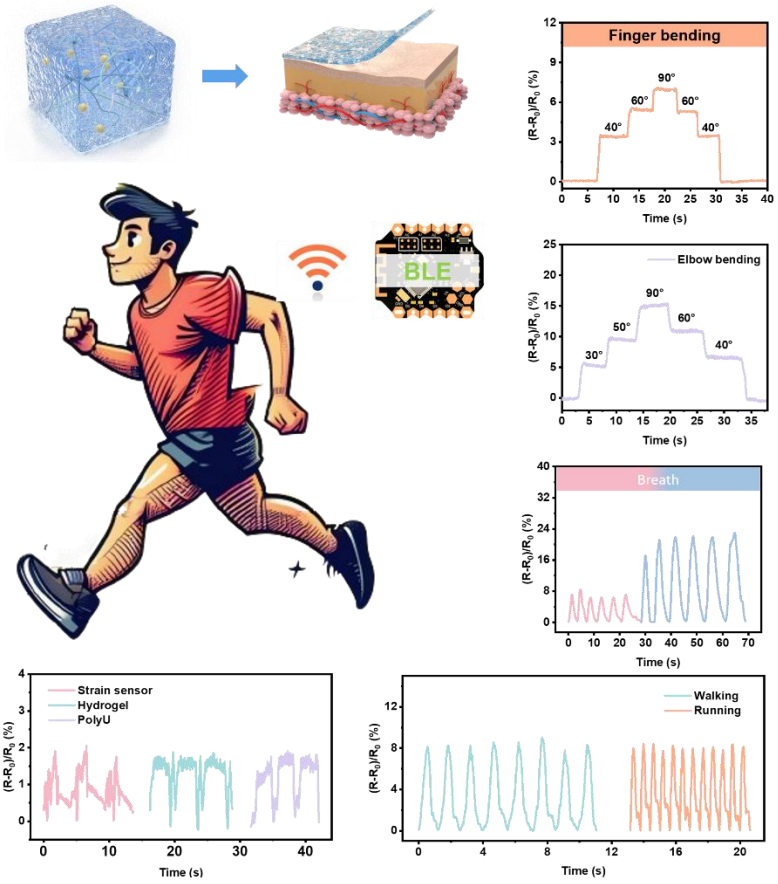

Figure 6.6 Application for monitoring full-range physical movements through Bluetooth device.

Recent advancements in machine learning, especially deep learning (DL), have made it a transformational instrument for analyzing nuanced physiological alterations and intricate signal patterns[221, 222]. Among several deep learning architectures, one-dimensional convolutional neural networks (1D-CNNs) are proficient at extracting hierarchical features from temporal data[223]. They generally comprise an input layer, a convolutional hidden layer, and a fully connected classifier. The integration of multi-channel hydrogel sensing technologies with 1D-CNNs has brought a paradigm shift in the objective and quantifiable monitoring of fine hand movements in physical rehabilitation. Biomechanics of finger motion—comprising individual finger bending,

multi-finger coordination, precision pinching, and item hold—are key biomarkers for neurorehabilitation. Using electrical signals captured from human finger motion using G-ZCX biogels, a wearable rehabilitation recognition system has been developed to accurately distinguish various human states (Figure 6.7a).

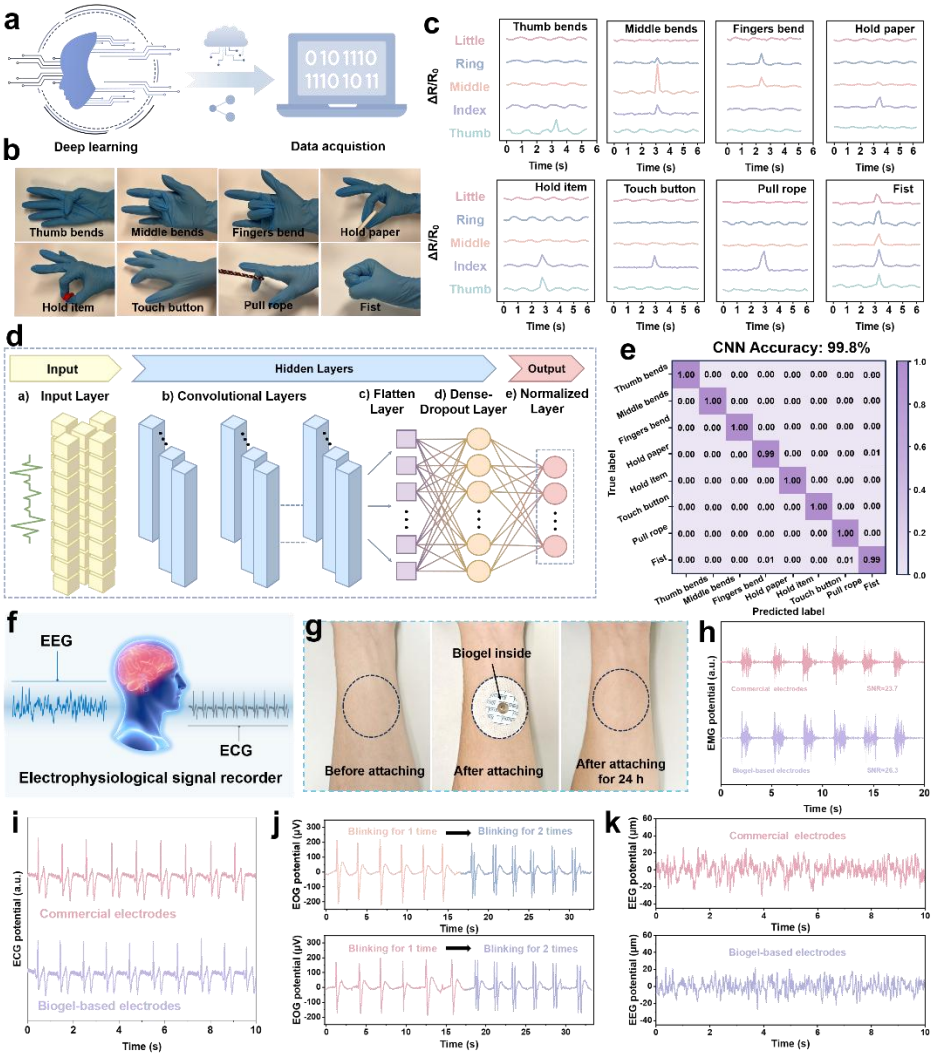

Figure 6.7 Gesture recognition system and electrophysiological signal recording platform. a) Schematic illustration of the gesture recognition system. b) Pictures of various hand gestures. c) Electrical data acquisition for the recognition of different hand gestures. d) Illustrations of the procedure for creating the 1D CNN structure. e) Confusion matrix on test set. f) Schematic illustration of the electrophysiological signal

recorder platform. g) Digital images showing the skin irritation results of G-ZCX biogels on the forearms of the volunteer. h) EMG, i) ECG, j) EOG, and k) EEG signals acquired by G-ZCX biogels-based electrode and commercial electrode.

Figure 6.7b presents pictures related to activities such as thumb finger bending, middle finger bending, middle and ring fingers bending, holding paper, holding item, touching button, pulling rope, and fist. Subsequently, electrical signals from the G-ZCX biogel were recorded, capturing over 120,000 data points for eight types of motion, each including over 60 cycles (Figure 6.7c). To facilitate data gathering, each motion was recorded for at least 300 s to compile a dataset. In this dataset, 80% was allocated for training, while the remaining 20% was reserved for testing. As shown in Figure 6.7d, a 1D-CNN motion recognition model was constructed to analyze the large amount of motion data. The network architecture comprises three convolutional layers: input, hidden, and output. Every convolutional layer is succeeded by a max pooling layer to diminish dimensionality and extract essential features from the input sequence data. Subsequent to the feature extraction phase, the model utilizes a fully connected layer to integrate these features and generate predictions for the eight kinds finger motion. The samples were standardized and divided into training and testing sets in an 80:20 ratio to create a detection model for G-ZCX biogels. This method guarantees a robust training foundation and effective assessment of model performance. The model achieved almost 99% accuracy and stabilized at epoch 12, showcasing its exceptional learning capability (Figure 6.8a). Figure 6.8b illustrates that the model's loss diminished with the increase in epochs, ultimately stabilizing at approximately 0%. The developed 1D-CNN model achieved an overall recognition accuracy of 99.8% for various finger actions (Figure 6.7e). The diagonal elements of the confusion matrix approached 1.0, indicating exceptionally high classification accuracy for each

movement category; the off-diagonal elements were close to zero, reflecting extremely low inter-category confusion. These results demonstrate the exceptional reliability and resolution of the flexible sensing-deep learning integrated system for multi-finger movement recognition, highlighting its extensive application potential in intelligent human-computer interaction, rehabilitation training monitoring, and virtual reality control.

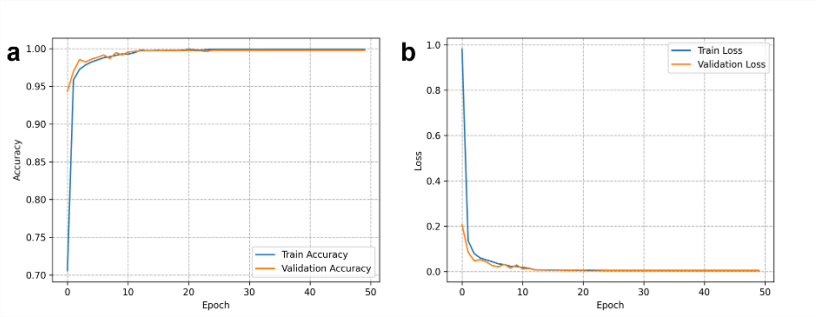

Figure 6.8 a) Training and validation accuracy during 50 training epochs. b) Training and validation loss during 50 training epochs.

An advanced bioelectronics technology platform was established to demonstrate the G-ZCX biogel's ability to monitor electrophysiological signals, including EMG, ECG, EOG, and EEG (Figure 6.7f). The bioelectrical signal platform includes a wireless signal recorder, electrodes, and a graphical user interface. The biogel, as the skin-electrode interface material, provides a stable, low-impedance contact environment that improves the sensitivity and reliability of signal acquisition. Before conducting electrophysiological signal monitoring tests, a skin allergy assessment was performed to evaluate the biocompatibility of the G-ZCX biogel with human skin. Such an assessment is essential for ensuring safety during daily wear and preventing damage to the skin. As shown in Figure 6.7g, the left image shows the skin condition before attaching, the middle image shows the condition after application of the biogel-based electrode, and the right image shows the condition after application for 24 h. The results

of the skin allergy test demonstrate that the G-ZCX biogel is non-toxic to the skin. The biogel electrode maintained good conformability and adhesion stability even after long-term wear, with no noticeable skin irritation. Subsequently, the EMG signals generated by muscle contraction were captured successfully by using the G-ZCX biogel (Figure 6.7h). A comparison is made between the EMG signal generated from a commercial electrode and a G-ZCX biogel-based electrode during the same muscle contractions. While both electrodes capture clear contraction-relaxation waveforms, the G-ZCX biogel electrode achieves a higher SNR (26.3 dB) and less baseline drift, demonstrating superior dynamic response stability. The G-ZCX biogel can also record ECG signals that is similar to those obtained using the commercial electrode (Figure 6.7i). The biogel electrode not only fully captures key features such as the P wave, QRS complex, and T wave, but also maintains low noise levels after long acquisition times (Figures 6.9a, b). These results indicate the long-term stability of the G-ZCX biogel in capturing high-quality ECG signals and its potential for accurate human electrophysiological monitoring.

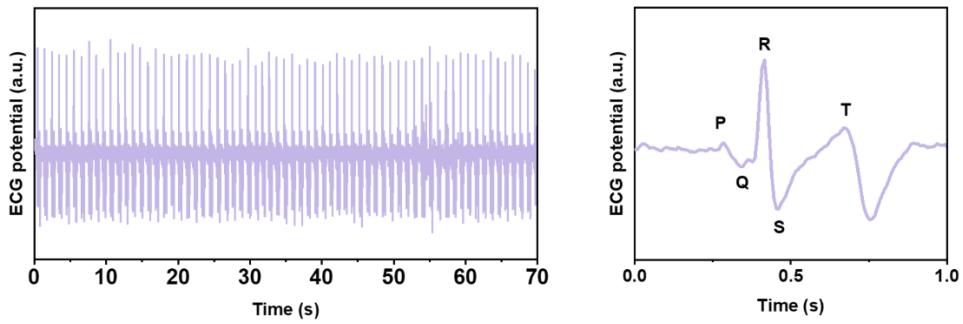

Figure 6.9 a) ECG signals recorded by biogel-based electrodes after 2 h continuous wearing. b) The zoomed-in data segments showing the characteristic PQRST waveforms.

Recording EOG and EEG signals presents greater challenges compared to ECG

and EMG owing to their weaker signals. As shown in Figure 6.7j, the upper figure shows the EOG signal recorded by a commercial electrode, and the lower figure shows the EOG signal recorded by a G-ZCX biogel-based electrode. When performing single and double blinks, the biogel electrode output high-amplitude eye movement signals with clear waveforms, demonstrating its ability to capture low-amplitude neural electrical signals. Furthermore, resting-state EEG signals were recorded (Figure 6.7k), exhibiting high-fidelity alpha rhythms during signal acquisition. The biogel electrode exhibited lower noise amplitude and more stable baseline levels, which improves the accuracy of signal analysis and feature extraction. These results demonstrate that the biogel electrode maintains good skin adhesion and biocompatibility even under prolonged wear. In addition, it demonstrates higher SNR, more stable baseline, and clearer waveform characteristics than commercial electrodes in acquiring multiple electrophysiological signals (EMG, ECG, EOG, and EEG), highlighting its potential for application in wearable bioelectronics and continuous health monitoring.

Implantable hydrogels are crucial in biointegrated electronics, intelligent medication delivery, biomedical engineering, and clinical medicine. To further evaluate the viability of G-ZCX biogels as implantable medical devices, we performed in vitro and in vivo biocompatibility assessments (Figure 6.10a). The cytocompatibility of the synthesized hydrogel was assessed by inoculating L929 cells onto its surface. Figures 6.10b and c indicate that cell viability remained around 104.6% (>100%) following 5 days of cultivation. Figure 6.10d illustrates the optical density (OD) values of the G-ZCX biogels and the control group, demonstrating a progressive increase in OD values over time.

To systematically evaluate the initial tissue reaction following G-ZCX biogel implantation, H&E staining of dorsal subcutaneous tissue was conducted on

postoperative days 3 and 14 (Figure 6.10e). The control group demonstrated preserved skin structure at both time points, characterized by orderly organization of the dermis and subcutaneous fat layers; however, modest hemorrhage and infiltration of inflammatory cells were observed in the incision region. In contrast, the material group demonstrated the formation of a continuous and complete fiber cyst wall around the implant by day 3. Active fibroblasts were distributed within the cyst wall, along with new capillaries and an approximate infiltrate of neutrophils and macrophages at the periphery, indicating an acute healing phase accompanied by active angiogenesis and matrix remodeling. By day 14, the cyst wall structure exhibited increased density and uniformity, accompanied by a notable reduction in inflammatory cells, maturation of interstitial cells, and a more stable vascular structure, indicating that the local tissue's progression from the acute inflammatory phase to a phase of tissue remodeling and stable integration. To observe extracellular matrix (ECM) remodeling, tissue sections from the same time period were stained with Masson's trichrome (Figure 6.10f). In the control group, only a small amount of collagen fiber deposition was visible at the edge of the injury on day 3; the fibers were delicate and sparse. By day 14, collagen content had increased, but the arrangement remained loose, indicating slow ECM remodeling. In the material group, continuous blue-stained collagen fibers appeared in the cyst wall region on day 3, distributed radially along the implant interface and accompanied by numerous active fibroblasts, indicating a significant initiation of collagen synthesis. By day 14, collagen fiber density had increased significantly, with larger bundles and more directional arrangement, indicating that collagen had transformed from its initial loose state to a mature, dense structure. This change indicates that the material enchances ECM deposition and structural maturation, promoting the formation of a stable tissue-material interface.

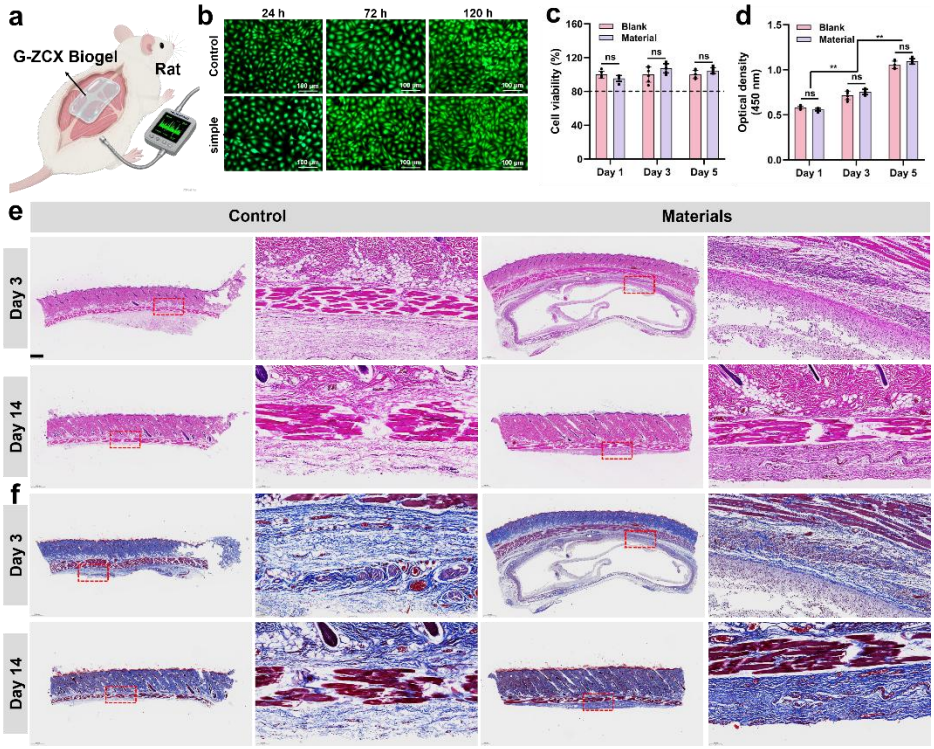

Figure 6.10 In vitro and in vivo biocompatibility of G-ZCX biogels. a) Schematic diagram of G-ZCX biogels inside rat. b) Fluorescent images of cells cultured in the incubation medium with the blank sample and G-ZCX biogels. c) Cell viability for the G-ZCX biogels and control after 1, 3, and 5 days of incubation. d) Absorption at 450 nm in MTT assay of the G-ZCX biogels and control after 1, 3 and 5 days of incubation. e) and f) Micrographs of G-ZCX biogels stained with H & E and Masson on days 3 and 14.

6.3 Summary

In summary, highly and compatiable gelatin-based biogels have been fabricated for multifunctional electronic applications such as body movement monitoring, gesture recognition, electrophysiological signal acquisition, and implantable applications. Ionic crosslinking and hydrogen bonding, which integrate gelatin with PCA-Zn, CNFs,

and XG, reconcile conflicting properties for bioelectronic interfaces. The hierarchical network achieves low modulus (<0.5 MPa), excellent stretchability (286.7%), and fatigue resistance (>10,000 cycles), minimizing mechanical mismatch with biological tissues. The biogel has a wide detection range and high linearity (99.9%), enabling full-body motion tracking, gesture recognition (99.8% accuracy via 1D-CNN), and high-fidelity electrophysiological monitoring (EMG, ECG, EOG, and EEG). In vivo and in vitro studies reveal excellent biocompatibility and implantable potential, with the inflammatory response disappearing after 14-day implantation. Unlike flexible and wearable electronics, G-ZCX biogels leverage natural components to enable simultaneous wearable-implantable functionality without environmental stability requirements or requiring secondary removal surgery. This work advances the design and platform of hydrogel materials for personalized rehabilitation, long-term neural monitoring, implantable medical electronic devices, and drug delivery.

Chapter 7. Conclusion and Suggestions for Future Research

7.1 Conclusion

This research study systematically investigates and develops sustainable photochromic wearable fabrics and multifunctional biocompatible electronic gels, establishing a comprehensive framework spanning material design, scalable fabrication, performance optimization, and application validation. The work provides innovative material platforms and versatile technical pathways for the fields of smart textiles and healthcare bioelectronics. The main findings and conclusions are summarized as follows:

First, a novel and scalable modification strategy for creating fiber-based photochromic wearables has been proposed and developed. By incorporating a MoO_3-based self-synthesized polymer network (MSPN) and long-chain silyl groups onto cotton fabrics, exceptional photochromic properties are imparted. The resultant MSPPT material demonstrates remarkable reversible color switching (pale yellow to blue) triggered by UV light or common disinfectants, characterized by outstanding fatigue resistance, rapid light response, and impressive color retention. This study successfully demonstrates the practical utility of MSPPT in flexible wearables, dynamic photo-patterning, and information encryption through writable/erasable patterns and QR code recognition. Crucially, the MSPN-based strategy establishes a broadly applicable paradigm for developing advanced fiber-based photochromic textiles.

Secondly, a scalable fabrication approach for photochromic fabrics has been developed by integrating sheath-core structured MM nanoparticles into polyester-cotton fabrics (PCFs) via covalent bonding, and combining them with SA through electrostatic interactions and peptide linkages. The resultant SAME-PCF exhibits

excellent reversible photochromism (pale yellow to blue) upon UV or $K_2S_2O_8$ exposure, featuring superior fatigue resistance, rapid response, and prolonged color retention. Practical demonstrations, including a fully rewritable T-shirt and a QR code-based encryption system, highlight the significant potential of SAME-PCFs in customizable patterning, flexible rewritable textiles, and information security applications.

Thirdly, highly compatible gelatin-based biogels (G-ZCX) have been designed for a wide range of multifunctional bioelectronic electronic applications, from wearable sensing to implantation. By integrating gelatin with PCA-Zn, CNFs, and XG through synergistic ionic crosslinking and hydrogen bonding, these biogels successfully reconcile the critical yet often conflicting demands of bioelectronic interfaces. The engineered hierarchical network structure endows the gels with a low modulus, outstanding stretchability, and excellent fatigue resistance, effectively minimizing mechanical mismatch with biological tissues. G-ZCX biogels exhibit a broad detection range and exceptional linearity, enabling applications such as full-body motion tracking, high-accuracy gesture recognition, and high-fidelity monitoring of diverse electrophysiological signals (EMG, ECG, EOG, EEG). Comprehensive in vitro and in vivo evaluations confirm its excellent biocompatibility and significant implant potential, with observed inflammatory responses resolving within 14 days. Unlike conventional flexible electronics, G-ZCX biogels leverage natural components to achieve dual wearable and implantable functionality without requiring stringent environmental stability or secondary removal surgeries. This study represents a significant advancement in hydrogel material design, paving the way for personalized rehabilitation, long-term neural monitoring, implantable medical devices, and advanced healthcare platforms.

7.2 Recommendations for Future Work

Building upon the foundations laid by this research, the following directions are proposed to further enhance the capabilities, applicability, and impact of photochromic textiles and biocompatible biogels.

7.2.1 Enhanced environmental stability and durability

The long-term stability of photochromic fabrics under real-world conditions (e.g., repeated washing, abrasion, prolonged UV exposure, varying humidity/temperature) requires a more systematic evaluation. Future works should focus on developing protective coatings or encapsulation strategies (e.g., atomic layer deposition of transparent oxides, self-healing polymer layers) to significantly improve wash fastness, abrasion resistance, and photochemical fatigue life. Similarly, the in vivo long-term stability, degradation profile, and functional longevity of the G-ZCX biogels under physiological conditions need deeper investigation over extended periods (months to years).

7.2.2 Multi-stimuli responsive systems and advanced functionalities

Expanding the responsiveness of the developed materials beyond light is crucial. Future research could integrate thermochromic, electrochromic, or humidity-responsive elements with the photochromic platforms to create fabrics that respond intelligently to multiple environmental cues. For the biogels, incorporating stimuli-responsive components (e.g., pH-sensitive polymers for drug release, conductive polymers for on-demand stiffness modulation) could enable smart therapeutic functions and adaptive interfaces. Exploring self-healing capabilities for both material systems would further enhance durability and lifespan.

7.2.3 Towards closed-loop digital health systems

The true potential of digital health systems lies in integrating sensing (biogels) and responsive feedback (e.g., photochromic displays, drug release) into intelligent, closed-loop systems. Future work should focus on seamlessly combining the G-ZCX biogel sensors with the photochromic textile actuators (or other output modalities like microfluidic drug delivery) on a single flexible/textile platform. Developing efficient signal processing circuits, energy harvesting/storage elements specifically compatible with these soft materials, and wireless communication modules is essential for creating autonomous, wearable/implantable digital health monitors and therapeutic devices.

7.2.4 Scalability, sustainability, and biocompatibility optimization

Scaling up the fabrication processes for both photochromic fabrics and biocompatible biogels while ensuring batch-to-batch consistency and performance uniformity is vital for translation. Research into continuous manufacturing techniques (e.g., roll-to-roll coating for fabrics, microfluidic synthesis for gels) is recommended. Concurrently, the sustainability footprint should be minimized by prioritizing bio-based or recycled feedstocks, aqueous processing, and designing for end-of-life recyclability or biodegradability where appropriate. For implantable biogels, deeper investigations into immune response modulation, long-term biointegration, and potential systemic effects are necessary.

7.2.5 Personalization and AI-driven design/optimization

Leveraging artificial intelligence (AI) and machine learning (ML) holds immense promise. Future work could develop predictive models to optimize material formulations (e.g., gel composition for target mechanical/electrical properties, dye/polymer ratios for specific color kinetics) and fabrication parameters, accelerating

design and experimental cycles. AI algorithms could also analyze complex sensor data streams from biogels for early disease detection, personalized activity recognition, or adaptive therapy control. Furthermore, exploring digital printing or additive manufacturing techniques could enable the personalization of photochromic patterns and biogel device geometries for individual users or specific clinical applications.

References

[1] Bao B, Bai S, Fan J, Su J, Wang W, Yu D. A novel and durable photochromic cotton-based fabric prepared via thiol-ene click chemistry. Dyes Pigm. 2019, 171: 107778.

[2] Ermes M, Pärkkä J, Mäntyjärvi J, Korhonen I. Detection of daily activities and sports with wearable sensors in controlled and uncontrolled conditions. IEEE Trans. Inf. Technol. Biomed. 2008, 12: 20-26.

[3] Petriashvili G, De Santo M P, Devadze L, Zurabishvili T, Sepashvili N, Gary R, Barberi R. Rewritable optical storage with a spiropyran doped liquid crystal polymer film. Macromol. Rapid Commun. 2016, 37: 500-505.

[4] Shallcross R C, Körner P O, Maibach E, Köhnen A, Meerholz K. A photochromic diode with a continuum of intermediate states: towards high density multilevel storage. Adv. Mater. 2013, 25: 4807-4813.

[5] Qiao Y, Che Y, Yu Y, Tang Y, Liu L, Zhao X, Zhao J. Solid-state photochromic properties, mechanism and electrospun membranes of (E)-2-(benzo [b] thiophen-2-ylmethylene)-N-ethylhydrazine-1-carbothioamide. Dyes Pigm. 2018, 156: 326-331.

[6] Irie M, Fukaminato T, Matsuda K, Kobatake S. Photochromism of diarylethene molecules and crystals: memories, switches, and actuators. Chem. Rev. 2014, 114: 12174-12277.

[7] Li Z, Wang Y, Li M, Chen H, Xie Y, Li P, Guo H, Ya H. Solvent-dependent and visible light-activated NIR photochromic dithienylethene modified by difluoroboron β-diketonates as fluorescent turn-on pH sensor. Dyes Pigm. 2019, 162: 339-347.

[8] Zheng C, Pu S, Liu G, Chen B, Dai Y. A highly selective colorimetric sensor for cysteine and homocysteine based on a new photochromic diarylethene. Dyes Pigm.

2013, 98: 280-285.

[9] Yoon B, Lee J, Park I S, Jeon S, Lee J, Kim J-M. Recent functional material based approaches to prevent and detect counterfeiting. J. Mater. Chem. C. 2013, 1: 2388-2403.

[10] Zhong W, Zeng X, Chen J, Hong Y, Xiao L, Zhang P. Photoswitchable fluorescent polymeric nanoparticles for rewritable fluorescence patterning and intracellular dual-color imaging with AIE-based fluorogens as FRET donors. Polym. Chem. 2017, 8: 4849-4855.

[11] Hrabovská V, Hricová M, Ujhelyiová A. Application of photochromic pigment in mass dyed polypropylene fibres intended for intelligent textiles. Acta Chimica Slovaca. 2019, 12: 82-90.

[12] Zhang Y, Xia X, Ma K, Xia G, Wu M, Cheung Y H, Yu H, Zou B, Zhang X, Farha O K. Functional textiles with smart properties: their fabrications and sustainable applications. Adv. Funct. Mater. 2023, 33: 2301607.

[13] Gao W, Ota H, Kiriya D, Takei K, Javey A. Flexible electronics toward wearable sensing. Acc. Chem. Res. 2019, 52: 523-533.

[14] Ray T R, Choi J, Bandodkar A J, Krishnan S, Gutruf P, Tian L, Ghaffari R, Rogers J A. Bio-integrated wearable systems: a comprehensive review. Chem. Rev. 2019, 119: 5461-5533.

[15] Chen T, Yang Q, Fang C, Deng S, Xu B. Advanced Design for Stimuli-Reversible Chromic Wearables With Customizable Functionalities. Adv. Mater. 2025, 37: 2413665.

[16] Yang Y, Gao W. Wearable and flexible electronics for continuous molecular monitoring. Chem. Soc. Rev. 2019, 48: 1465-1491.

[17] Ling Y, An T, Yap L W, Zhu B, Gong S, Cheng W. Disruptive, soft, wearable sensors. Adv. Mater. 2020, 32: 1904664.

[18] Brown G H. Photochromism. Techniques of Chemistry. 1971, 853.

[19] Photochromic O, Compounds T. JC Crano and RJ Guglielmetti. Plenum Press, New York. 1999, 1: 85.

[20] Pardo R, Zayat M, Levy D. Photochromic organic–inorganic hybrid materials. Chem. Soc. Rev. 2011, 40: 672-687.

[21] Washington I, Brooks C, Turro N J, Nakanishi K. Porphyrins as photosensitizers to enhance night vision. J. Am. Chem. Soc. 2004, 126: 9892-9893.

[22] Kayani A B A, Kuriakose S, Monshipouri M, Khalid F A, Walia S, Sriram S, Bhaskaran M. UV photochromism in transition metal oxides and hybrid materials. Small. 2021, 17: 2100621.

[23] Chernyshev A V, Voloshin N A, Rostovtseva I A, Solov'eva E V, Gaeva E B, Metelitsa A V. Polychromogenic molecular systems based on photo-and ionochromic spiropyrans. Dyes Pigm. 2018, 158: 506-516.

[24] Inaba K, Iwai R, Morimoto M, Irie M. Thermally reversible photochromism of dipyrrolylethenes. Photochemical & Photobiological Sciences. 2019, 18: 2136-2141.

[25] Barachevsky V. Advances in photonics of organic photochromism. J. Photochem. Photobiol., A. 2018, 354: 61-69.

[26] Kozlenko A S, Ozhogin I V, Pugachev A D, Lukyanova M B, El-Sewify I M, Lukyanov B S. A modern look at spiropyrans: From single molecules to smart materials. Top. Curr. Chem. 2023, 381: 8.

[27] Pang M L, Nie Y T, Wang Y M, Meng J B, Wang J T. Synthesis of New Spiropyrans With a Polyaromatic or Heteroaromatic Pendant and Their Photochromic Behaviors. Chin. J. Chem. 2002, 20: 1102-1108.

[28] Klajn R. Spiropyran-based dynamic materials. Chem. Soc. Rev. 2014, 43: 148-184.

[29] Kortekaas L, Browne W R. The evolution of spiropyran: fundamentals and

progress of an extraordinarily versatile photochrome. Chem. Soc. Rev. 2019, 48: 3406-3424.

[30] Yuan J, Yuan Y, Tian X, Wang H, Liu Y, Feng R. Photoswitchable boronic acid derived salicylidenehydrazone enabled by photochromic spirooxazine and fulgide moieties: Multiple responses of optical absorption, fluorescence emission, and quadratic nonlinear optics. J. Phys. Chem. C. 2019, 123: 29838-29855.

[31] Yokoyama Y. Fulgides for memories and switches. Chem. Rev. 2000, 100: 1717-1740.

[32] Tian H, Yang S. Recent progresses on diarylethene based photochromic switches. Chem. Soc. Rev. 2004, 33: 85-97.

[33] Lin S, Gutierrez-Cuevas K G, Zhang X, Guo J, Li Q. Fluorescent photochromic α-cyanodiarylethene molecular switches: an emerging and promising class of functional diarylethene. Adv. Funct. Mater. 2021, 31: 2007957.

[34] Jerca F A, Jerca V V, Hoogenboom R. Advances and opportunities in the exciting world of azobenzenes. Nat. Rev. Chem. 2022, 6: 51-69.

[35] Becker R S, Michl J. Photochromism of synthetic and naturally occurring 2H-chromenes and 2H-pyrans. J. Am. Chem. Soc. 1966, 88: 5931-5933.

[36] Linsley C S, Wu B M. Recent advances in light-responsive on-demand drug-delivery systems. Therapeutic delivery. 2017, 8: 89-107.

[37] Sallenave X, Delbaere S, Vermeersch G, Saleh A, Pozzo J-L. Photoswitch based on remarkably simple naphthopyrans. Tetrahedron Lett. 2005, 46: 3257-3259.

[38] Zheng T, Xu Z, Zhao Y, Li H, Jian R, Lu C. Multiresponsive polysiloxane bearing photochromic spirobenzopyran for sensing pH changes and Fe^{3+} ions and sequential sensing of Ag^{+} and Hg^{2+} ions. Sens. Actuators, B. 2018, 255: 3305-3315.

[39] Fan F, Zhang W, Wang C. Covalent bonding and photochromic properties of

double-shell polyurethane-chitosan microcapsules crosslinked onto cotton fabric. Cellulose. 2015, 22: 1427-1438.

[40] Samoylova E, Dallari W, Allione M, Pignatelli F, Marini L, Cingolani R, Diaspro A, Athanassiou A. Characterization of fatigue resistance in photochromic composite materials for 3D rewritable optical memory applications. Mater. Sci. Eng., B. 2013, 178: 730-735.

[41] Yu A, Tolbert C A, Farrow D A, Jonas D M. Solvatochromism and solvation dynamics of structurally related cyanine dyes. J. Phys. Chem. A. 2002, 106: 9407-9419.

[42] Sun C, Xu G, Jiang X-M, Wang G-E, Guo P-Y, Wang M-S, Guo G-C. Design strategy for improving optical and electrical properties and stability of lead-halide semiconductors. J. Am. Chem. Soc. 2018, 140: 2805-2811.

[43] Shree S, Schulz-Senft M, Alsleben N H, Mishra Y K, Staubitz A, Adelung R. Light, force, and heat: a multi-stimuli composite that reveals its violent past. ACS Appl. Mater. Interfaces. 2017, 9: 38000-38007.

[44] Prabhu S, Cindrella L, Kwon O J, Mohanraju K. Photoelectrochemical, photocatalytic and photochromic performance of rGO-TiO_2WO_3 composites. Mater. Chem. Phys. 2019, 224: 217-228.

[45] Rawat M, Mal S, Singh P. Photochromism in Anils-A Review. Open Chemistry Journal. 2015, 2: 7-9.

[46] Pan L, Wang Y, Wang X, Qu H, Zhao J, Li Y, Gavrilyuk A. Hydrogen photochromism in Nb_2O_5 powders. PCCP. 2014, 16: 20828-20833.

[47] Kawahara K, Suzuki K, Ohko Y, Tatsuma T. Electron transport in silver-semiconductor nanocomposite films exhibiting multicolor photochromism. PCCP. 2005, 7: 3851-3855.

[48] Tobaldi D, Hortigüela Gallo M, Otero-Irurueta G, Singh M, Pullar R, Seabra M,

Labrincha J. Purely visible-light-induced photochromism in Ag–TiO_2 nanoheterostructures. Langmuir. 2017, 33: 4890-4902.

[49] He T, Yao J. Photochromism in composite and hybrid materials based on transition-metal oxides and polyoxometalates. Prog. Mater Sci. 2006, 51: 810-879.

[50] Bechinger C, Wirth E, Leiderer P. Photochromic coloration of WO_3 with visible light. Appl. Phys. Lett. 1996, 68: 2834-2836.

[51] Bechinger C, Oefinger G, Herminghaus S, Leiderer P. On the fundamental role of oxygen for the photochromic effect of WO_3. J. Appl. Phys. 1993, 74: 4527-4533.

[52] González-Borrero P, Sato F, Medina A, Baesso M L, Bento A C, Baldissera G, Persson C, Niklasson G A, Granqvist C G, Ferreira da Silva A. Optical band-gap determination of nanostructured WO_3 film. Appl. Phys. Lett. 2010, 96: 061909.

[53] Gavrilyuk A. Photochromism in WO_3 thin films. Electrochim. Acta. 1999, 44: 3027-3037.

[54] He Y, Wu Z, Fu L, Li C, Miao Y, Cao L, Fan H, Zou B. Photochromism and size effect of WO_3 and WO_3-TiO_2 aqueous sol. Chem. Mater. 2003, 15: 4039-4045.

[55] Kim H Y, Yoo T-H, Hwang Y, Lee G H, Kim B, Jang J, Yu H T, Kim M C, Cho J-Y, Lee C J. Indoxyl sulfate (IS)-mediated immune dysfunction provokes endothelial damage in patients with end-stage renal disease (ESRD). Sci. Rep. 2017, 7: 3057.

[56] Prasad A R, Anagha M, Shamsheera K, Joseph A. Bio-fabricated ZnO nanoparticles: Direct sunlight-driven selective photodegradation, antibacterial activity, and thermoluminescence-emission characteristics. New J. Chem. 2020, 44: 8273-8279.

[57] Mclaren A, Valdes-Solis T, Li G, Tsang S C. Shape and size effects of ZnO nanocrystals on photocatalytic activity. J. Am. Chem. Soc. 2009, 131: 12540-12541.

[58] Kołodziejczak-Radzimska A, Jesionowski T. Zinc oxide—from synthesis to application: a review. Materials. 2014, 7: 2833-2881.

[59] Matsuda K, Irie M. Diarylethene as a photoswitching unit. J. Photochem. Photobiol., C. 2004, 5: 169-182.

[60] Beharry A A, Woolley G A. Azobenzene photoswitches for biomolecules. Chem. Soc. Rev. 2011, 40: 4422-4437.

[61] Seefeldt B, Kasper R, Beining M, Mattay J, Arden-Jacob J, Kemnitzer N, Drexhage K H, Heilemann M, Sauer M. Spiropyrans as molecular optical switches. Photochemical & Photobiological Sciences. 2010, 9: 213-220.

[62] Lee K M, Lai C W, Ngai K S, Juan J C. Recent developments of zinc oxide based photocatalyst in water treatment technology: a review. Water Res. 2016, 88: 428-448.

[63] Tang H, Prasad K, Sanjines R, Schmid P, Levy F. Electrical and optical properties of TiO_2 anatase thin films. J. Appl. Phys. 1994, 75: 2042-2047.

[64] Tandy L M F, Bueno J P, Vong Y M, Torres I Z, Rojas L L, Torres C J R, Gutiérrez H M, López M M. Reversible photochromic effect in the TiO_2—polymer hybrid system. J. Sol-Gel Sci. Technol. 2017, 82: 51-58.

[65] Nishio S, Kakihana M. Evidence for visible light photochromism of V_2O_5. Chem. Mater. 2002, 14: 3730-3733.

[66] Greenwood N N, Earnshaw A, Chemistry of the Elements, Elsevier2012.

[67] Jittiarporn P, Sikong L, Kooptarnond K, Taweepreda W. Effects of precipitation temperature on the photochromic properties of h-MoO_3. Ceram. Int. 2014, 40: 13487-13495.

[68] He T, Yao J. Photochromism of molybdenum oxide. J. Photochem. Photobiol., C. 2003, 4: 125-143.

[69] Wang M, Koski K J. Reversible chemochromic MoO_3 nanoribbons through zerovalent metal intercalation. ACS Nano. 2015, 9: 3226-3233.

[70] Miyata N, Suzuki T, Ohyama R. Physical properties of evaporated molybdenum

oxide films. Thin Solid Films. 1996, 281: 218-222.

[71] Shen Y, Huang R, Cao Y, Wang P. Synthesis and photochromic properties of formaldehyde-induced MoO_3 powder. Mater. Sci. Eng., B. 2010, 172: 237-241.

[72] Zhao H, Cun Y, Bai X, Xiao D, Qiu J, Song Z, Liao J, Yang Z. Entirely reversible photochromic glass with high coloration and luminescence contrast for 3D optical storage. ACS Energy Lett. 2022, 7: 2060-2069.

[73] Fan J, Bao B, Wang Z, Li H, Wang Y, Chen Y, Wang W, Yu D. Flexible, switchable and wearable image storage device based on light responsive textiles. Chem. Eng. J. 2021, 404: 126488.

[74] Li H, Zhao G, Zhu M, Guo J, Wang C. Robust large-sized photochromic photonic crystal film for smart decoration and anti-counterfeiting. ACS Appl. Mater. Interfaces. 2022, 14: 14618-14629.

[75] Heo J, Kim Y B, Kim D S. Versatile camouflage coating of photochromic pigments. Mol. Cryst. Liq. Cryst. 2022, 739: 104-110.

[76] Mahbubul Bashar M, Khan M A. An overview on surface modification of cotton fiber for apparel use. J. Polym. Environ. 2013, 21: 181-190.

[77] Huang L, Lin S, Xu Z, Zhou H, Duan J, Hu B, Zhou J. Fiber-based energy conversion devices for human-body energy harvesting. Adv. Mater. 2020, 32: 1902034.

[78] Wang D, Zhang Y, Lu X, Ma Z, Xie C, Zheng Z. Chemical formation of soft metal electrodes for flexible and wearable electronics. Chem. Soc. Rev. 2018, 47: 4611-4641.

[79] Sun H, Zhang Y, Zhang J, Sun X, Peng H. Energy harvesting and storage in 1D devices. Nat. Rev. Mater. 2017, 2: 1-12.

[80] Zhang X, Lin H, Shang H, Xu J, Zhu J, Huang W. Recent advances in functional fiber electronics. SusMat. 2021, 1: 105-126.

[81] Gao Y, Zhang J, Su Y, Wang H, Wang X-X, Huang L-P, Yu M, Ramakrishna S,

Long Y-Z. Recent progress and challenges in solution blow spinning. Mater. Horiz. 2021, 8: 426-446.

[82] Yan W, Dong C, Xiang Y, Jiang S, Leber A, Loke G, Xu W, Hou C, Zhou S, Chen M. Thermally drawn advanced functional fibers: New frontier of flexible electronics. Mater. Today. 2020, 35: 168-194.

[83] Rahaman M, Aldalbahi A, Bhagabati P. Preparation/processing of polymer–carbon composites by different techniques. Carbon-Containing Polymer Composites. 2019, 99-124.

[84] Aboutalebi S H, Jalili R, Esrafilzadeh D, Salari M, Gholamvand Z, Aminorroaya Yamini S, Konstantinov K, Shepherd R L, Chen J, Moulton S E. High-performance multifunctional graphene yarns: toward wearable all-carbon energy storage textiles. ACS Nano. 2014, 8: 2456-2466.

[85] He H, Yang C, Wang F, Wei Z, Shen J, Chen D, Fan C, Zhang H, Liu K. Mechanically strong globular-protein-based fibers obtained using a microfluidic spinning technique. Angew. Chem. Int. Ed. 2020, 59: 4344-4348.

[86] Wang Z, Wu T, Wang Z, Zhang T, Chen M, Zhang J, Liu L, Qi M, Zhang Q, Yang J. Designer patterned functional fibers via direct imprinting in thermal drawing. Nat. Commun. 2020, 11: 3842.

[87] Ho D H, Han J, Huang J, Choi Y Y, Cheon S, Sun J, Lei Y, Park G S, Wang Z L, Sun Q. β-Phase-Preferential blow-spun fabrics for wearable triboelectric nanogenerators and textile interactive interface. Nano Energy. 2020, 77: 105262.

[88] Liao M, Wang C, Hong Y, Zhang Y, Cheng X, Sun H, Huang X, Ye L, Wu J, Shi X. Industrial scale production of fibre batteries by a solution-extrusion method. Nat. Nanotechnol. 2022, 17: 372-377.

[89] Zheng Y, Panatdasirisuk W, Liu J, Tong A, Xiang Y, Yang S. Patterned, wearable

UV indicators from electrospun photochromic fibers and yarns. Adv. Mater. Technol. 2020, 5: 2000564.

[90] Wei J, Jiao X, Wang T, Chen D. Electrospun photochromic hybrid membranes for flexible rewritable media. ACS Appl. Mater. Interfaces. 2016, 8: 29713-29720.

[91] El-Newehy M H, Aldalbahi A, Thamer B M, Abdulhameed M M. Electrospinning of photochromic poly (ethylene terephthalate) nanofibers toward information authentication. Luminescence. 39: e4626.

[92] Wang Y, Xi P, Shu D, Meng S, Liu K, Wang X, Cheng B. Preparation and Properties of Electrospun Sheath-core Modified-PMMA Nanofibers with Photoluminescence and Photochromic Functions. Chem. Res. Chin. Univ. 2021, 37: 549-557.

[93] Wang B, Peng J, Yang K, Cheng H, Yin Y, Wang C. Multifunctional textile electronic with sensing, energy storing, and electrothermal heating capabilities. ACS Appl. Mater. Interfaces. 2022, 14: 22497-22509.

[94] Xiong J, Lin M F, Wang J, Gaw S L, Parida K, Lee P S. Wearable all-fabric-based triboelectric generator for water energy harvesting. Adv. Energy Mater. 2017, 7: 1701243.

[95] Bae H, Kim D, Seo M, Jin I K, Jeon S B, Lee H M, Jung S H, Jang B C, Son G, Yu K. Bioinspired polydopamine-based resistive-switching memory on cotton fabric for wearable neuromorphic device applications. Adv. Mater. Technol. 2019, 4: 1900151.

[96] Gao C, Zhang Y, Jiang B, Xi R, Zhu K, Wang Y, Xu W, Song D. Construction of durable and original color constancy photochromic cotton fabrics by a facile esterification strategy. Ind. Crops Prod. 2022, 189: 115783.

[97] Fan J, Bao B, Wang Z, Xu R, Wang W, Yu D. High tri-stimulus response photochromic cotton fabrics based on spiropyran dye by thiol-ene click chemistry.

Cellulose. 2020, 27: 493-510.

[98] He Z, Bao B, Fan J, Wang W, Yu D. Photochromic cotton fabric based on microcapsule technology with anti-fouling properties. Colloids Surf., A. 2020, 594: 124661.

[99] He Z, Wang W, Fan J, Bao B, Qin X, Yu D. Photochromic microcapsules anchored on cotton fabric by layer-by-layer self-assembly method with erasable property. React. Funct. Polym. 2020, 157: 104762.

[100] Qi Y, Fan J, Chang Y, Li Y, Bao B, Yan B, Li H, Cong P. Smart photochromic fabric prepared via thiol-ene click chemistry for image information storage applications. Dyes Pigm. 2021, 193: 109507.

[101] Bao B, Fan J, Wang Z, Wang Y, Wang W, Qin X, Yu D. Sodium deca-tungstate/polyacrylic acid self-assembled flexible wearable photochromic composite fabric for solar UV detector. Compos Part B-Eng. 2020, 202: 108464.

[102] Liu X, Miao J, Fan Q, Zhang W, Zuo X, Tian M, Zhu S, Zhang X, Qu L. Recent progress on smart fiber and textile based wearable strain sensors: materials, fabrications and applications. Adv. Fiber Mater. 2022, 4: 361-389.

[103] Yamada T, Hayamizu Y, Yamamoto Y, Yomogida Y, Izadi-Najafabadi A, Futaba D N, Hata K. A stretchable carbon nanotube strain sensor for human-motion detection. Nat. Nanotechnol. 2011, 6: 296-301.

[104] Cima M J. Next-generation wearable electronics. Nat. Biotechnol. 2014, 32: 642-643.

[105] Han S T, Peng H, Sun Q, Venkatesh S, Chung K S, Lau S C, Zhou Y, Roy V. An overview of the development of flexible sensors. Adv. Mater. 2017, 29: 1700375.

[106] Zhang Y, Fu J, Ding Y, Babar A A, Song X, Chen F, Yu X, Zheng Z. Thermal and Moisture Managing E-Textiles Enabled by Janus Hierarchical Gradient Honeycombs.

Adv. Mater. 2023, 2311633.

[107] Abramson A, Chan C T, Khan Y, Mermin-Bunnell A, Matsuhisa N, Fong R, Shad R, Hiesinger W, Mallick P, Gambhir S S. A flexible electronic strain sensor for the real-time monitoring of tumor regression. Sci. Adv. 2022, 8: eabn6550.

[108] Tan C, Dong Z, Li Y, Zhao H, Huang X, Zhou Z, Jiang J-W, Long Y-Z, Jiang P, Zhang T-Y. A high performance wearable strain sensor with advanced thermal management for motion monitoring. Nat. Commun. 2020, 11: 3530.

[109] Ma Y, Zhang Y, Cai S, Han Z, Liu X, Wang F, Cao Y, Wang Z, Li H, Chen Y. Flexible hybrid electronics for digital healthcare. Adv. Mater. 2020, 32: 1902062.

[110] Meng K, Xiao X, Wei W, Chen G, Nashalian A, Shen S, Xiao X, Chen J. Wearable pressure sensors for pulse wave monitoring. Adv. Mater. 2022, 34: 2109357.

[111] Kaisti M, Panula T, Leppänen J, Punkkinen R, Jafari Tadi M, Vasankari T, Jaakkola S, Kiviniemi T, Airaksinen J, Kostiainen P. Clinical assessment of a non-invasive wearable MEMS pressure sensor array for monitoring of arterial pulse waveform, heart rate and detection of atrial fibrillation. npj Digital Med. 2019, 2: 39.

[112] Boutry C M, Kaizawa Y, Schroeder B C, Chortos A, Legrand A, Wang Z, Chang J, Fox P, Bao Z. A stretchable and biodegradable strain and pressure sensor for orthopaedic application. Nat. Electron. 2018, 1: 314-321.

[113] Yin R, Wang D, Zhao S, Lou Z, Shen G. Wearable sensors-enabled human–machine interaction systems: from design to application. Adv. Funct. Mater. 2021, 31: 2008936.

[114] Xiong J, Chen J, Lee P S. Functional fibers and fabrics for soft robotics, wearables, and human–robot interface. Adv. Mater. 2021, 33: 2002640.

[115] Sun T, Jiang Y, Duan Z, Yuan Z, Wang Y, Tai H. Wearable and washable textile-based strain sensors via a single-step, environment-friendly method. Sci. China Technol.

Sci. 2021, 64: 441-450.

[116] Yu A, Zhu M, Chen C, Li Y, Cui H, Liu S, Zhao Q. Implantable flexible sensors for health monitoring. Adv. Healthcare Mater. 2024, 13: 2302460.

[117] Jiang W, Li H, Liu Z, Li Z, Tian J, Shi B, Zou Y, Ouyang H, Zhao C, Zhao L. Fully bioabsorbable natural-materials-based triboelectric nanogenerators. Adv. Mater. 2018, 30: 1801895.

[118] Ashammakhi N, Hernandez A L, Unluturk B D, Quintero S A, de Barros N R, Hoque Apu E, Bin Shams A, Ostrovidov S, Li J, Contag C. Biodegradable implantable sensors: materials design, fabrication, and applications. Adv. Funct. Mater. 2021, 31: 2104149.

[119] Herbert R, Lim H R, Park S, Kim J H, Yeo W H. Recent advances in printing technologies of nanomaterials for implantable wireless systems in health monitoring and diagnosis. Adv. Healthcare Mater. 2021, 10: 2100158.

[120] Chen W, Zheng X, Zhou Y, Du W, Liang F, Yu H D, Li L. Recent Progress in Semi-Implantable Bioelectronics for Precision Health Monitoring. Adv. Funct. Mater. 2025, 2424463.

[121] Lee H K, Yang Y J, Koirala G R, Oh S, Kim T-i. From lab to wearables: Innovations in multifunctional hydrogel chemistry for next-generation bioelectronic devices. Biomaterials. 2024, 122632.

[122] Zhang M, Xu T, Liu K, Zhu L, Miao C, Chen T, Gao M, Wang J, Si C. Modulation and Mechanisms of Cellulose-Based Hydrogels for Flexible Sensors. SusMat. 2025, 5: e255.

[123] Chen Z, Xu C, Chen X, Huang J, Guo Z. Advances in electrically conductive hydrogels: performance and applications. Small Methods. 2025, 9: 2401156.

[124] Imani K B C, Dodda J M, Yoon J, Torres F G, Imran A B, Deen G R, Al-Ansari

R. Seamless integration of conducting hydrogels in daily life: from preparation to wearable application. Adv. Sci. 2024, 11: 2306784.

[125] Zeb M, Qu Z, Li P, Liang D, Zhu J, Yang E, Yeom B, Peng C, Guo F, Zhao Y. Crafting the Biomimetic Hydrogel for Wearable Biosensors. Small. 2025, 21: 2501910.

[126] He Q, Cheng Y, Deng Y, Wen F, Lai Y, Li H. Conductive hydrogel for flexible bioelectronic device: current progress and future perspective. Adv. Funct. Mater. 2024, 34: 2308974.

[127] Roy A, Afshari R, Jain S, Zheng Y, Lin M-H, Zenkar S, Yin J, Chen J, Peppas N A, Annabi N. Advances in conducting nanocomposite hydrogels for wearable biomonitoring. Chem. Soc. Rev. 2025,

[128] Li Z, Lu J, Ji T, Xue Y, Zhao L, Zhao K, Jia B, Wang B, Wang J, Zhang S. Self-healing hydrogel bioelectronics. Adv. Mater. 2024, 36: 2306350.

[129] Xiao K, Wan C, Jiang L, Chen X, Antonietti M. Bioinspired ionic sensory systems: the successor of electronics. Adv. Mater. 2020, 32: 2000218.

[130] Yao X, Zhang S, Qian L, Wei N, Nica V, Coseri S, Han F. Super stretchable, self-healing, adhesive ionic conductive hydrogels based on tailor-made ionic liquid for high-performance strain sensors. Adv. Funct. Mater. 2022, 32: 2204565.

[131] Duan J, Wen H, Zong S, Li T, Lv H, Liu L. Soft/hard controllable conversion galactomannan ionic conductive hydrogel as a flexible sensor. ACS Appl. Electron. Mater. 2021, 3: 5000-5014.

[132] Huang Y, Xiao L, Zhou J, Liu T, Yan Y, Long S, Li X. Strong tough polyampholyte hydrogels via the synergistic effect of ionic and metal–ligand bonds. Adv. Funct. Mater. 2021, 31: 2103917.

[133] Li W, Li L, Zheng S, Liu Z, Zou X, Sun Z, Guo J, Yan F. Recyclable, healable, and tough ionogels insensitive to crack propagation. Adv. Mater. 2022, 34: 2203049.

[134] Matsuda T, Kawakami R, Namba R, Nakajima T, Gong J P. Mechanoresponsive self-growing hydrogels inspired by muscle training. Science. 2019, 363: 504-508.

[135] Che L, Lei Z, Wu P, Song D. A 3D printable and bioactive hydrogel scaffold to treat traumatic brain injury. Adv. Funct. Mater. 2019, 29: 1904450.

[136] Hu Y, Zhuo H, Zhang Y, Lai H, Yi J, Chen Z, Peng X, Wang X, Liu C, Sun R. Graphene oxide encapsulating liquid metal to toughen hydrogel. Adv. Funct. Mater. 2021, 31: 2106761.

[137] Lin Z, Barbara D, Taberna P-L, Van Aken K L, Anasori B, Gogotsi Y, Simon P. Capacitance of $Ti_3C_2T_x$ MXene in ionic liquid electrolyte. J. Power Sources. 2016, 326: 575-579.

[138] Lu B, Yuk H, Lin S, Jian N, Qu K, Xu J, Zhao X. Pure pedot: Pss hydrogels. Nat. Commun. 2019, 10: 1043.

[139] Ohm Y, Pan C, Ford M J, Huang X, Liao J, Majidi C. An electrically conductive silver–polyacrylamide–alginate hydrogel composite for soft electronics. Nat. Electron. 2021, 4: 185-192.

[140] Liang Q, Xia X, Sun X, Yu D, Huang X, Han G, Mugo S M, Chen W, Zhang Q. Highly stretchable hydrogels as wearable and implantable sensors for recording physiological and brain neural signals. Adv. Sci. 2022, 9: 2201059.

[141] Shen Z, Zhu X, Majidi C, Gu G. Cutaneous ionogel mechanoreceptors for soft machines, physiological sensing, and amputee prostheses. Adv. Mater. 2021, 33: 2102069.

[142] Lee Y W, Chun S, Son D, Hu X, Schneider M, Sitti M. A tissue adhesion-controllable and biocompatible small-scale hydrogel adhesive robot. Adv. Mater. 2022, 34: 2109325.

[143] Zhang C, Hsieh M-H, Wu S-Y, Li S-H, Wu J, Liu S-M, Wei H-J, Weisel R D,

Sung H-W, Li R-K. A self-doping conductive polymer hydrogel that can restore electrical impulse propagation at myocardial infarct to prevent cardiac arrhythmia and preserve ventricular function. Biomaterials. 2020, 231: 119672.

[144] Yao S, Zhao X, Wang X, Huang T, Ding Y, Zhang J, Zhang Z, Wang Z L, Li L. Bioinspired electron polarization of nanozymes with a human self-generated electric field for cancer catalytic therapy. Adv. Mater. 2022, 34: 2109568.

[145] Yang S, Macharia D K, Ahmed S, Zhu B, Zhong Q, Wang H, Chen Z. Flexible and reusable non-woven fabric photodetector based on polypyrrole/crystal violate lactone for NIR light detection and writing. Adv. Fiber Mater. 2020, 2: 150-160.

[146] Wang Z, Bo Y, Bai P, Zhang S, Li G, Wan X, Liu Y, Ma R, Chen Y. Self-sustaining personal all-day thermoregulatory clothing using only sunlight. Science. 2023, 382: 1291-1296.

[147] Lee G S, Kim J G, Kim J T, Lee C W, Cha S, Choi G B, Lim J, Padmajan Sasikala S, Kim S O. 2D materials beyond post-AI era: smart fibers, soft robotics, and single atom catalysts. Adv. Mater. 2024, 36: 2307689.

[148] Zhang J, Liu J, Zhao Z, Sun W, Zhao G, Liu J, Xu J, Li Y, Liu Z, Li Y. Calotropis gigantea fiber-based sensitivity-tunable strain sensors with insensitive response to wearable microclimate changes. Adv. Fiber Mater. 2023, 5: 1378-1391.

[149] Lu J, Xu B, Huang J, Liu X, Fu H. Charge transfer and Ion occupation induced ultra-durable and all-weather energy generation from ambient air for over 200 days. Adv. Funct. Mater. 2024, 34: 2406901.

[150] Zhang J, Xu B, Chen K, Li Y, Li G, Liu Z. Revolutionizing digital healthcare networks with wearable strain sensors using sustainable fibers. SusMat. 2024, e207.

[151] Kundu P K, Samanta D, Leizrowice R, Margulis B, Zhao H, Börner M, Udayabhaskararao T, Manna D, Klajn R. Light-controlled self-assembly of non-

photoresponsive nanoparticles. Nat. Chem. 2015, 7: 646-652.

[152] Chen T, Xu B, Han J, Zhu M, Zhang J, Li Z. Chelating coordination regulated photochromic electrospun nanofibers for waterproof and long-color-retention rewritable wearables. ACS Appl. Mater. Interfaces. 2024, 16: 13305-13315.

[153] Kuroiwa H, Inagaki Y, Mutoh K, Abe J. On-demand control of the photochromic properties of naphthopyrans. Adv. Mater. 2019, 31: 1805661.

[154] Pardo R, Zayat M, Levy D. Photochromic organic-inorganic hybrid materials. Chem. Soc. Rev. 2011, 40: 672-687.

[155] Zhao J, Liu L, Zhang Y, Feng Z, Zhao F, Wang W. Light-responsive color switching of self-doped TiO_2−x/WO_3·0.33H_2O hetero-nanoparticles for highly efficient rewritable paper. Nano Res. 2021, 14: 165-171.

[156] Li J, Liu Y, Gu Z, Sun P, Liu K, Xu D, Gao C, Xu W. Scalable, green, flexible photochromic bacterial cellulose for multicolor switching, photo-patterning, and daily sunlight UV monitoring. Small. 2024, 20: 2309514.

[157] Zhu M, Xu B, Chen T, Zhang J, Sun W. Advanced Functional Photochromic Wearables with Superior Durability and Stability for Sustainable Applications. Adv. Funct. Mater. 2024, 2406840.

[158] Yimyai T, Crespy D, Pena-Francesch A. Self-healing photochromic elastomer composites for wearable UV-sensors. Adv. Funct. Mater. 2023, 33: 2213717.

[159] Wang M-S, Xu G, Zhang Z-J, Guo G-C. Inorganic-organic hybrid photochromic materials. Chem. Commun. 2010, 46: 361-376.

[160] Macharia D K, Sarker S, Zhu B, Zhang Y, Liu Z, Yu N, Chen Z. Constructing on-demand photoreversible mono/multi-color switching fabrics with plasmonic in-doped ZnO catalyzed systems. Chem. Eng. J. 2021, 425: 130638.

[161] Chen T, Xu B, Zhu M, Zhang J, Sun W, Han J. Advanced functional

photochromic wearables with fast photo-responsivity, long color-retention, and multi-environmental stability. Chem. Eng. J. 2024, 490: 151804.

[162] Yang M, Han Q, Liu X, Han J, Zhao Y, He L, Gou J, Wu Z, Wang X, Wang J. Ultrahigh stability 3D TI Bi_2Se_3/MoO_3 thin film heterojunction infrared photodetector at optical communication waveband. Adv. Funct. Mater. 2020, 30: 1909659.

[163] Saji V S, Lee C W. Molybdenum, molybdenum oxides, and their electrochemistry. ChemSusChem. 2012, 5: 1146-1161.

[164] De Castro I A, Datta R S, Ou J Z, Castellanos-Gomez A, Sriram S, Daeneke T, Kalantar-zadeh K. Molybdenum oxides-from fundamentals to functionality. Adv. Mater. 2017, 29: 1701619.

[165] Liu J, Shao S, Fang G, Meng B, Xie Z, Wang L. High-efficiency inverted polymer solar cells with transparent and work-function tunable MoO_3-Al composite film as cathode buffer layer. Adv. Mater. 2012, 24: 2774-2779.

[166] Kanno H, Holmes R J, Sun Y, Kena-Cohen S, Forrest S R. White stacked electrophosphorescent organic light-emitting devices employing MoO_3 as a charge-generation layer. Adv. Mater. 2006, 18: 339-342.

[167] Devan R S, Patil R A, Lin J H, Ma Y R. One-dimensional metal-oxide nanostructures: recent developments in synthesis, characterization, and applications. Adv. Funct. Mater. 2012, 22: 3326-3370.

[168] Dixit D, Ramachandran B, Chitra M, Madhuri K, Mangamma G. Photochromic response of the PLD-grown nanostructured MoO_3 thin films. Appl. Surf. Sci. 2021, 553: 149580.

[169] Duan J, Álvarez-Pérez G, Lanza C, Voronin K, Tresguerres-Mata A I, Capote-Robayna N, Álvarez-Cuervo J, Tarazaga Martin-Luengo A, Martín-Sánchez J, Volkov V S. Multiple and spectrally robust photonic magic angles in reconfigurable α-MoO3

trilayers. Nat. Mater. 2023, 22: 867-872.

[170] Zhou Z, Wang Y, Peng F, Meng F, Zha J, Ma L, Du Y, Peng N, Ma L, Zhang Q. Intercalation-activated layered MoO3 nanobelts as biodegradable nanozymes for tumor-specific photo-enhanced catalytic therapy. Angewandte Chemie. 2022, 134: e202115939.

[171] Zhang J Y, Liang J, Mei B, Lan K, Zu L, Zhao T, Ma Y, Chen Y, Lv Z, Yang Y. Synthesis of Ni/NiO@ MoO_{3-x} composite nanoarrays for high current density hydrogen evolution reaction. Adv. Energy Mater. 2022, 12: 2200001.

[172] Xu L, Zhou W, Chao S, Liang Y, Zhao X, Liu C, Xu J. Advanced oxygen-vacancy Ce-doped MoO3 ultrathin nanoflakes anode materials used as asymmetric supercapacitors with ultrahigh energy density. Adv. Energy Mater. 2022, 12: 2200101.

[173] Wang L, Zhang F, Liu Y, Leng J. Shape memory polymer fibers: materials, structures, and applications. Adv. Fiber Mater. 2022, 4: 5-23.

[174] Yan M, Shen Y, Zhao L, Li Z. Synthesis and photochromic properties of EDTA-induced MoO_3 powder. Mater. Res. Bull. 2011, 46: 1648-1653.

[175] Lupan O, Trofim V, Cretu V, Stamov I, Syrbu N, Tiginyanu I, Mishra Y K, Adelung R. Investigation of optical properties and electronic transitions in bulk and nano-microribbons of molybdenum trioxide. J. Phys. D: Appl. Phys. 2014, 47: 085302.

[176] Deng Y, Wei G-D, Nan C-W. Ligand-assisted control growth of chainlike nanocrystals. Chem. Phys. Lett. 2003, 368: 639-643.

[177] Wang Q, Sun G, Tong Q, Yang W, Hao W. Fluorine-free superhydrophobic coatings from polydimethylsiloxane for sustainable chemical engineering: Preparation methods and applications. Chem. Eng. J. 2021, 426: 130829.

[178] Sam E K, Sam D K, Lv X, Liu B, Xiao X, Gong S, Yu W, Chen J, Liu J. Recent development in the fabrication of self-healing superhydrophobic surfaces. Chem. Eng.

J. 2019, 373: 531-546.

[179] Abd El-Ghaffar M, Sherif M, El-Habab A T. Novel high solid content nano siliconated poly (VeoVa-acrylate) terpolymer latex for high performance latex paints. Chem. Eng. J. 2016, 301: 285-298.

[180] Xu L, Wang L, Shen Y, Ding Y, Cai Z. Preparation of hexadecyltrimethoxysilane-modified silica nanocomposite hydrosol and superhydrophobic cotton coating. Fibers Polym. 2015, 16: 1082-1091.

[181] Campos-Martin J M, Blanco-Brieva G, Fierro J L. Hydrogen peroxide synthesis: an outlook beyond the anthraquinone process. Angew. Chem. Int. Ed. 2006, 45: 6962-6984.

[182] Khan M F, Yu L, Hollman J, Tay J H, Achari G. Integration of aerobic granulation and UV/H 2 O 2 processes in a continuous flow system for the degradation of sulfolane in contaminated water. Environ. Sci. Water Res. Technol. 2020, 6: 1711-1722.

[183] Oszajca M, Brindell M, Orzeł Ł, Dąbrowski J M, Śpiewak K, Łabuz P, Pacia M, Stochel-Gaudyn A, Macyk W, van Eldik R. Mechanistic studies on versatile metal-assisted hydrogen peroxide activation processes for biomedical and environmental incentives. Coord. Chem. Rev. 2016, 327: 143-165.

[184] Papaconstantinou E. Photochemistry of polyoxometallates of molybdenum and tungsten and/or vanadium. Chem. Soc. Rev. 1989, 18: 1-31.

[185] Ding N, Hu N, Zhang J, Xu H, Meng L, Cai X, Müller-Buschbaum P, Qi D, Zhong Q. Reversible and photochromic peony-shaped hairpin prepared from electrospun hybrid nanofibers for visualized solar UV radiation detector. ACS Appl. Nano Mater. 2024, 7: 8140-8150.

[186] Lawrynowicz A, Vuori S, Palo E, Winther M, Lastusaari M, Miettunen K. Transforming fabrics into UV-sensing wearables: A photochromic hackmanite coating

for repeatable detection. Chem. Eng. J. 2024, 494: 153069.

[187] Lu J, Fu H, Tian X, Chen Y, Xu B. Advanced Design of Organic Ionic Materials for the Boost of Electricity Generation, Storage, and Utilization. Adv. Energy Mater. 2024, 14: 2402130.

[188] Qian J, Dong Q, Chun K, Zhu D, Zhang X, Mao Y, Culver J N, Tai S, German J R, Dean D P. Highly stable, antiviral, antibacterial cotton textiles via molecular engineering. Nat. Nanotechnol. 2023, 18: 168-176.

[189] Ahmed T, Gao Y, So M Y, Tan D, Lu J, Zhang J, Wang Q, Liu X, Xu B. Diamond-Structured Fabric-Based Triboelectric Nanogenerators for Energy Harvesting and Healthcare Application. Adv. Funct. Mater. 2024, 34: 2408680.

[190] Zhang J, Chen T, Zhu M, Lu J, Liu X, Sun W, So M Y, Xu B. Scalable, Fast Light-Responsive, and Excellent Color-Retention Fiber-Based Photochromic Wearables for Sustainable Photo-Patterning and Information Security Encryption. Adv. Funct. Mater. 2024, 2415622.

[191] Zhang J, Zou Q, Tian H. Photochromic materials: more than meets the eye. Adv. Mater. 2013, 25: 378-399.

[192] Xi G, Sheng L, Du J, Zhang J, Li M, Wang H, Ma Y, Zhang S X-A. Water assisted biomimetic synergistic process and its application in water-jet rewritable paper. Nat. Commun. 2018, 9: 4819.

[193] Liu P, Wang B, Wang C, Ma L, Zhang W, Hopmann E, Liu L, Elezzabi A Y, Li H. Amorphous Tungsten Oxide Nanodots for Chromatic Applications. Adv. Funct. Mater. 2024, 34: 2400760.

[194] Kawata S, Kawata Y. Three-dimensional optical data storage using photochromic materials. Chem. Rev. 2000, 100: 1777-1788.

[195] Qin B, Chen H, Liang H, Fu L, Liu X, Qiu X, Liu S, Song R, Tang Z. Reversible

photoswitchable fluorescence in thin films of inorganic nanoparticle and polyoxometalate assemblies. J. Am. Chem. Soc. 2010, 132: 2886-2888.

[196] El Kadib A. Chitosan as a sustainable organocatalyst: a concise overview. ChemSusChem. 2015, 8: 217-244.

[197] Amiri H, Aghbashlo M, Sharma M, Gaffey J, Manning L, Moosavi Basri S M, Kennedy J F, Gupta V K, Tabatabaei M. Chitin and chitosan derived from crustacean waste valorization streams can support food systems and the UN Sustainable Development Goals. Nat. Food. 2022, 3: 822-828.

[198] Mura S, Nicolas J, Couvreur P. Stimuli-responsive nanocarriers for drug delivery. Nat. Mater. 2013, 12: 991-1003.

[199] Miao Y B, Lin Y J, Chen K H, Luo P K, Chuang S H, Yu Y T, Tai H M, Chen C T, Lin K J, Sung H W. Engineering nano-and microparticles as oral delivery vehicles to promote intestinal lymphatic drug transport. Adv. Mater. 2021, 33: 2104139.

[200] Ma Z, Yang Z, Gao Q, Bao G, Valiei A, Yang F, Huo R, Wang C, Song G, Ma D. Bioinspired tough gel sheath for robust and versatile surface functionalization. Sci. Adv. 2021, 7: eabc3012.

[201] Li T, Qi H, Dong X, Li G, Zhai W. Highly robust conductive organo-hydrogels with powerful sensing capabilities under large mechanical stress. Adv. Mater. 2024, 36: 2304145.

[202] Lan L, Ping J, Li H, Wang C, Li G, Song J, Ying Y. Skin-inspired all-natural biogel for bioadhesive interface. Adv. Mater. 2024, 36: 2401151.

[203] Jiang Y, Ji S, Sun J, Huang J, Li Y, Zou G, Salim T, Wang C, Li W, Jin H. A universal interface for plug-and-play assembly of stretchable devices. Nature. 2023, 614: 456-462.

[204] Chong J, Sung C, Nam K S, Kang T, Kim H, Lee H, Park H, Park S, Kang J.

Highly conductive tissue-like hydrogel interface through template-directed assembly. Nat. Commun. 2023, 14: 2206.

[205] Zheng M, Wang X, Yue O, Hou M, Zhang H, Beyer S, Blocki A M, Wang Q, Gong G, Liu X. Skin-inspired gelatin-based flexible bio-electronic hydrogel for wound healing promotion and motion sensing. Biomaterials. 2021, 276: 121026.

[206] Park B, Shin J H, Ok J, Park S, Jung W, Jeong C, Choy S, Jo Y J, Kim T-i. Cuticular pad–inspired selective frequency damper for nearly dynamic noise–free bioelectronics. Science. 2022, 376: 624-629.

[207] Baumgartner M, Hartmann F, Drack M, Preninger D, Wirthl D, Gerstmayr R, Lehner L, Mao G, Pruckner R, Demchyshyn S. Resilient yet entirely degradable gelatin-based biogels for soft robots and electronics. Nat. Mater. 2020, 19: 1102-1109.

[208] Sun X, Mao Y, Yu Z, Yang P, Jiang F. A biomimetic “salting out—alignment—locking” tactic to design strong and tough hydrogel. Adv. Mater. 2024, 36: 2400084.

[209] Klemm D, Heublein B, Fink H P, Bohn A. Cellulose: fascinating biopolymer and sustainable raw material. Angew. Chem. Int. Ed. 2005, 44: 3358-3393.

[210] Kong W, Wang C, Jia C, Kuang Y, Pastel G, Chen C, Chen G, He S, Huang H, Zhang J. Muscle-inspired highly anisotropic, strong, ion-conductive hydrogels. Adv. Mater. 2018, 30: 1801934.

[211] Wang L, Zhang H J, Liu X, Liu Y, Zhu X, Liu X, You X. A physically cross-linked sodium alginate–gelatin hydrogel with high mechanical strength. ACS Appl. Polym. Mater. 2021, 3: 3197-3205.

[212] Dai H, Li X, Du J, Ma L, Yu Y, Zhou H, Guo T, Zhang Y. Effect of interaction between sorbitol and gelatin on gelatin properties and its mechanism under different citric acid concentrations. Food Hydrocolloids. 2020, 101: 105557.

[213] Tordi P, Tamayo A, Jeong Y, Bonini M, Samorì P. Multiresponsive ionic

conductive alginate/gelatin organohydrogels with tunable functions. Adv. Funct. Mater. 2024, 34: 2410663.

[214] Yin R, Zhang C, Shao J, Chen Y, Yin A, Feng Q, Chen S, Peng F, Ma X, Xu C-Y. Integration of flexible, recyclable, and transient gelatin hydrogels toward multifunctional electronics. Journal of Materials Science & Technology. 2023, 145: 83-92.

[215] Yin R, Zhang C, Chen Y, Wang Y, Feng Q, Liu Y, Yu M, Yuan Y, Xu C-Y, Liu F. Transient, printable and recyclable gelatin hydrogels with enhanced mechanical sensing and electromagnetic shielding performance by incorporation of reduced graphene oxide. Chem. Eng. J. 2023, 475: 145794.

[216] Shintake J, Sonar H, Piskarev E, Paik J, Floreano D, Soft pneumatic gelatin actuator for edible robotics, 2017 IEEE/RSJ International Conference on Intelligent Robots and Systems (IROS), IEEE, 2017, pp. 6221-6226.

[217] He Q, Huang Y, Wang S. Hofmeister effect-assisted one step fabrication of ductile and strong gelatin hydrogels. Adv. Funct. Mater. 2018, 28: 1705069.

[218] Zhao X, Lang Q, Yildirimer L, Lin Z Y, Cui W, Annabi N, Ng K W, Dokmeci M R, Ghaemmaghami A M, Khademhosseini A. Photocrosslinkable gelatin hydrogel for epidermal tissue engineering. Adv. Healthcare Mater. 2016, 5: 108-118.

[219] Xu C, Guan S, Dong X, Qi M. Super strong gelatin/cellulose nanofiber hybrid hydrogels without covalent cross-linking for strain sensor and supercapacitor. Composites, Part A. 2023, 164: 107287.

[220] Li Z, Wang B, Lu J, Xue Y, Wang J, Jia B, Han G, Zhao Y, Qureshi M A K, Yu L. Highly Stretchable, Self-Healable, and Conductive Gelatin Methacryloyl Hydrogel for Long-Lasting Wearable Tactile Sensors. Adv. Sci. 2025, e02678.

[221] Jin T, Sun Z, Li L, Zhang Q, Zhu M, Zhang Z, Yuan G, Chen T, Tian Y, Hou X.

Triboelectric nanogenerator sensors for soft robotics aiming at digital twin applications. Nat. Commun. 2020, 11: 5381.

[222] Lu Y, Tian H, Cheng J, Zhu F, Liu B, Wei S, Ji L, Wang Z L. Decoding lip language using triboelectric sensors with deep learning. Nat. Commun. 2022, 13: 1401.

[223] Yu S, Piao X, Park N. Machine learning identifies scale-free properties in disordered materials. Nat. Commun. 2020, 11: 4842.